Final Technical Report

Project Title: Perovskite/Perovskite Tandem Photoelectrodes for Low-Cost Unassisted Photoelectrochemical Water Splitting

Project Period of Performance: October 1st, 2019 – March 31st, 2024

Date of Report: 8/15/2024

Recipient: University of Toledo

Principal Investigator: Yanfa Yan, 419-530-3918, yanfa.yan@utoledo.edu

Teaming Members:
Zhaoning Song, University of Toledo
Kai Zhu and Joe Berry, HydroGEN Consortium NREL node
Todd Deutsch and James Young, HydroGEN Consortium NREL node
Jon Lee and Tadashi Ogitsu, HydroGEN Consortium LLNL node

DOE Managers: James Vickers, 202-287-6446, james.vickers@ee.doe.gov

Acknowledgement:

This material is based upon work supported by the U.S. Department of Energy's Office of Energy Efficiency and Renewable Energy (EERE) under the Hydrogen Fuel Technology Office DE-FOA-0002022 Award Number DE-EE0008837.

Executive Summary: In this project, we aim to address the challenges of achieving efficient and cost-effective unassisted photoelectrochemical water splitting using perovskite/perovskite tandem photoelectrodes. We utilized the following unique approaches to advance our innovation. (1) We developed stable and efficient low-E_g (1.2 – 1.4 eV) perovskites as the bottom electrodes. We demonstrated approaches to improve the photovoltaic performance and photothermal stability of low-E_g Sn-Pb iodide perovskite solar cells. (2) We developed a low-

temperature synthesis route to fabricate wide-E_g (>1.8 eV) perovskite top electrodes. By combining theoretical and experimental investigation, we found methods to reduce the formation of defects and dislocations in the wide-E_g mixed halide perovskites and suppress halide segregation. (3) We developed a robust metal oxide-based interconnecting layer to integrate two perovskite layers into tandem photoelectrodes. Our monolithically integrated tandem devices feature a high V_{OC} of more than 2 V and a high J_{SC} of more than 15 mA/cm^2. We showed the new design of the tandem photoelectrodes that is critical to the stable operation of tandem photoelectrodes for unassisted PV/PEC water splitting. (4) We demonstrated a water-impermeable barrier of carbon paste/epoxy/metal foil composite, which can prevent photocorrosion and water ingress of perovskite active layers. This surface protection enabled the operation of perovskite photoelectrodes in water and significantly enhanced the long-term stability of our tandem devices. (5) We conducted standardized PEC characterization in collaboration with NREL and reported accurate determination of solar-to-hydrogen conversion efficiencies of perovskite/perovskite tandem photoelectrodes. At the end of the project, we demonstrated perovskite/perovskite tandem photoelectrodes with STH efficiencies of up to 18% and less than 20% efficiency loss after continuous operation for more than 500 hours in water. Our results demonstrate the potential to develop a low-cost, durable, and efficient water-splitting system that meets the DOE 2026 and 2031 cost targets for hydrogen production.

Project Objectives:

In this project, we propose to develop monolithically integrated perovskite/perovskite tandem photoelectrodes to achieve low-cost, high efficiency (solar-to-H_2 efficiency (STH) up to 20%), and long-term stability (>1,000 hours) spontaneous water splitting systems. According to recent theoretical modeling, a tandem device consisting of a 1.80 eV wide bandgap (E_g) perovskite top photoelectrode and a 1.25 eV low-E_g mixed Pb-Sn perovskite bottom photoelectrode can yield an STH efficiency of >20%. The perovskite/perovskite tandem photoelectrodes can be fabricated by low-cost low-temperature solution processes on conductive flexible inexpensive stainless steel (SS) substrates, presenting a significant technoeconomic advantage over the state-of-the-art spontaneous water splitting devices such as InGaP/GaAs and InGaP/InGaAs tandem photoelectrodes. This project will also leverage the extensive materials characterization and device measurement expertise at NREL (node of the HydoGEN EMN consortium).

Project Accomplishments:

In Budget Period 1 (BP1), we developed technical approaches to accomplishing the milestones and learned lessons about some too-aggressive goals set in the initial proposal. We reevaluated and revised some milestones based on the early investigation results. Mainly, the low-E_g mixed tin-lead perovskite solar cells are too difficult to achieve in the n-i-p device configuration and are too vulnerable to air or water-induced degradation. Therefore, we made a pivotal change from the artificial leaf type of wireless photoelectrodes (which require the n-i-p type solar cell configuration) to wired tandem photoelectrode (can work for both n-i-p and p-i-n device configurations) to overcome the current limitations of the proposed materials and device structures. We also investigated some later tasks due to the change of work plan and achieved some promising results relevant to the project's success. At the end of BP1, we demonstrated double-junction tandem solar cells (p-i-n configuration) with a power conversion efficiency of > 22% and stable operation in the air for more than 300 hours, which meet the criterion of the

GNG decision point, despite a revised device configuration. We also demonstrated more than 100 hours of photoelectrode operation in an aqueous electrolyte.

In Budget Period 2 (BP2). We continued to work on perovskite/perovskite tandem photoelectrodes in the p-i-n configuration. We reevaluated and revised some milestones based on the investigations. Mainly, fabricating efficient tandem perovskite photoelectrodes on metal foils or metal-coated glass substrates has proven to be very difficult. The soft nature of metal halide perovskites enables the direct integration of perovskite thin film stacks to a piece of metal foil using conductive adhesives. Therefore, we made a pivotal change from the artificial leaf type of wireless to wired tandem photoelectrode (which can work for both n-i-p and p-i-n device configurations) to overcome the current limitations of the proposed materials and device structures. At the end of BP2, we demonstrated Pb/(Pb,Sn) perovskite double-junction tandem solar cells (p-i-n configuration) with a power conversion efficiency (PCE) of > 26% and stable operation in the air for more than 300 hours. We also demonstrated Pb/Pb double-junction tandem solar cells (p-i-n configuration) with a PCE of > 21% and stable operation in the air for more than 500 hours. Utilizing the device structure of these perovskite tandem cells, we fabricated perovskite/perovskite tandem photoelectrodes by applying metal integration and epoxy edge sealing. We demonstrated perovskite/perovskite tandem photoelectrodes with STH efficiencies up to 15% in a wired two-electrode system and a T_{80} lifetime (retaining 80% of initial efficiency) of more than 100 hours in an aqueous electrolyte, which meet the criterion of the GNG decision point for BP2.

In Budget Period 3 (BP3), we focused on the improvement of wired perovskite/perovskite tandem photoelectrodes. We demonstrated double-junction perovskite/perovskite tandem solar cells with a PCE of 28% and stable operation in the air for more than 1,000 hours. We demonstrated perovskite/perovskite tandem photoelectrodes with STH efficiencies of up to 18% in a wired two-electrode system. We also demonstrated more than 500 hours of continuous operation for a perovskite/perovskite tandem photoelectrode in a two-electrode configuration in a 0.5 M H2SO4 electrolyte, retaining more than 80% of its initial STH efficiency. We did not achieve the proposed project goal of 20% STH efficiency and more than 1,000 hours of long-term stability, but our results still demonstrated the great potential of using perovskite/perovskite tandem photoelectrodes for a spontaneous water-splitting hydrogen production system.

Project Activities:

1. Fabricating wide-E_g $CsPbBr_3$-based perovskite solar cells with a bandgap of > 2.0 eV

This project started with developing efficient all-perovskite tandem solar cells in the n-i-p configuration. We first worked on the synthesis of high-quality wide-E_g (> 2.0 eV) $CsPbBr_3$ perovskite photoelectrode for photoelectrochemical (PEC) water splitting. To achieve more stable and high-efficiency n-i-p perovskite tandem photoelectrodes, we investigated the target bandgap combination for the top/bottom electrodes from 1.75/1.25 to 2.3/1.6 eV. $CsPbBr_3$ (E_g = 2.3 eV) has demonstrated a high V_{OC} of ~1.6 V in a perovskite solar cell (*Adv. Energy Mater.* 8, 1802346, 2018). More importantly, $CsPbBr_3$ has shown much better stability against water than the widely used organic-inorganic halide perovskites, which makes $CsPbBr_3$ a very promising candidate for practical photoelectrochemical water-splitting applications.

However, due to the low solubility of CsBr in most organic solvents, a multi-step method is typically used to fabricate $CsPbBr_3$ thin films. In this process, we first deposited a $PbBr_2$ layer by spin-coating a 1 *M* $PbBr_2$/DMF precursor solution and annealed at 100 °C for 5 min. After that, we spin-coated a 0.07 *M* saturated CsBr/methanol solution on $PbBr_2$ and annealed at 250 °C for 5 min. The CsBr/methanol coating/annealing process was repeated for ~7 times for a complete perovskite phase conversion. Each of the CsBr coating and annealing cycles needs to be taken care of carefully to prompt a strong CsBr/$PbBr_2$ reaction, which is critical for the quality control of the final film phase purity and morphology.

It is noted that after the first 2 to 3 CsBr cycles, the film turns light yellow after spin-coating a CsBr/methanol solution on a $PbBr_2$ layer, indicating the formation of the $CsPbBr_3$ phase. Upon the 250 °C annealing, the film turns white immediately, which indicates the transformation to the $CsPb_2Br_5$ phase due to CsBr deficiency caused by the low CsBr/methanol precursor concentration. After 6 to 7 cycles, the film can be stabilized to the $CsPbBr_3$ phase, showing a yellowish color after annealing. However, the film may become white again at the 7th cycle (or more cycles) when introducing excess CsBr, because of the phase transformation to the Cs_4PbBr_6 with insufficient $PbBr_2$. Therefore, the precise control of the reaction between $PbBr_2$ and CsBr is critical to obtain the pure $CsPbBr_3$ stoichiometry.

We employed the multi-step method to fabricate 15 $CsPbBr_3$ cells with an n-i-p type device configuration of FTO/SnO_2/$CsPbBr_3$/Spiro-OMeTAD/Au. The statistical device performance is shown in Figure 1. All the parameters show a wide range of distribution with V_{OC} varying from 1.33 to 1.41 V, J_{SC} varying from 5.4 to 6.2 mA/cm^2, FF varying from 60 to 73%, and PCE varying from 4.6 to 6.1%. The inferior device performance and undesirable reproducibility indicate the challenge of synthesizing high-quality and pure-phase $CsPbBr_3$ perovskites by the multi-step process.

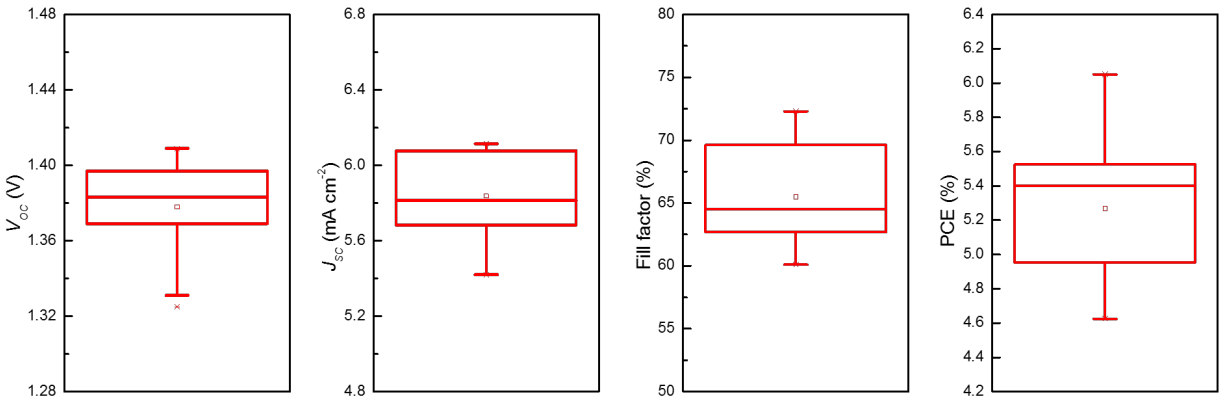

Figure 1. Statistical distribution of $CsPbBr_3$ device performance made by the multi-step method.

We then introduced a low-temperature reaction process after the spin-coating of CsBr to retard the fast reaction and diffusion of CsBr. After the first cycle of CsBr spin-coating, we first anneal the film at 100 °C for 5 min. During this annealing stage, methanol evaporates slowly, and CsBr spreads uniformly on the $PbBr_2$ layer, which enables a more even reaction between CsBr and

$PbBr_2$. Then, a high temperature (220 °C) annealing is performed to fully convert the film to the $CsPbBr_3$ perovskite. Benefiting from the uniform phase transformation, the film made by this method only needs one cycle of CsBr deposition. Figure 2 compares the SEM morphology images of $CsPbBr_3$ film prepared by using the conventional approach and this method. The grain size distribution of the film (Figure 2b) becomes much more uniform than the multi-step prepared film (Figure 2a). The grains show an average grain size of about 600 nm with reduced grain boundaries, which is beneficial for reducing non-radiative recombination.

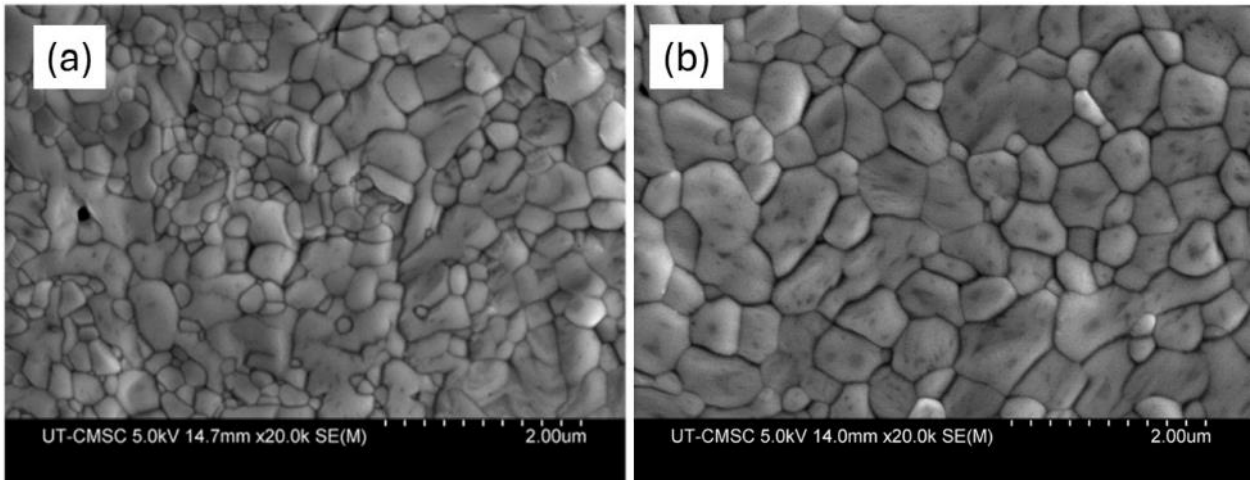

Figure 2. SEM images of $CsPbBr_3$ perovskite films made by (a) the conventional approach and (b) a novel approach using a low temperature of 100 °C annealing and then 220 °C annealing.

We then fabricated 15 $CsPbBr_3$ PSCs using this method. Figure 3 displays their statistical histogram and the J-V curve of a typical device. Due to the complete phase transformation and improved film quality, the devices show a narrow distribution of PCE from 6.5 to 7.2%. A typical device shows a V_{OC} of 1.447 V, a J_{SC} of 6.41 mA/cm^2, a FF of 74.4%, and a PCE of 6.9%. The improved device performance, especially the high V_{OC} is very desirable for the unassisted water splitting. Also, improved film quality and reduced grain boundaries can help improve device stability, which is quite essential when considering realistic PEC applications in water.

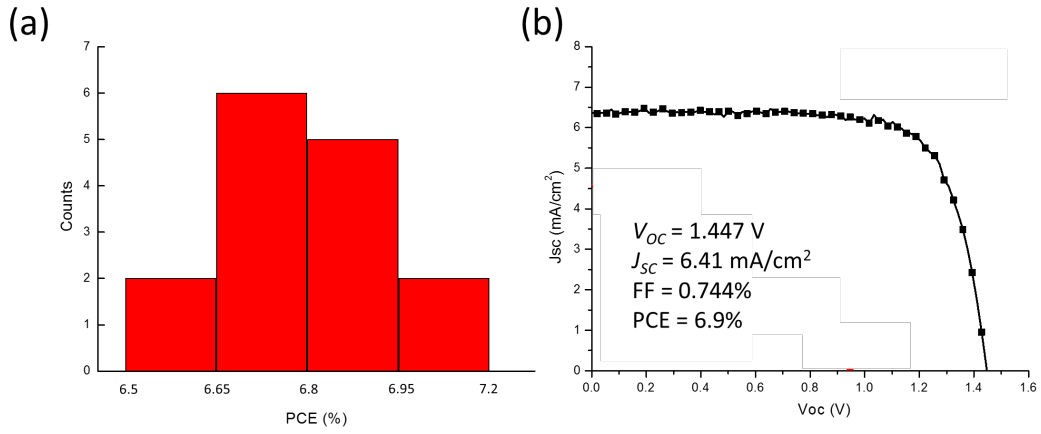

Figure 3. (a) Statistical histogram of 15 cells and (b) a typical J-V curve of a $CsPbBr_3$ PSC.

To prepare for the preliminary tests of using CsPbBr3 PSCs for wired, three-electrode, unassisted water splitting, we tracked the efficiency evolution of a $CsPbBr_3$ PSC in water to test its durability when working as a photoelectrode in aqueous electrolyte. As shown in Figure 4a, in the first 200 seconds of tracking in ambient air, the device shows almost no degradation. We then soak the device entirely in the water at the 300 s, and a shape drop appears, likely due to the optical loss of water reflection and refraction. From 300 to 1,000 s, the device shows a slight decrease in PCE, which is likely caused by the degradation of the charge transport layer (Li-doped Spiro-OMeTAD) and $CsPbBr_3$ light absorber layer. As can be seen in Figure 4b, $CsPbBr_3$ shows excellent stability against water. The perovskite layer underneath the Au electrode still shows a yellowish color after almost 1,000 seconds in water, which reveals the potential of $CsPbBr_3$ for water-splitting application. It is worth noting that we are working on developing a water-resistive coating for perovskite photoelectrode. If successful, the applications of $CsPbBr_3$ perovskite photoelectrode will become very promising.

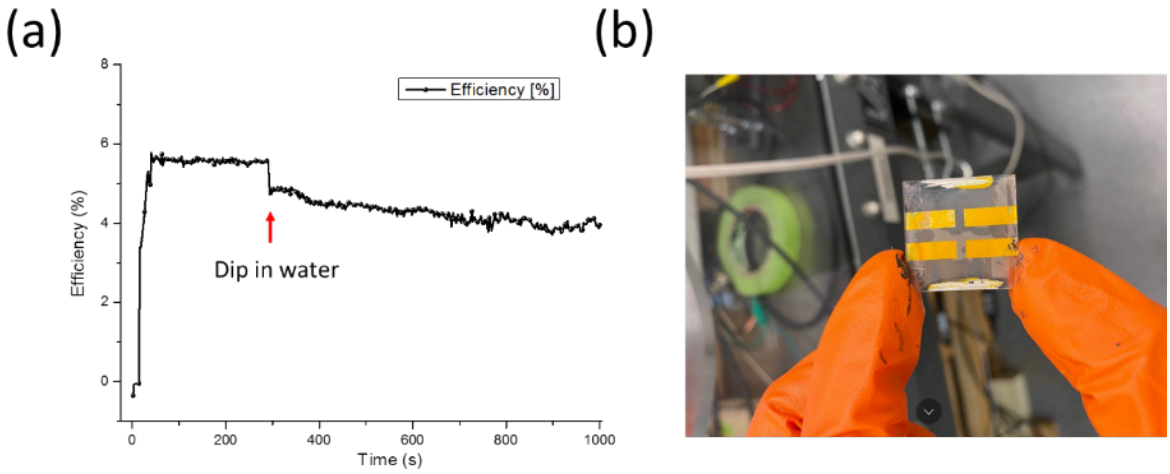

Figure 4. (a) PCE tracking of a $CsPbBr_3$ device. The red arrow indicates the time of soaking the device in water. (b) a photo taken from the glass side of a $CsPbBr_3$ device after 1,000 s soaking in water.

2. Modified hole transport layer for *n-i-p* structured tandem photoelectrodes

The use of a dopant-free hole-transport layer (HTL) as an interconnection layer in the *n-i-p* structured tandem photoelectrodes is critical for the development of n-i-p type perovskite/perovskite tandem photoelectrodes. Conventionally used HTLs, such as Spiro-OMeTAD and PTAA, usually require dopants such as Li-TFSI and TBP to improve their conductivity. However, these dopants are harmful to tandem device performance and stability. Li-TFSI is hydrophilic and may absorb moisture, while TBP is easy to escape at the typical temperature of perovskite and SnO_2 annealing, which leads to the aggregation of Li-TFSI. The migration of Li^+ ions from Spiro-OMeTAD into perovskites is also detrimental, which increases

hysteresis and reduces device performance. Therefore, PEDOT:PSS is more suitable for tandem photoelectrodes when considering stability due to the absence of ionic dopants. Moreover, applying a thin layer of PEDOT:PSS can effectively prevent the penetration of perovskite precursor solutions to other layers underneath, which is quite important when fabricating tandem photoelectrodes.

To simultaneously fulfill high device performance and avoid precursor solution penetration, one possible way is to mix Spiro-OMeTAD with PEDOT:PSS to prepare a new HTL that can combine both of their features. The mixed PEDOT:PSS and Spiro-OMeTAD will be denoted as PPSO afterward in this report. We then fabricated single-junction $MAPbI_3$ photoelectrodes with the device configuration of Glass/ITO/SnO_2/$MAPbI_3$/PEDOT:PSS or PPSO/sputtering ITO. For PPSO devices, we varied the volume concentration of Spiro-OMeTAD from 0% to 50% (i.e., PEDOT:PSS from 100% to 50%). As can be seen in Figure 5, $MAPbI_3$ photoelectrodes made by using PEDOT:PSS (0%) as HTL shows the lowest device performance with an average V_{OC} of ~0.95 V, a J_{SC} of ~17 mA/cm^2, and a FF of ~ 0.6. For the PPSO-based devices with 25% Spiro-OMeTAD, the device parameters show an overall improvement, with an average V_{OC} of ~0.98 V, a J_{SC} of ~19 mA/cm^2, and a FF of ~ 0.7. After mixing 50% Spiro-OMeTAD in PPSO, device parameters, especially V_{OC}s and J_{SC}s were further improved, showing an average V_{OC} as high as ~1.1 V and a J_{SC} of up to 20.3 mA/cm^2. These significant improvements indicate that by simply mixing PEDOT:PSS with Spiro-OMeTAD, the conductivity of Spiro-OMeTAD can also be sufficiently improved in the absence of dopants.

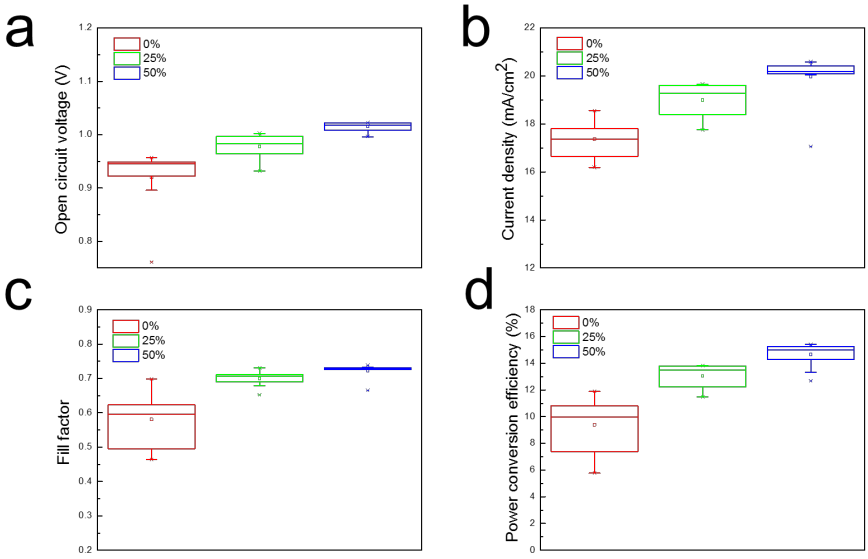

Figure 5. Device parameters of $MAPbI_3$ cells by using PEDOT:PSS and PPSO as the HTLs, including (a) open circuit voltage, (b) short circuit current density, (c) fill factor, and (d) power conversion efficiency

Yet, it still remains questionable whether PPSO can prevent the precursor penetration during the fabrication of the second perovskite cell in a tandem configuration. Hence, we fabricated *n-i-p* structured tandem photoelectrodes with the device configuration of Glass/ITO/SnO_2/thin $MAPbI_3$/HTLs/sputtering ITO/ALD SnO_2/thick $MAPbI_3$/Spiro-OMeTAD/Au, where HTLs are doped Spiro-OMeTAD, dopant-free PEDOT:PSS, and PPSO respectively. Figure 6a is the

cross-sectional SEM image of a tandem photoelectrode using Spiro-OMeTAD as an interconnection layer. From the image, we observe an anomalous single-layer structure with no distinct borders between layers, which is likely due to the re-dissolution of the as-formed top perovskite layer after spin-coating of the second perovskite precursor solution. In distinct contrast to the Spiro-OMeTAD-based device, PEDOT:PSS and PPSO both effectively preserved the device configuration and enabled tandem photoelectrodes with well-bordered layers (Figure 6b and 6c).

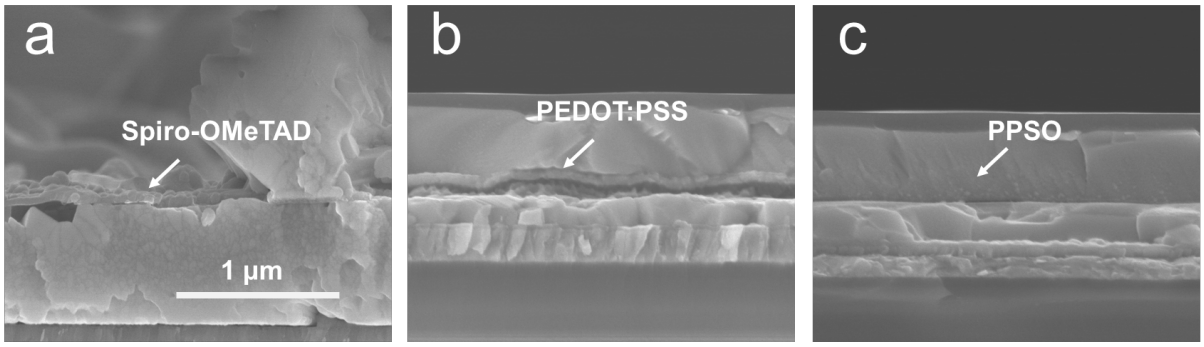

Figure 6. Cross-sectional SEM images of tandem photoelectrodes using (a) Spiro-OMeTAD, (b) PEDOT:PSS, and (c) PPSO as HTLs at interconnection.

We have proposed *n-i-p* structure tandem photoelectrodes with a V_{OC} of over 2 V after employing suitable wide-bandgap sub-cells. Thanks to the decent PPSO interconnection layer, we got a V_{OC} of more than 2 V for the tandem photoelectrodes by using two identical normal-bandgap $MAPbI_3$ sub-cells. As can be seen in Figure 7, the device shows a V_{OC} of 2.06 V, and a FF of 75.5%. The low J_{SC} of ~9.5 mA/cm^2 is due to the limitation of the 250 nm thick $MAPbI_3$ top sub-cell. Further improvement of J_{SC} can be achieved by optimizing the bandgap match of the two sub-cells to widen solar spectrum absorption. Note that *n-i-p* structured tandem devices with such high V_{OC} were rarely reported before. Such high V_{OC}s are quite desirable for the unassisted water-splitting application.

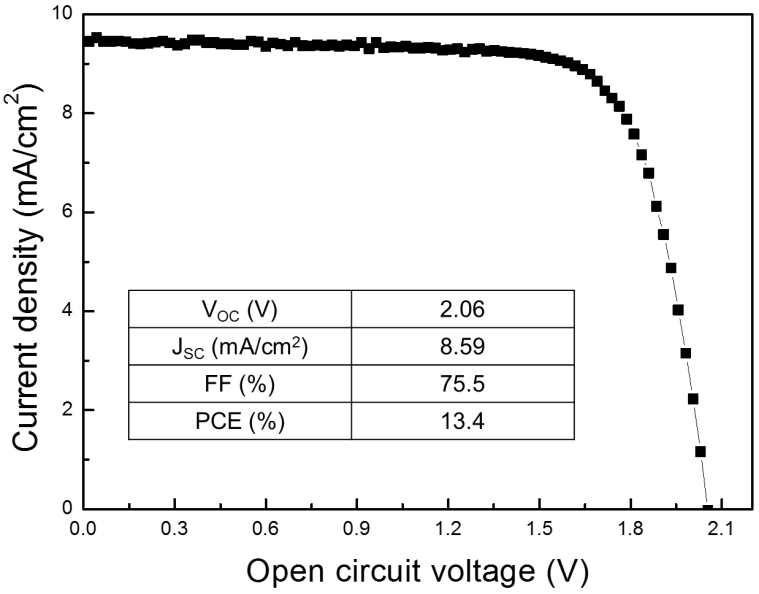

Figure 7. Device performance of the tandem photoelectrode under the configuration of Glass/ITO/SnO_2/thin $MAPbI_3$/HTLs/sputtering ITO/ALDE SnO_2/thick $MAPbI_3$/Spiro-OMeTAD/Au.

The tandem photoelectrodes were sent to NREL EMN nodes to measure the PV-EC characteristics. The high photovoltage (Voc) was confirmed, but the tandem photoelectrodes show significant hysteresis, some instability, and large series resistance. The photovoltage is sufficient to drive water splitting unassisted using Pt and IrO_x in 0.5 sulfuric acid, but only at low current densities ~1 mA/cm^2 due to a relatively low fill factor.

3. High-quality inorganic $CsPbI_2Br$ top photoelectrodes with low V_{OC} deficits

We have previously fabricated high-efficiency $(FAPbI_3)_{0.95}(MAPbBr_3)_{0.05}$ bottom photoelectrodes with a bandgap of ~1.5 eV. Combined with our progress of fabricating *n-i-p* structured tandem photoelectrodes, it is reasonable to move forward to the exploration of wide bandgap top sub-cells that match with the ~1.5 eV bottom sub-cells. According to the Shockley-Queisser detailed balance, when coupling with a ~1.5 eV bottom sub-cell, the bandgap of the top sub-cell should be close to 1.95 eV to maximize the overall performance of the tandem photoelectrode. However, for conventional organic-inorganic mixed perovskites, e.g., $MAPbI_xBr_{3-x}$, the concentration of Br will need to be more than 50% to reach a bandgap of ~1.95 eV. When containing such a high concentration of Br, perovskite films inevitably exhibit severe phase segregation issues, which both sacrifice device efficiency and stability. Compared with the organic-inorganic ones, Cs-based inorganic perovskites contain a lower Br concentration when having the same bandgap due to their smaller Cs atomic size, which delivers reduced phase segregation. Besides, Cs-based inorganic perovskites were reported to have better phase stability under illumination due to stronger interactions between Cs atoms and PbI_6 frameworks. For this research activity, we have investigated inorganic $CsPbI_2Br$ perovskites with a bandgap

of ~1.91 eV. The phase segregation is compared between organic-inorganic perovskites and Cs-based inorganic ones. Further, we have made a preliminary exploration of using formamidine acetate salt (FAOAc) additive to regulate the crystallization process of $CsPbI_2Br$ perovskite films, which significantly improved device performance.

We first compared the photostability and phase segregation characteristics of two different categories of wide-bandgap perovskites with a similar Br concentration, i.e., the organic-inorganic mixed $FA_{0.8}Cs_{0.2}Pb(I_{0.7}Br_{0.3})_3$ (control) and Cs-based inorganic $CsPbI_2Br$, by using in-situ PL measurement with an excitation wavelength of 532 nm and a power density of 1.56 w/cm^2 for 30 minutes. As shown in Figure 8a, the control film shows a significant peak shift towards a longer wavelength range under continuous laser beam exposure, indicating strong phase segregation of the homogenous perovskite composition to I-based and Br-based ones. In contrast, Cs-based inorganic $CsPbI_2Br$ shows a much smaller peak shift after 30 minutes (Figure 8b), indicating its suppressed phase segregation feature.

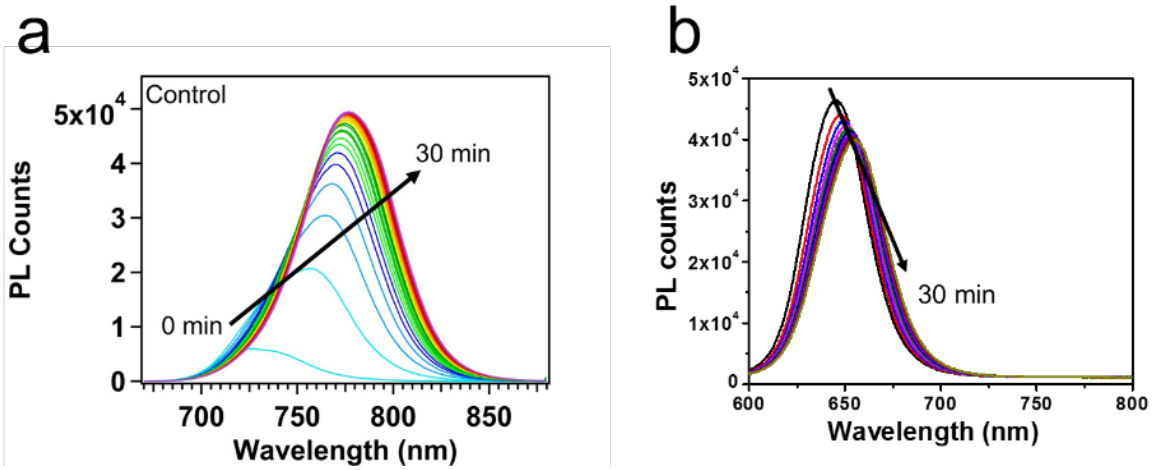

Figure 8. In-situ PL spectra of (a) $FA_{0.8}Cs_{0.2}Pb(I_{0.7}Br_{0.3})_3$ and (b) $CsPbI_2Br$ under continuous laser exposure.

However, the high V_{OC} deficits of inorganic perovskite cells compared with the organic-inorganic ones still limit their further application. Due to the rapid crystallization nature, Cs-based inorganic perovskite films usually comprise small-sized grains with excess grain boundaries. The excess grain boundaries are defective and are usually where non-radiative recombination happens. Typically, perovskite films with high-quality grains and reduced grain boundaries show suppressed dark saturation current and a high V_{OC}. Additive engineering is a widely adopted way to improve perovskite film quality. Here, we introduced formamidine acetate salt (FAOAc) as an additive to regulate the perovskite film crystallization process, which led to enlarged gran sizes and improved film quality. As a result, a high V_{OC} of 1.365 eV with a PCE of ~15% was achieved for the additive-assisted $CsPbI_2Br$ photoelectrodes.

We first measured the top-view SEM images of $CsPbI_2Br$ perovskite films with and without FAOAc additive. As can be seen in Figure 9a, the film without FAOAc shows an amorphous morphology with small grain sizes and blurry grain boundaries. This is likely due to the fast

crystallization process caused by the rapid evaporation of solvents at a typical annealing temperature of 300 ˚C. In contrast, after adding 50 mol% FAOAc in the stoichiometric $CsPbI_2Br$ precursor solution, the grain size after annealing is much enlarged to more than 1 μm (Figure 9b). The FAOAc is expected to form an intermediate phase at an early stage of the film crystallization process, which induces a large grain feature. Later, the organic molecules (FA) will be exchanged and replaced by Cs at a higher temperature and after a longer annealing time without changing the large grain morphology. The exchange process will also prolong the grain coarsening, which is also beneficial for grain growth.

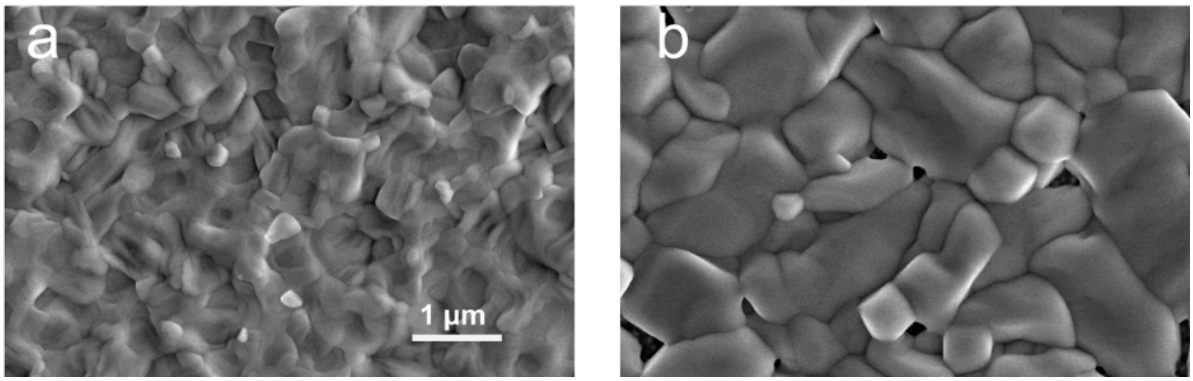

Figure 9. SEM images of $CsPbI_2Br$ films (a) without and (b) with FAOAc additive.

We then gave a preliminary exploration of the fabrication of n-i-p structured photoelectrodes based on the high-quality FAOAc-assisted $CsPbI_2Br$ perovskite films. As can be seen in Figure 10, the photoelectrode device without additive shows a V_{OC} of 1.085 V with a large V_{OC} deficit of 0.825 V, which is quite undesirable. After applying 50 mol% FAOAc as an additive, the V_{OC} was distinctly improved to 1.363 V, showing a V_{OC} deficit as low as 0.453 V. The high-efficiency $CsPbI_2Br$ perovskite cells can be used to fabricate tandem devices.

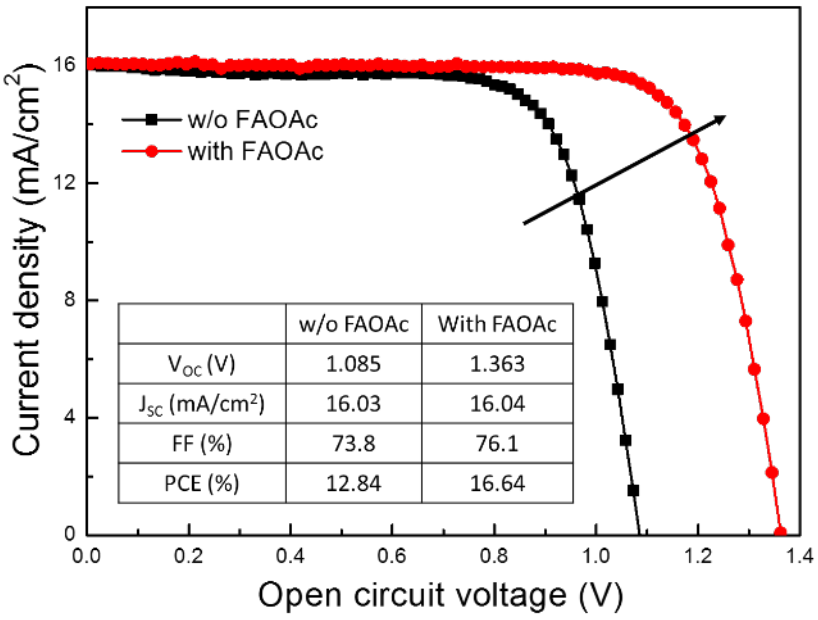

	w/o FAOAc	With FAOAc
V_{OC} (V)	1.085	1.363
J_{SC} (mA/cm^2)	16.03	16.04
FF (%)	73.8	76.1
PCE (%)	12.84	16.64

Figure 10. J-V curves of CsPbI2Br solar cells (a) without and (b) with FAOAc additive.

4. Preliminary water splitting tests using perovskite-perovskite tandem photoelectrodes

In this activity, we fabricated p-i-n type perovskite-perovskite tandem photoelectrodes to perform the preliminary water-splitting tests in a wired three-electrode system (Figure 11). The perovskite/perovskite tandem photoelectrode has a device structure of Glass/ITO/PTAA/wide-E_g perovskite/C_{60}/SnO_2/ITO/PEDOT: PSS/low-E_g perovskite/C_{60}/BCP/Ag. To ensure the operation of the photoelectrodes in aqueous solution, we applied a silver epoxy paste on the back contact of perovskite/perovskite photoelectrodes and connected a Cu wire to the ITO contact of the photoelectrode. Non-conductive epoxy adhesive was used to wrap up the non-active area of the photoelectrodes, leaving an illumination window of an area of 0.25 cm^2, as shown in Figure 12.

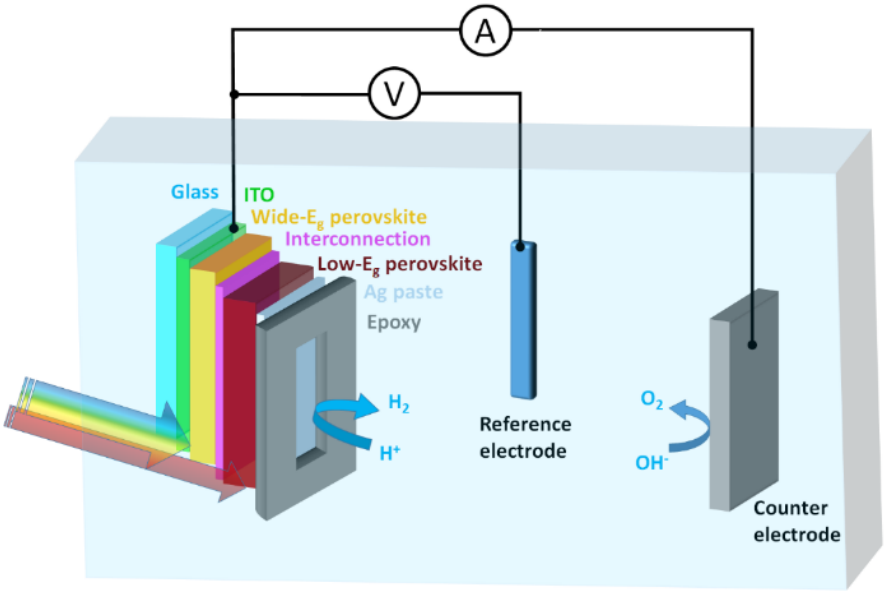

Figure 11. Schematic of a three-electrode water splitting system consisting of a p-i-n tandem photoelectrode.

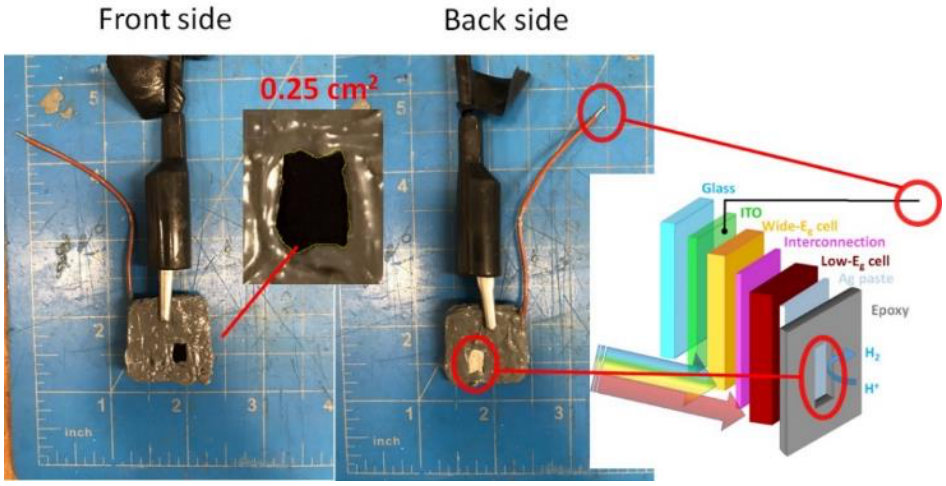

Figure 12. Photos and schematic of a p-i-n type perovskite/perovskite tandem photoelectrode.

The photoelectrochemical characterization was carried out using a Voltalab potentiostat in a three-electrode configuration with an Ag/AgCl reference electrode and a Pt counter electrode in a quartz container filled with electrolyte. A mild near-neutral (0.5 M Na_2SO_4) aqueous electrolyte (pH = 6.5) was used. The recorded potential versus Ag/AgCl ($E_{Ag/AgCl}$) in this work was converted into potential against reversible hydrogen electrode (RHE) using the Nernst equation:

$$E_{RHE} = E_{Ag/AgCl} + 0.059 \times pH + 0.1976\ (V)$$

Photoelectrochemical response was recorded on both the forward and reverse bias potential scans under the illumination of a 300 W Xe lamp equipped with AM 1.5 filter to simulate a light intensity of 100 mW/cm^2.

Figure 13a shows linear scan voltammogram (LSV) scans of p-i-n type perovskite/perovskite tandem photoelectrode under AM 1.5G one sun illumination (red) and dark (blue) conditions. This device has a turn-on voltage (V_{on}) of ~2.25 V vs RHE. As shown in Figure 13b, the photocurrent density at zero bias vs reference (Ag/AgCl) is ~14.2 mA/cm^2, demonstrating the capability of unassisted water splitting using perovskite/perovskite tandem photoelectrodes. Unassisted PEC water splitting was observed by using the perovskite/perovskite tandem photoelectrode, as evidenced by the oxygen and hydrogen evolution reactions at two electrodes (Figure 14).

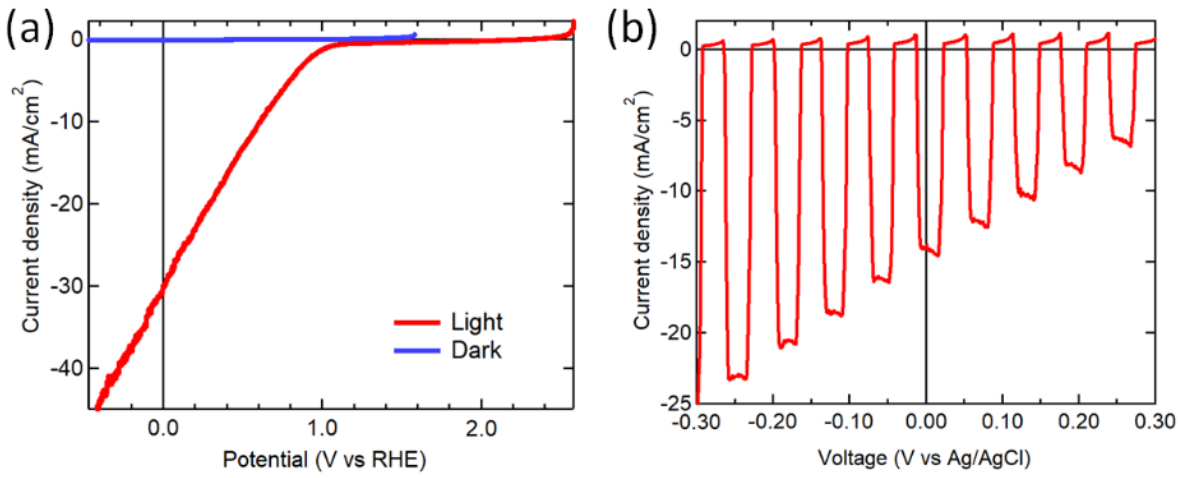

Figure 13. Photoelectrochemical characteristics of a p-i-n type perovskite/perovskite tandem photoelectrode. (a) Three-electrode linear scan voltammogram (LSV) under one sun illumination and dark conditions. (b) J−V curve of the same electrode under chopped light shows unassisted water splitting at zero bias.

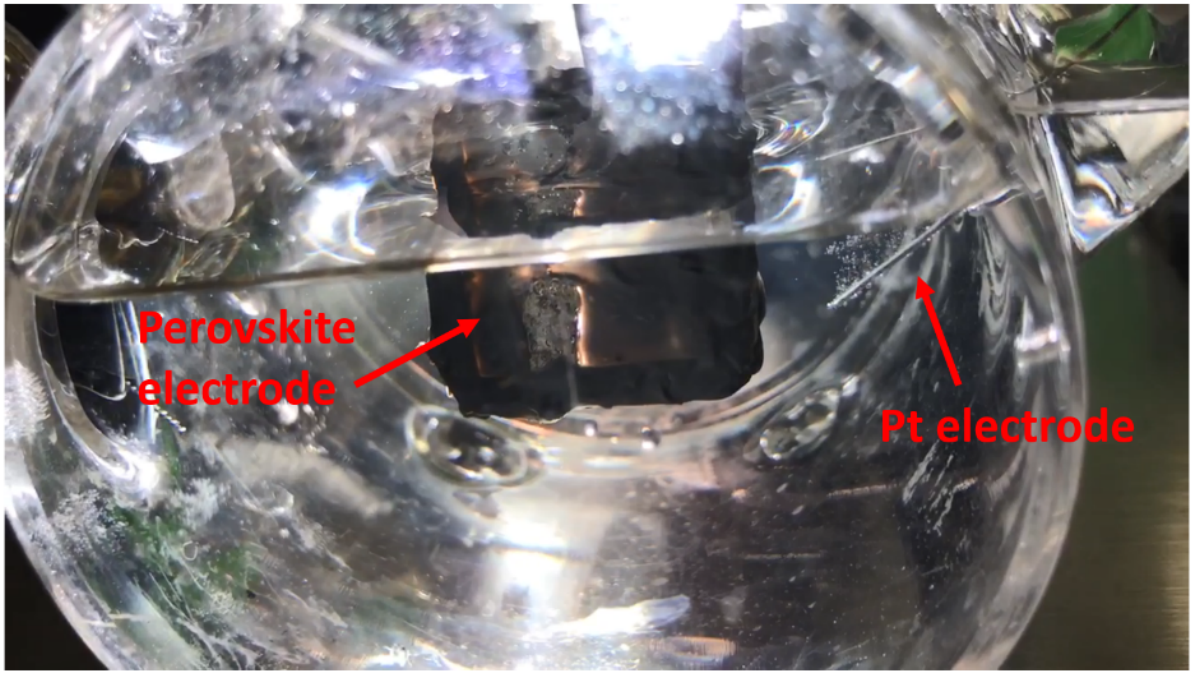

Figure 14. Photo of unassisted PEC water splitting by using a p-i-n type perovskite/perovskite tandem photoelectrode.

The open-circuit potential (OCP) measurement versus RHE under chopped light illumination was carrier out to evaluate the stability of perovskite/perovskite tandem photoelectrode (Figure 15). For a testing period of 30 min (1,800 s), the photoelectrode shows negligible degradation on the open-circuit potential. This result is encouraging for the follow-up durability tests and shows the promise for the practical applications of perovskite/perovskite tandem photoelectrodes for unassisted PEC water splitting.

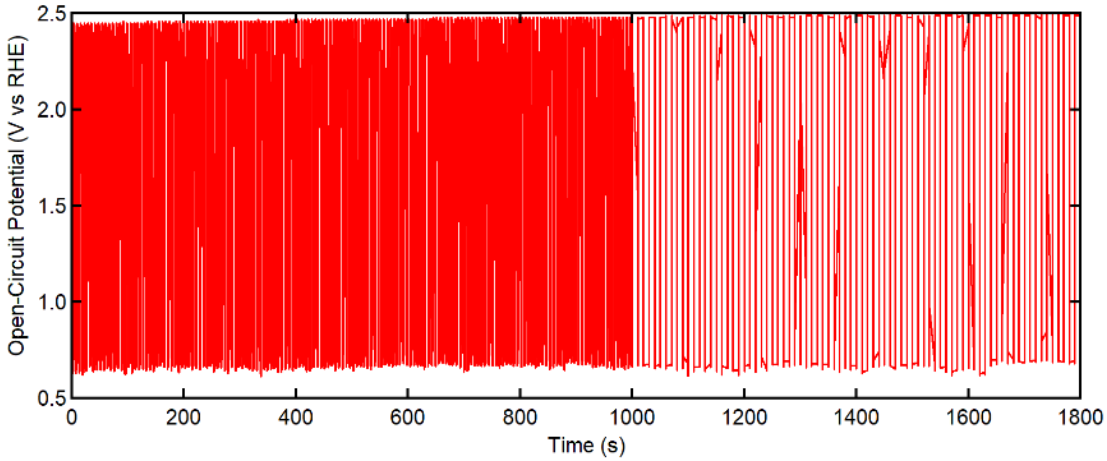

Figure 15. Open-circuit potential measurement versus RHE of a p-i-n type perovskite/perovskite tandem photoelectrode under chopped light illumination. The chopper frequency changed at 1000 s.

We also fabricated some p-i-n type perovskite-perovskite tandem photoelectrodes for preliminary water splitting tests. The tandem photoelectrode has a structure of Glass/ITO/PTAA/wide-E_g perovskite/C_{60}/SnO_2/ITO/PEDOT: PSS/low-E_g perovskite/C_{60}/BCP/Ag. The ITO contact was soldered to a Cu anode, and the Ag contact was connected to another Pt wire cathode using conductive paste (Figure 16a). We send the tandem photoelectrode to the NREL EMN node for water splitting measurements. Our collaborators at NREL performed "PV-EC" characterization, which is essentially PV-electrolysis (PV not submerged) with a Pt wire cathode and IrOx anode in 0.5 M sulfuric acid. The PV-EC measurements estimate the "best case" PEC performance that could be achieved if Pt deposition on the carbon paste gives ideal HER activity (matching that of a Pt wire). In this idealized configuration, perovskite-perovskite tandem photoelectrodes are just barely splitting water unassisted, as shown in Figure 16b. The inferior performance is likely due to the degradation of mixed Sn-Pb based perovskite and high resistance of conductive paste. We will have fresh photoelectrodes for in water test in the next quarter.

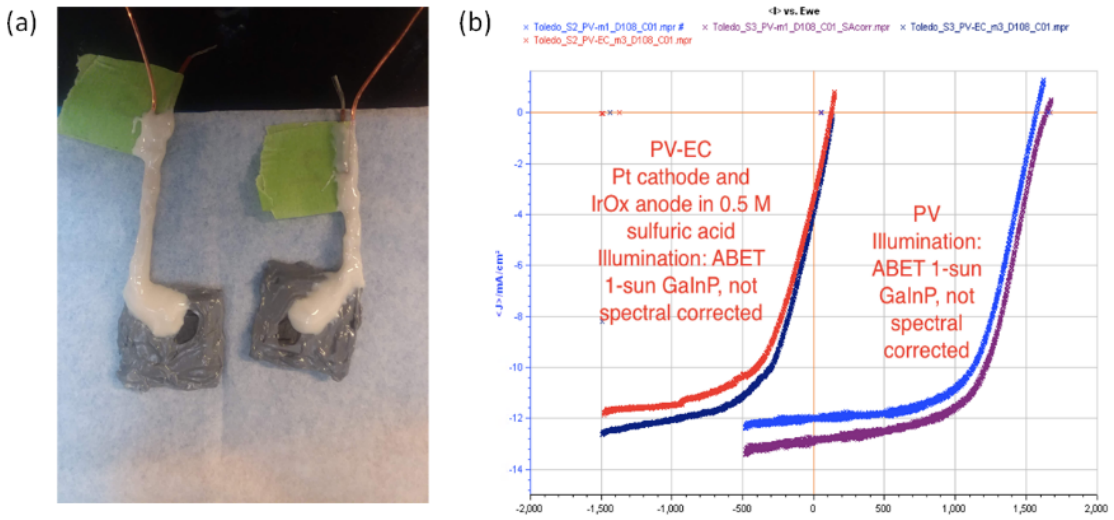

Figure 16. (a) Photo and (b) J-V curves of p-i-n tandem photoelectrodes for PV and PV-EC measurements. Unassisted water splitting has been demonstrated in the PV-EC measurement.

5. Exploring n-i-p perovskite/perovskite tandem photoelectrodes

In this activity, we mainly worked on developing an efficient interconnection layer to integrate top and bottom electrodes (both in the n-i-p device architecture) into a tandem configuration. Note that n-i-p type perovskite-perovskite tandem solar cells have rarely been reported in the literature because of the challenges for the second perovskite layer processing and device integration. To demonstrate the n-i-p tandem photoelectrodes, we used a gentle sputtered ITO/ALD SnO_2 as the interconnecting layers to integrate the two perovskite layers into the tandem photoelectrodes. Moreover, we employed conventional $MAPbI_3$ as the light absorbers

for both top and bottom photoelectrodes for the preliminary investigation of the device structure because the synthesis of high-quality wide-E_g $CsPbBr_3$ (or $FA_{0.8}Cs_{0.2}PbBr_{0.9}I_{2.1}$) and narrow-$E_g$ $FAPbI_3$ perovskite films requires critical environmental conditions that are difficult to maintain in summer.

We first tested the n-i-p tandem device comprising a configuration of Glass/ITO/SnO_2/thin $MAPbI_3$ (250 nm)/HTL/sputtering ITO/ALD SnO_2/thick $MAPbI_3$ (550 nm)/Spiro-OMeTAD/Au, as shown in Figure 17a. We investigated two widely used HTLs: PTAA and Spiro-OMeTAD, both doped with tert-butylpyridine (tBP) and lithium bis(trifluoromethylsulfonyl)-imide (Li-TFSI). The thickness of the doped PTAA and Spiro-OMeTAD are roughly 150 and 250 nm, respectively. Figure 17b and c shows the photos of the n-i-p tandem devices made by using doped Spiro-OMeTAD and PTAA as the interconnecting HTL. Both devices show a high density of pinholes in the active area of the electrodes, which indicates that the perovskite precursor solution for the second perovskite layer permeated through the interlayers and dissolved the first-deposited perovskite layer underneath. These pinholes lead to the shunting behavior of the tandem photoelectrodes.

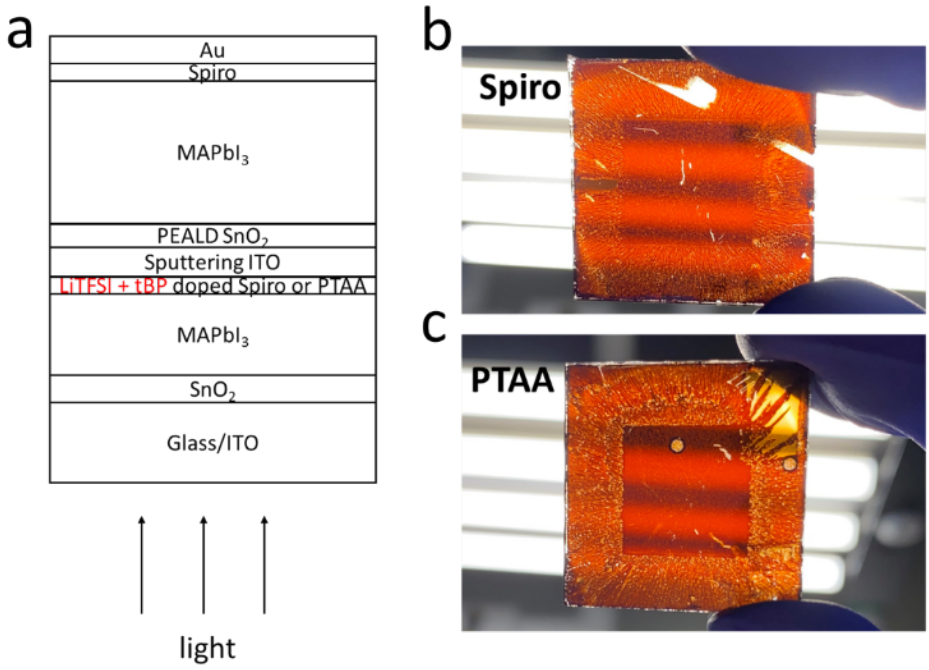

Figure 17. (a) Configuration of an n-i-p type perovskite-perovskite photoelectrode. Photos of perovskite-perovskite tandem devices using doped Spiro-OMeTAD (b) and PTAA (c) as the interconnecting HTL.

It is reported that Li-TFSI and tBP in the HTL form a tBP-Li-TFSI complex (*J. Am. Chem. Soc.*, 140, 16720, 2018). However, due to its high vapor pressure, tBP is easy to deplete from the HTL film during the sputtering process, resulting in the aggregation of Li-TFSI molecules. It is speculated that the aggregation of Li-TFSI leaves pinholes and thus collapses the interlayers, which consequentially creates tunnels for the permeation of the perovskite precursor solution.

To address the pinhole issue, we replaced the tBP-Li-TFSI complex with 2,3,5,6-Tetrafluoro-tetracyanoquinodimethane (F4-TCNQ) as dopants for Spiro-OMeTAD and PTAA. F4-TCNQ has a high melting point of 291 °C and is expected to be stable during the device fabrication. Figure 18 shows a schematic and photos of the tandem cells employing F4TCNQ doped Spiro-OMeTAD and PTAA. As seen in Figure 18b and c, the tandem photoelectrodes exhibit much fewer processing damages and pinholes. However, these tandem devices still show very low power conversion efficiencies (Figure 19). The tandem cells both show low V_{OC} values of ~1 V, indicating that the top and bottom photoelectrodes are incorrectly connected due to the failure of the interconnecting layers.

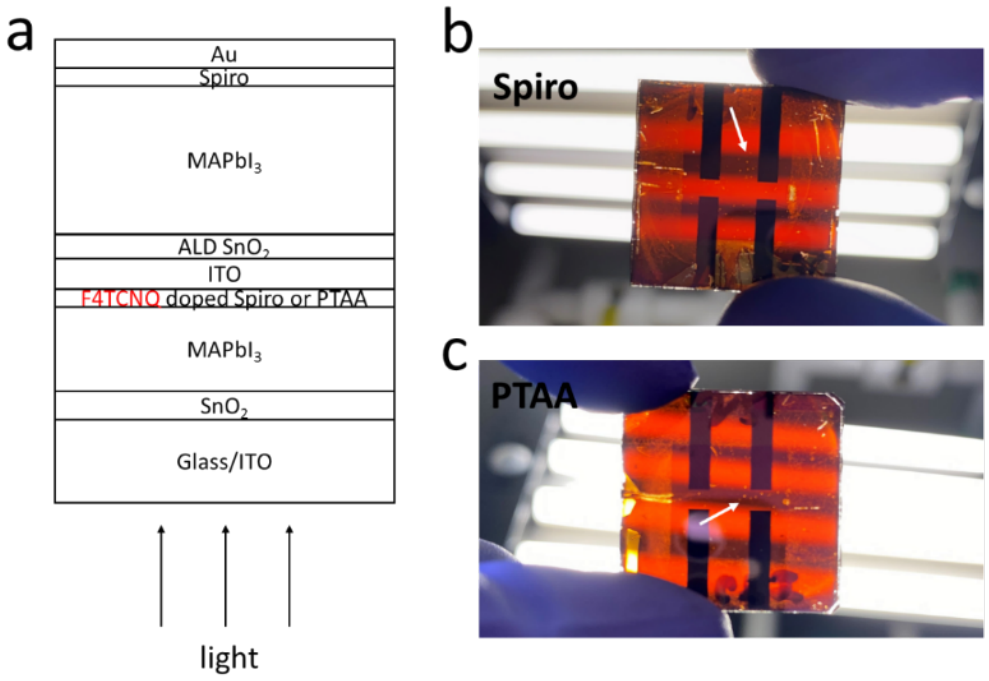

Figure 18. (a) Configuration of our n-i-p structure all perovskite tandem cell. Photos of perovskite-perovskite tandem devices made by using F4TCNQ doped (b) Spiro-OMeTAD and (c) PTAA as the interconnecting HTL.

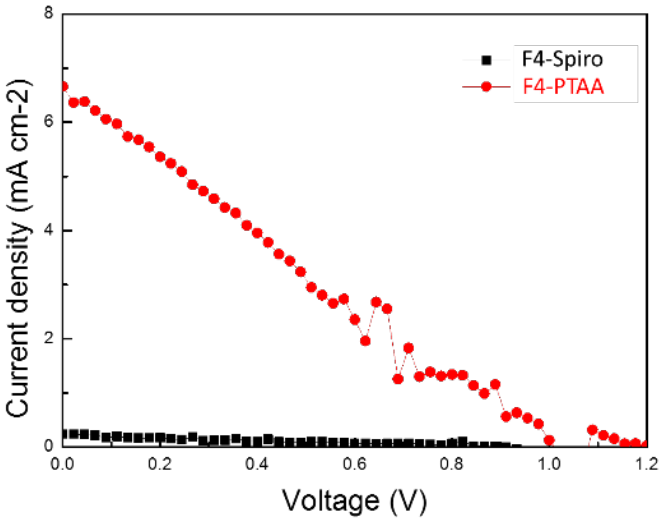

Figure 19. J-V curves of tandem devices using F4-TCNQ doped Spiro-OMeTAD (black curve and dots) and PTAA (red curve and dots) as the interconnecting HTL.

To further investigate the issues of the sputtering damages caused by the preparation of the interconnecting layers, we prepared single-junction cells with the configuration of Glass/ITO/SnO_2/$MAPbI_3$/HTL/with and without sputtering ITO/Au. Figure 20 shows the device structures and J-V curves of representative devices with different HTLs.

The PTAA-based device without a sputtering ITO layer shows a V_{OC} of 1.059 V, a J_{SC} of 21.99 mA/cm^2, a FF of 73.6%, and a PCE of 17.2%. The F4TCNQ doped Spiro-OMeTAD device shows a V_{OC} of 1.038 V, a J_{SC} of 21.84, a FF of 64.2%, and a PCE of 14.6%. However, with the insertion of sputtered ITO layers, both types of devices show no *J-V* response, which is likely due to the processing damages of sputtering ITO. One possible solution to address the sputtering damages on HTLs is the addition of a thin oxide protection layer. It has been reported that a thin layer of thermally evaporated MoO_x can protect PTAA or Spiro-OMeTAD from sputtering damage.

We also tested PEDOT: PSS in toluene (Solar 3) as the HTL layer (Figure 20c). The dense structure and mechanical robustness of PEDOT: PSS enables the ITO deposition without sacrificing device performance. Figure 20e shows the J-V curves of n-i-p perovskite solar cells without and with an ITO layer as the anode. The control device without ITO shows a V_{OC} of 0.803 V, a J_{SC} of 22.03 mA/cm^2, a FF of 68.9%, and a PCE of 12.2%, while the device with ITO shows a V_{OC} of 0.881 V, a J_{SC} of 22.6 mA/cm^2, a FF of 68.1%, and a PCE of 13.6%. Although the PCE of the device using PEDOT: PSS as the HTL is inferior to those using Spiro-OMeTAD and PTAA due to a lower work function of PEDOT: PSS, the PEDOT: PSS layer can protect the perovskite absorber layer from sputtering damages. Additionally, the performance of devices with PEDOT: PSS HTL could be potentially improved by modifying the work function of PEDOT: PSS by using proper functional groups.

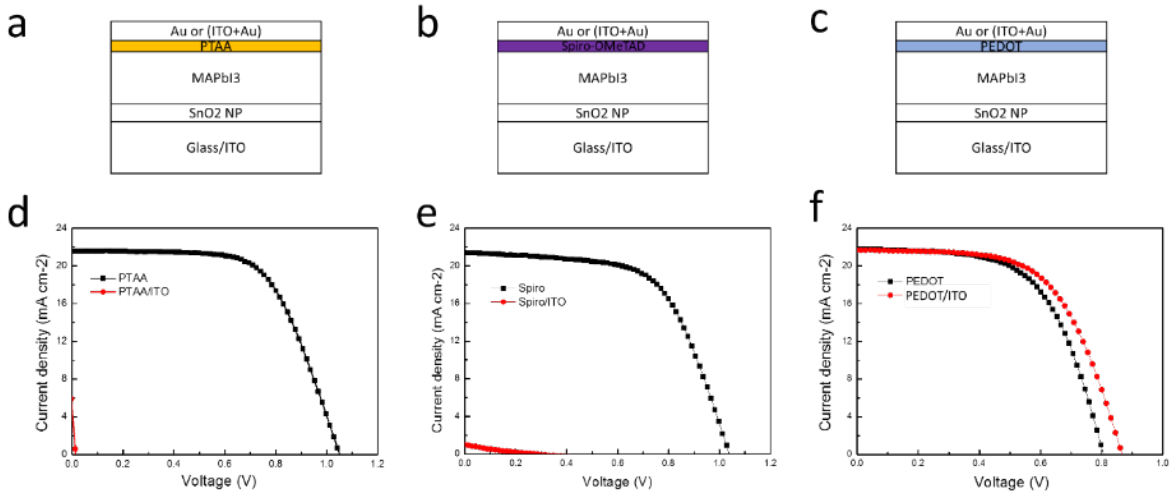

Figure 20. Device architectures of n-i-p perovskite cells using F4-TCNQ doped (a) Spiro-OMeTAD, (b) PTAA, and (c) PEDOT: PSS HTLs, and (d-f) the J-V curves their corresponding device.

We then fabricated proof-of-concept n-i-p tandem devices using PEDOT: PSS as the interconnecting HTL of the top sub-cell (Figure 21). An n-i-p tandem cell delivers a V_{OC} of 1.836 V, a J_{SC} of 6.518 mA/cm^2, a FF of 42.8%, and a PCE of 5.12% (Figure 21b). Note that a single-junction n-i-p $MAPbI_3$ cell with PEDOT: PSS as the HTL usually shows a V_{OC} of ~0.9 V. The tandem V_{OC} of 1.836 V shows the superposition of two subcells. The photocurrent of the tandem cell is limited by the low current density generated by the 250 nm thick top absorber. Therefore, the performance parameters of the n-i-p tandem cell are reasonable despite the relatively low FF. Clearly, more work is needed to further improve the V_{OC} of the tandem cell to more than 2 V with high J_{SC} and FF to drive efficient water splitting.

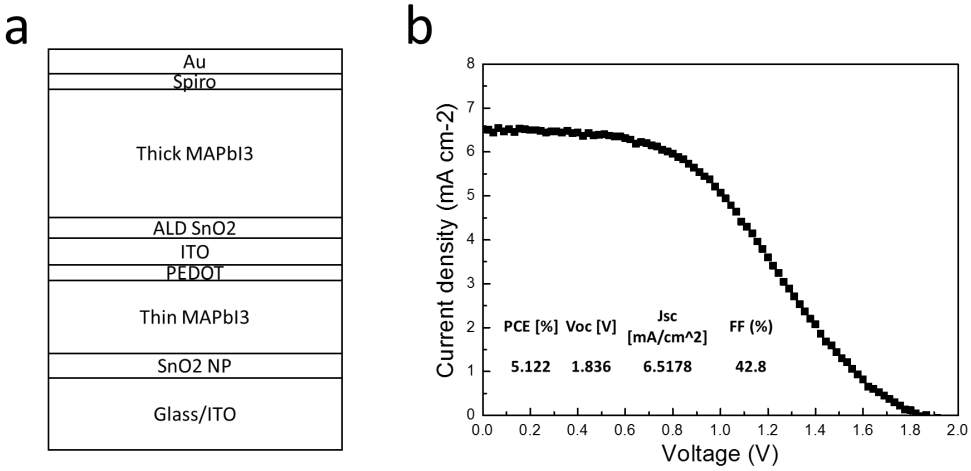

Figure 21. (a) Device configuration and (b) J-V curve of n-i-p tandem cells using PEDOT: PSS as the interconnecting HTL.

6. Pure-Pb-based perovskite-perovskite tandem photoelectrodes

In this activity, we fabricated two-terminal all-perovskite tandem solar cells consisting of two solution-processed perovskite subcells based on pure Pb-based perovskites. Compared with the conventional perovskite/perovskite tandem cells employing a lower bandgap mixed Sn-Pb bottom cell, our pure Pb-based perovskite tandem cells hold the promise of higher stability against ambient air and heat and a higher V_{OC}. The champion device exhibits a PCE of 19.2% with a high V_{OC} of 2.15 V. Owing to the high PCEs and photovoltages, all-perovskite tandem solar cells are investigated for photovoltaic-electrolysis (PV-EC) water-splitting applications. We further demonstrated unassisted PV-EC water splitting using these pure Pb-based all-perovskite tandem solar cells.

The complete perovskite/perovskite tandem device structure is shown in Figure 22. In brief, a 20 nm poly(triaryl)amine (PTAA) hole transport layer (HTL) was spin-coated on clean pre-patterned indium tin oxide (ITO) coated glass substrates. A 300 nm wide-Eg $FA_{0.8}Cs_{0.2}PbBr_1I_2$ perovskite was then spin-coated on the PTAA layer, followed by the deposition of electron transport layers (ETLs) consisting of 20 nm C_{60} and 15 nm SnO_2 prepared by thermal evaporation and atomic layer deposition (ALD), respectively. Next, a 110 nm interconnecting ITO layer was deposited by radio-frequency sputtering. A 60 nm poly(3,4-ethylenedioxythiophene) polystyrene sulfonate (PEDOT: PSS) HTL was spin-coated on the sputtered ITO layer. A 600 nm $FA_{0.7}MA_{0.3}PbI_3$ bottom absorber was prepared by spin-coating, followed by the same ETLs as in the top subcell. Finally, an 80 nm Ag back electrode was deposited by thermal evaporation. The thickness of each component layer was measured by spectroscopic ellipsometry. The active device area is 0.12 cm^2, defined by the patterned electrodes.

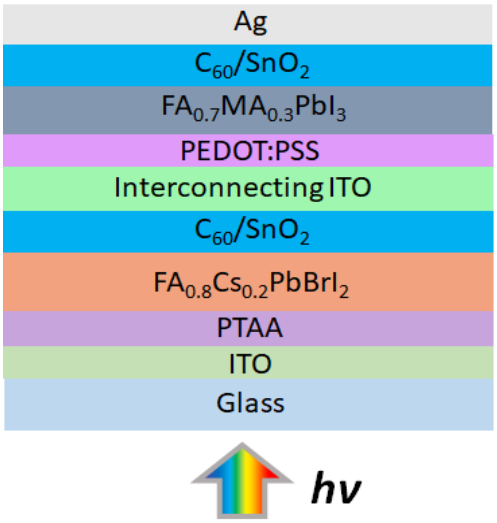

Figure 22. Schematic device structure of a perovskite/perovskite tandem cell.

Figure 23a shows the J-V curve of a 2-T all-perovskite tandem cell consisting of pure-Pb perovskite absorbers. The cell delivers a PCE of 19.2%, with a high V_{OC} of 2.153 V, a J_{SC} of 11.13 mA/cm2, and a fill factor (FF) of 80%. The device exhibits negligible hysteresis under the

reverse and forward scans. The high V_{OC} value of 2.15 V is close to the sum of the two subcells (1 and 1.15 V, respectively). The EQE measurements were carried out with red/blue biased light to detect the spectral response of top/bottom subcells. Figure 23b shows the EQE curves of the two subcells in a tandem device. The integrated photocurrent densities are determined to be 14.2 and 10.2 mA/cm^2 for the top and bottom subcells, respectively. It is worth noting that the photocurrent mismatch is mainly due to the not sufficiently high bandgap (~1.8 eV) of the top perovskite absorber. Moreover, the photocurrent mismatch and lateral conductivity of the interconnecting ITO layer make the pseudo-shunting behavior of the tandem device close to zero bias. Clearly, absorber bandgap and thickness optimization are needed to improve the performance of the pure Pb-based all-perovskite tandem solar cells.

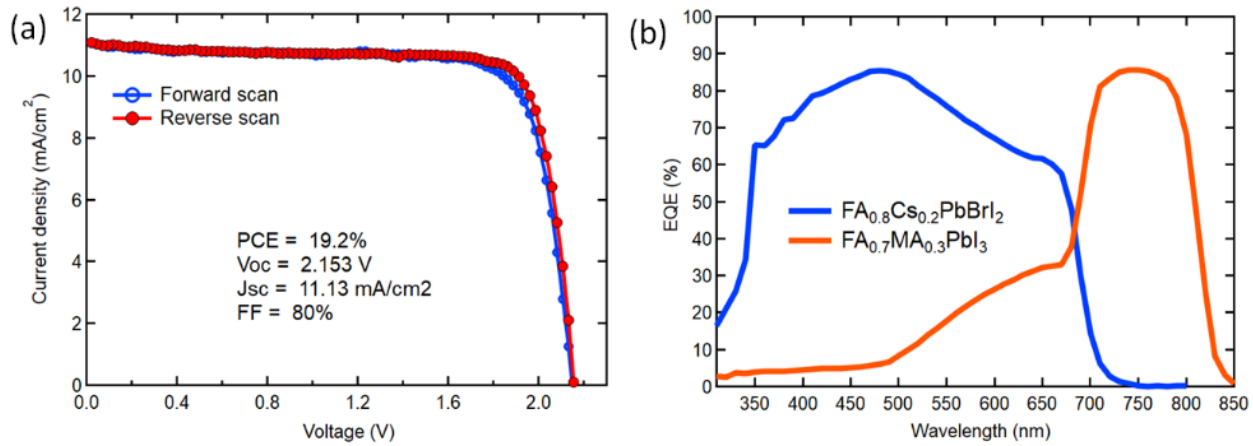

Figure 23. (a) J-V and (b) EQE of a typical all-perovskite tandem solar cell.

The preliminary PV-EC characterization was carried out using a Voltalab potentiostat and a three-electrode configuration in a 0.5 M sulfuric acid electrolyte (PH = ~0.3), with a Pt wire as the cathode, an IrOx coated Ni foil as the anode, an Ag/AgCl reference electrode. The illumination source was a 300 W Xe lamp calibrated and equipped with AM 1.5G filter.

Figure 24 shows a linear scan voltammogram (LSV) curve of a PV-EC system powered by a perovskite/perovskite tandem solar cell under AM 1.5G one sun illumination. The recorded potential versus Ag/AgCl reference potential was converted into potential against reversible hydrogen electrode (RHE) using the Nernst equation (1) given below:

$$E_{RHE} = E_{Ag/AgCl} + 0.059 \times pH + 0.1976\ V$$

Note that the PV-EC device shows an onset voltage (Von) of ~2.1 V vs. RHE, and the photocurrent density at zero bias vs. RHE is 10.5 mA/cm^2, consistent with the PV characterization. Figure 24b shows the chopped LSV of a two-electrode PV-EC system in a 0.5 M sulfuric acid electrolyte (PH = ~0.3), powered by a perovskite tandem solar cell under one sun illumination and dark conditions. The measurement result clearly demonstrates that pure Pb-based all-perovskite tandem solar cells can provide sufficient photovoltage to overcome the water electrolysis potential and, therefore, can be used for unassisted water splitting. The

maximum photocurrent density of the PV-EC system is ~7 mA/cm^2 at zero bias which suggests a solar-to-hydrogen (STH) efficiency of ~8.5% for these tandem devices. However, STH efficiency needs to be accurately determined under standard measurement protocols by the NREL EMN node.

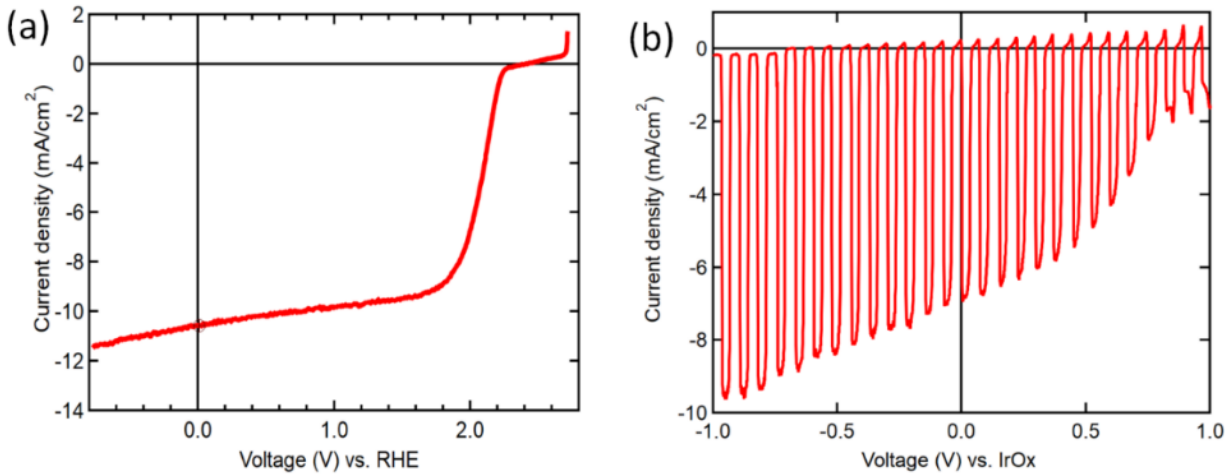

Figure 24. Linear sweep voltammetry scans of PV-EC systems powered by a perovskite/perovskite tandem solar cell, including (a) a three-electrode configuration with a Pt cathode working electrode, an IrOx anode counter electrode, and an Ag/AgCl reference electrode under continuous illumination and (b) a two-electrode configuration with a Pt cathode and an IrOx anode under chopped illumination. The electrolyte is 0.5 M sulfuric acid (PH = ~0.3).

The perovskite tandem photoelectrode was then encapsulated using epoxy rinses and soaked into an aqueous near-neutral electrolyte with Na_2SO_4 (PH = 6.5) for water stability test. The cathode contact of the perovskite tandem cell was fully covered by silver epoxy to prevent water ingress into the PV device, while the other contact was connected to an FTO/IrO_x anode by a Cu wire. Figure 25 shows that our perovskite tandem devices demonstrated relatively stable operation in water for more than 100 hours. Further work is needed to improve the stability of all-perovskite photoelectrodes.

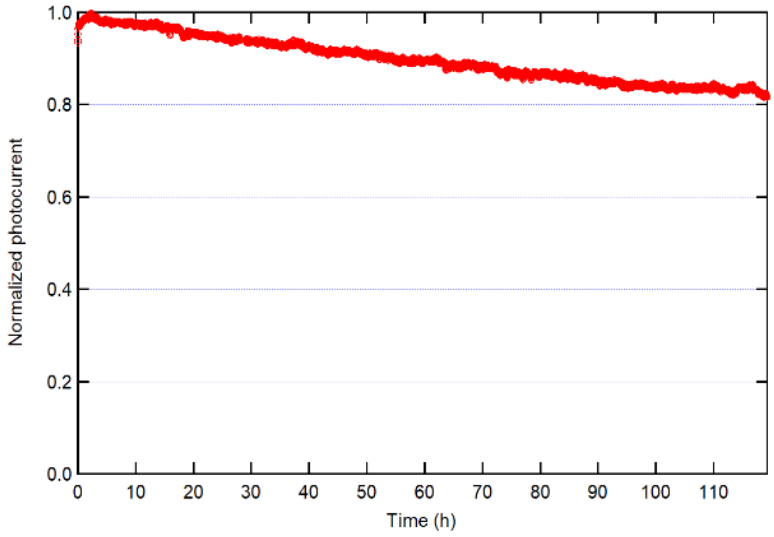

Figure 25. Normalized photocurrent of a p-i-n structured all-perovskite tandem photoelectrode in near-neutral aqueous electrolyte (PH = 6.5).

7. Optimization of interconnection layer for tandem devices

The fabrication of Pb-based all-perovskite tandem photoelectrodes accompanies higher annealing temperatures (180 and 150 ˚C) than the conventional mixed Sn-Pb ones (100 ˚C). At such a high temperature, the commonly used hole-blocking material, BCP, aggregates. Therefore, it needs to be replaced by a more robust material. Thermal-assisted ALD SnO_2 provides good hole-blocking properties and much improved thermal stability. In this activity, we optimized the ALD SnO_2 ETL based on the device structure of Glass/FTO/PTAA/$FAPbI_3$/C_{60}/ALD SnO_2/Ag. Figure 26 shows that the V_{OC} of the devices slightly increases along with the increase of the ALD deposition cycle from 15 to 40, while FF decreases and J_{SC} remains unchanged. Combined with the S-kink features shown in Figure 27 for the 30- and 40-cycle devices, we speculate that longer ALD deposition time induces the generation of PbI_2 on the grain boundaries, which passivates defects and increases V_{OC}. However, the formation of an insulative SnO_x layer caused by the low-quality ALD SnO_2 is not desirable for high-quality perovskite tandem photoelectrodes and thus needs to be eliminated.

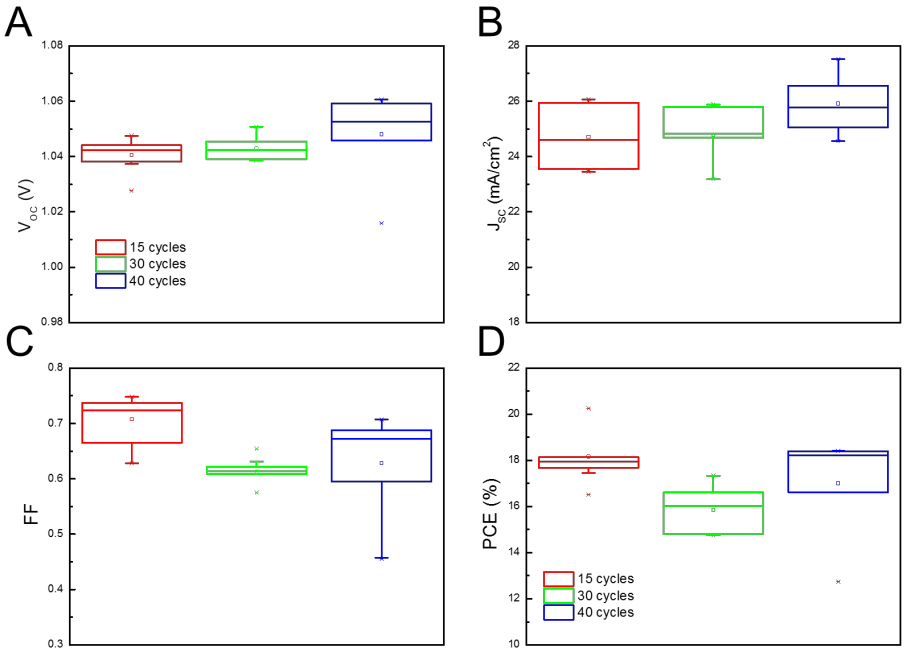

Figure 26. V_{OC} (A), J_{SC} (B), FF (C) and PCE (D) of $FAPbI_3$ photoelectrodes based on ALD SnO_2 with different cycles.

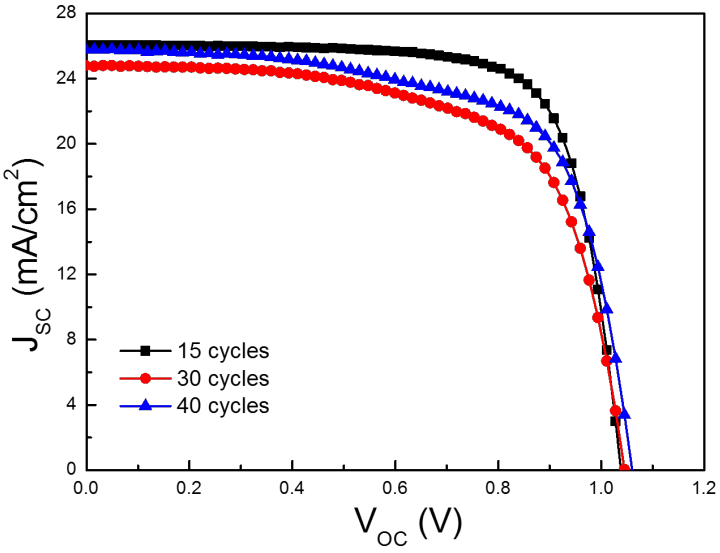

Figure 27. J-V curve of $FAPbI_3$ photoelectrodes based on ALD SnO_2 with different cycles.

To solve this issue, we conducted ALD SnO_2 deposition with a relatively high base pressure (~0.1 Torr) to increase the reaction time for the synthesis of high-quality SnO_2 layers. As can be

seen in Figure 28, the devices with different ALD SnO_2 cycles cause no change in terms of FF, J_{SC}, and V_{OC}. More interestingly, the J-V curves in Figure 29 indicate that 15- to 40-cycle of ALD SnO_2 at the relatively high base pressure doesn't cause S-kink features, which is ascribed to the improved quality of the SnO_2 layer.

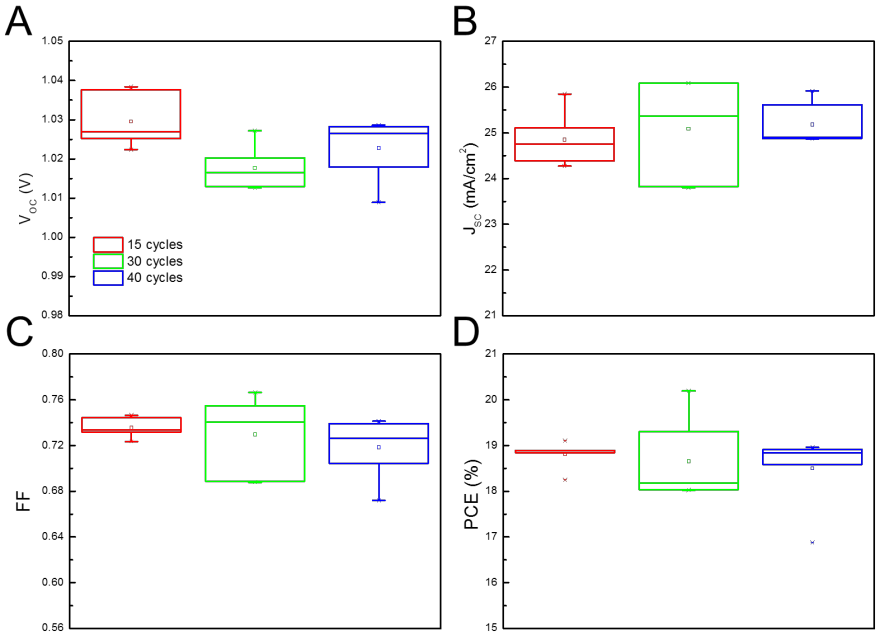

Figure 28. V_{OC} (A), J_{SC} (B), FF (C) and PCE (D) of $FAPbI_3$ photoelectrodes based on different cycled ALD SnO_2 without turbo pump.

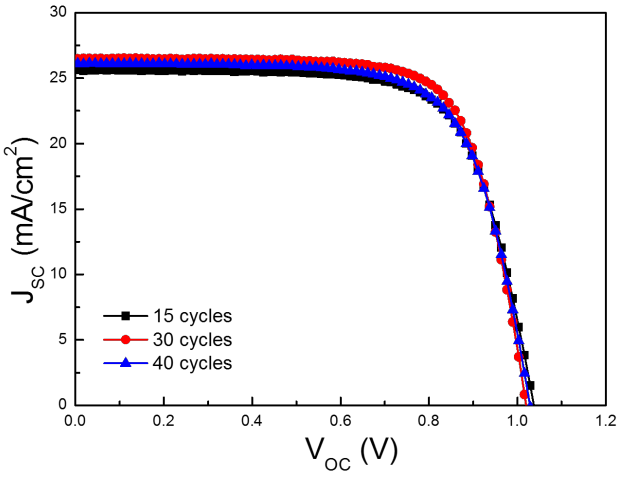

Figure 29. J-V curve of $FAPbI_3$ photoelectrodes based on different cycled ALD SnO_2. without turbo pump.

To double-check the advantages of the ALD SnO_2 at a relatively high base pressure, we further fabricated devices with increased deposition cycles to 80. As can be seen from Figure 30, the devices with 60-cycle SnO_2 show similar performance with 40-cycle ones, which confirms the effectiveness of ALD SnO_2 without turbopump. However, when the cycle further increased to 80, the FF of the devices decreased dramatically, which is likely due to the high series resistance caused by the thicker SnO_2 layer. By optimizing the ALD SnO_2 deposition conditions as we discussed above, we successfully fabricated $FAPbI_3$ photoelectrodes with an average V_{OC} of 1.02 V, a J_{SC} of 25 mA/cm^2, a FF of 70%, and a PCE of 19%.

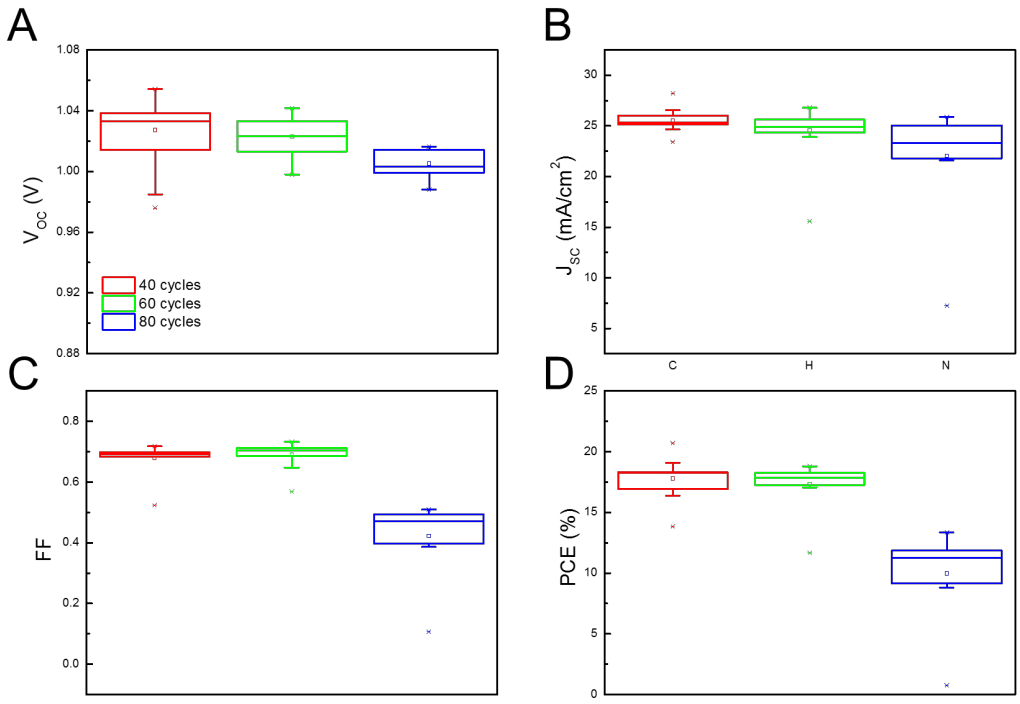

Figure 30. V_{OC} (A), J_{SC} (B), FF (C) and PCE (D) of $FAPbI_3$ photoelectrodes based on ALD SnO_2 with more deposition cycles.

To test the intrinsic device stability of $FAPbI_3$ bottom photoelectrodes at an elevated temperature (85 ˚C), we fabricated ITO/PTAA/$FAPbI_3$/C_{60}/SnO_2/ITO devices and tracked the device stability evolution. The devices were kept in a hotplate at 85 ˚C in a nitrogen glovebox and were taken out to ambient air for the PV measurement periodically. Figure 31 shows the evolution of normalized PCE of a $FAPbI_3$ photoelectrode. The device retained 90% of its initial PCE after thermal aging at 85 ˚C for more than 100 hours.

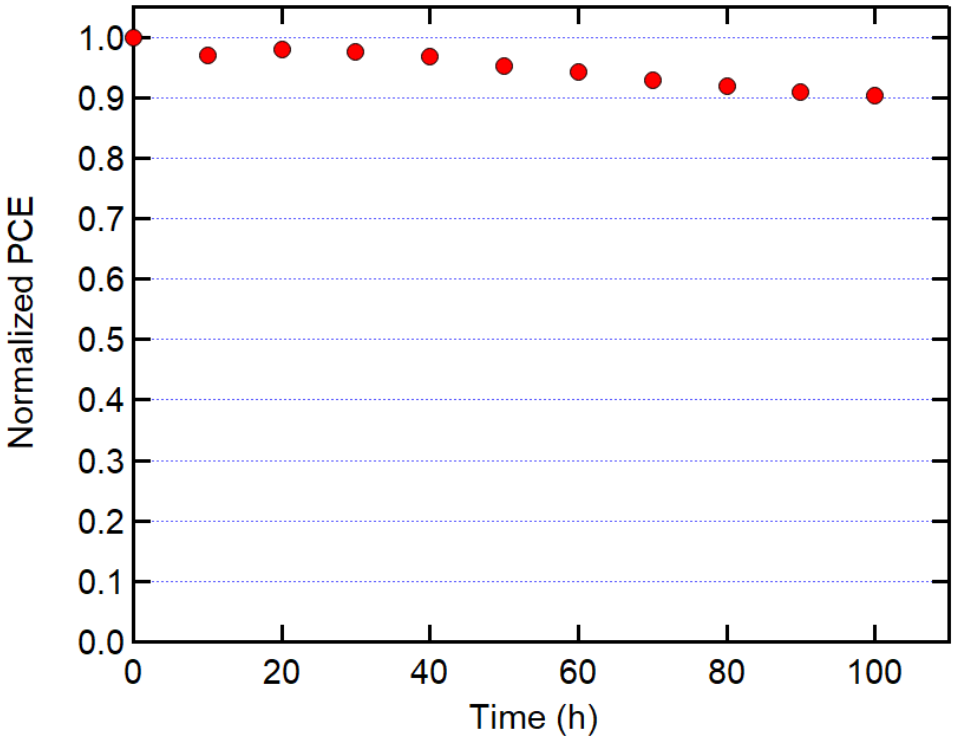

Figure 31. Evolution of the normalized PCE of a $FAPbI_3$ photoelectrode aged at 85 ˚C.

ITO interconnection layer enables the stack of solution-processed perovskite layers by preventing the penetration of precursor solutions. We optimized the sputtered ITO interconnecting layers for our Pb-based all-perovskite tandem photoelectrodes by varying the sputtering time. As can be seen from Figure 32, along with the sputtering time from 105 to 150 minutes, the ITO color changes from green to purple, which results from the different optical reflections by the increasing ITO thickness. All the ITO layers show even and dense morphologies.

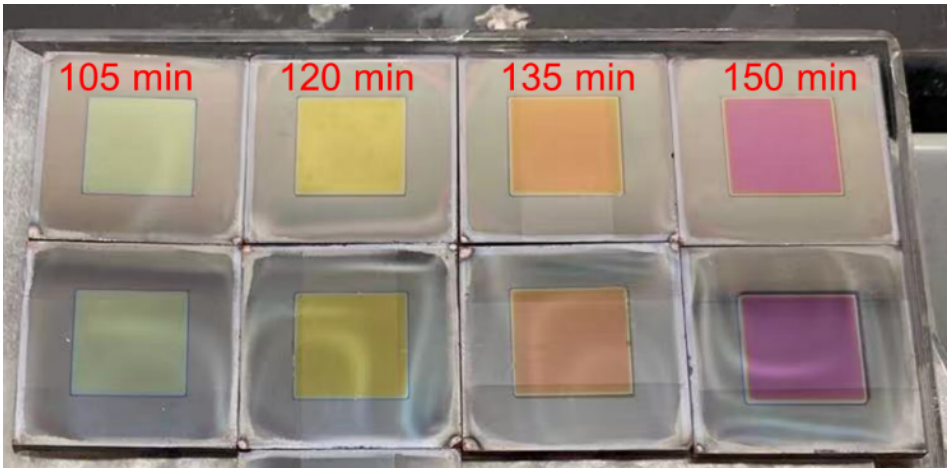

Figure 32. Photos of sputtered ITO on $CsPbI_2Br$ sub-cells with different sputtering times.

We fabricated Pb-based all-perovskite tandem photoelectrodes under the configuration of Glass/FTO/NiO_x/P3CT/$CsPbI_2Br$/C_{60}/SnO_2/Sputter ITO/PEDOT:PSS/$FAPbI_3$/C_{60}/SnO_2/Ag with different ITO interconnection layers (Figure 33A). As can be seen from Figure 33B to E, when the sputtering time increases from 105 to 135 minutes, V_{OC}, J_{SC}, and FF all show an increasing trend, which indicates improved ITO layer quality without sacrificing optical transparency and inducing leakage current. When the sputtering time further increased to 150 minutes, both the V_{OC} and J_{SC} for the devices decease, which are typical consequences of the reduced light intensity and prominent leakage current caused by thick ITO layers.

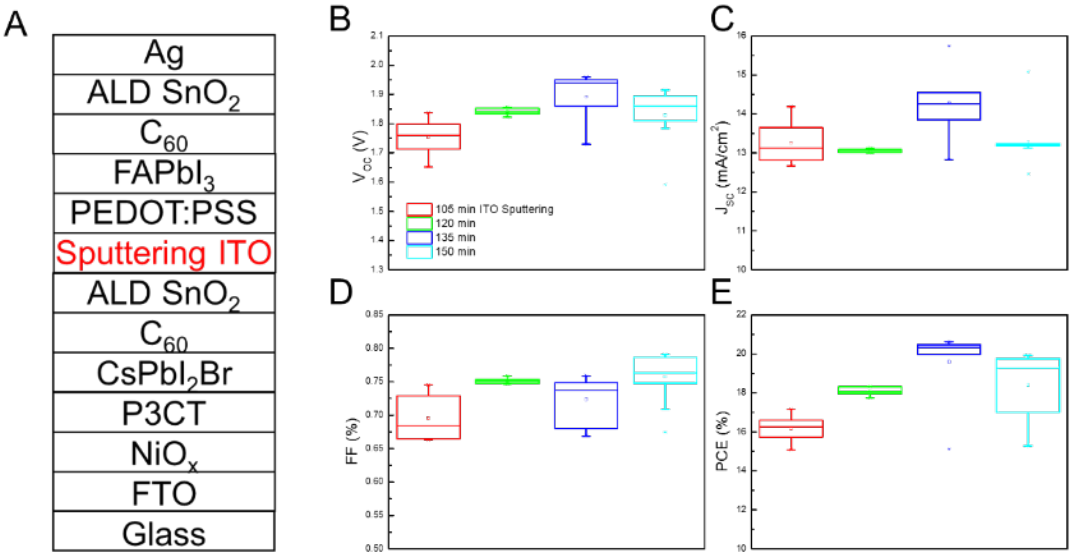

Figure 33. Device configuration (A) and detailed parameters (B) to (E) of our Pb-based all-perovskite tandem photoelectrodes.

By all the optimization works that we have discussed in this quarterly report, we are now able to make efficient Pb-based all-perovskite tandem photoelectrodes with superior air stability. As can be seen in Figure 34, our best Pb-based all-perovskite tandem photoelectrode shows a PCE of 21.17 (18.88)% with a V_{OC} of 2.11 (2.05) V, a J_{SC} of 12.40 (12.29) mA/cm^2, a FF of 80.9 (74.9)% under the reverse (forward) scan direction. What should be noted here is that our Pb-based tandem photoelectrodes are stable in low-humidity air, which is more significant for the practical water-splitting application.

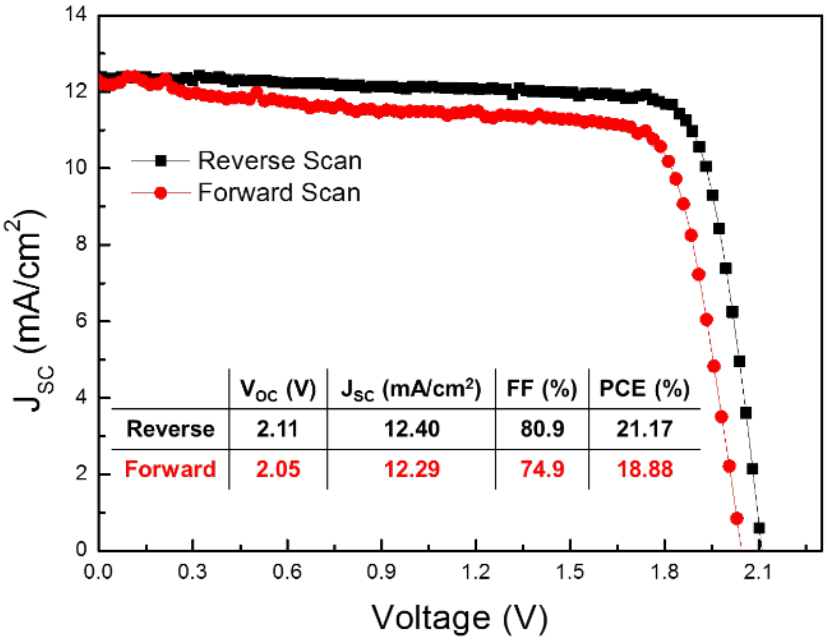

	V_{OC} (V)	J_{SC} (mA/cm^2)	FF (%)	PCE (%)
Reverse	2.11	12.40	80.9	21.17
Forward	2.05	12.29	74.9	18.88

Figure 34. J-V curve of our best Pb-based all-perovskite tandem photoelectrodes.

8. Improving All-Pb-based tandem photoelectrodes

After achieving some preliminary results of the Pb-based $CsPbI_2Br/FA_{0.95}Cs_{0.05}PbI_3$ tandem photoelectrodes with a higher open-circuit voltage and improved photostability than conventional Pb/Sn-Pb tandem perovskite photoelectrodes. We continued our effort in improving the tandem device performance and investigating the tandem device working mechanism.

We first investigated the impact of poly[3-(4-methylamine carboxylbutyl)thiophene] (P3CT-N) surface modification on the NiO_x hole-transport layer (HTL) of wide-bandgap perovskite solar cells (PSCs) with a p-i-n structure as shown in Figure 35A. P3CT-N is a polymer containing a carboxyl group at the end of one sidechain and a thiophene end group on the other side. The deposition of P3CT-N on NiO_x was confirmed by the detection of the sulfur (S) 2-s peak in X-ray photoelectron spectroscopy (XPS) measurements (Figure 35B).

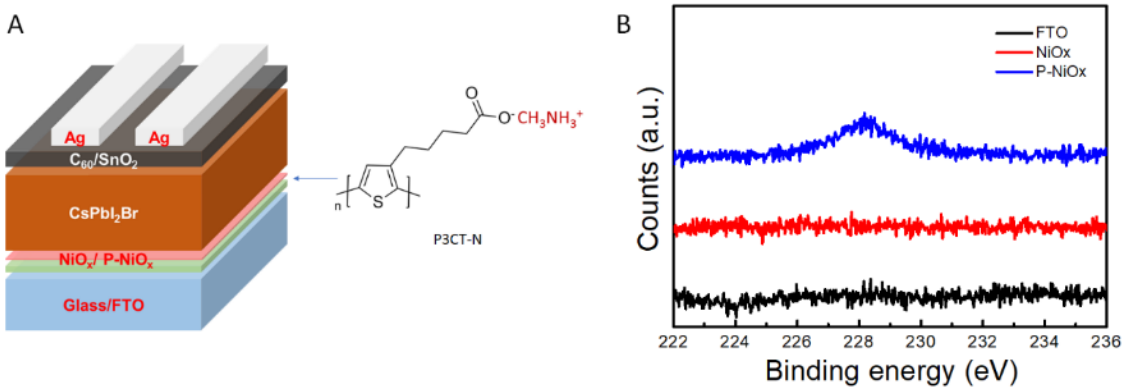

Figure 35. (A) Device structure of wide-bandgap perovskite structure and the chemical structure of P3CT-N. (B) X-ray photoelectron spectroscopy (XPS) measurements of NiO_x film with and without P3CT-N modification.

Kelvin probe force microscopic (KPFM) scanning shows that the P3CT-N coating significantly modifies the surface potential of the underlying NiO_x films. The pristine NiOx film shows significant heterogeneity in surface potential across the measured area (Figure 36A). Particularly, a substantial-high contrast is observed at the grain boundaries (GBs) following the profile of the underlying fluorine doped tin oxide (FTO) coated glass substrate, showing spatial nonuniformity in the electrical properties of as-deposited NiO_x films. In contrast, the modified NiO_x film exhibits much smoother and more uniform surface potential (Figure 36B). Figure 36C quantify the surface potential uniformity in term of standard deviation. The more uniform potential distribution of the modified NiO_x indicates efficient defect passivation. The defects can involve point defects, extended defects, defect aggregations, and grain boundaries (GBs), that trap electrical charges and cause non-radiative recombination. Moreover, a uniform interfacial layer is beneficial for lowering the energy loss due to the surface potential fluctuation at the HTL/perovskite interface.

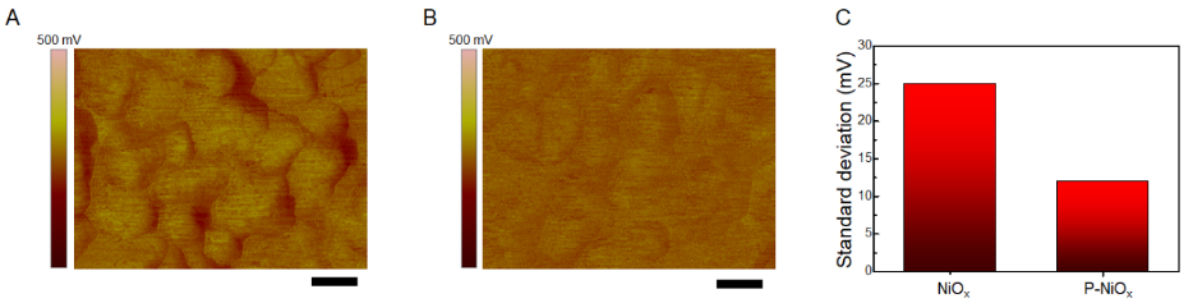

Figure 36. (A and B) Kelvin probe force microscopic (KPFM) images of NiO_x and modified NiO_x films. The scale bar is 100 nm. (C) Standard deviation of the surface potential distribution of NiO_x and modified NiO_x films.

To precisely measure the energy levels of NiO_x and the modified NiO_x, we conducted ultraviolet photoelectron spectroscopy (UPS) and spectroscopic ellipsometry (SE) measurements. The work function (WF) and ionization energy (IE) of NiO_x are fitted to be 4.71 and 5.34 eV, as shown in Figure 37A and B. After the P3CT-N modification, the WF increases to 4.83 eV, and the IE downshifts to 5.49 eV. Figure 37C illustrates the corresponding energy levels of different component layers in a $CsPbI_2Br$ PSC, showing a more favorable band alignment of the modified NiO_x HTL with $CsPbI_2Br$ than NiO_x. The deeper work function of the HTL after the P3CT-N modification is expected to enhance hole extraction and reduce non-radiative recombination at the HTL/perovskite interface, suppressing the photovoltage loss due to Fermi energy pinning at the HTL/perovskite interface.

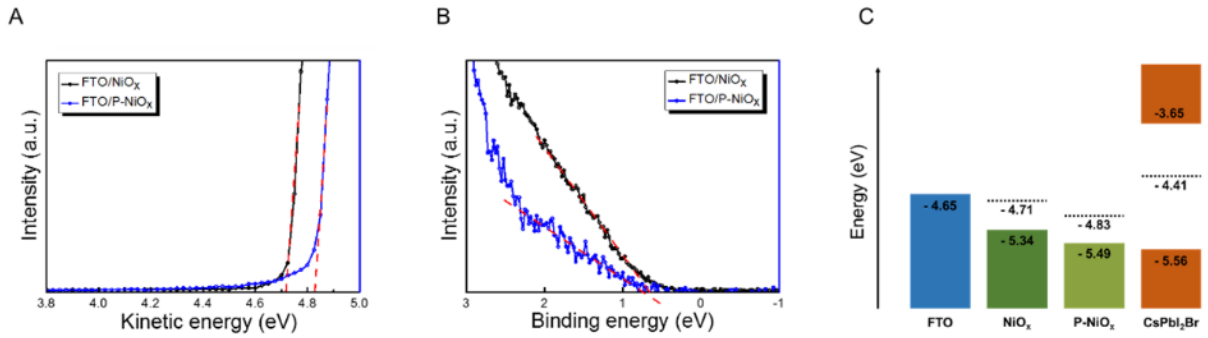

Figure 37. (A and B) Ultraviolet photoelectron spectroscopy (UPS) measurements of NiO_x and modified NiO_x films. (C) Energy levels of $CsPbI_2Br$ made on NiO_x and modified NiO_x-coated FTO substrates.

Steady-state photoluminescence (PL) and time-resolved PL (TRPL) measurements were conducted through illuminating from the glass and perovskite film sides separately to evaluate the photophysical behaviors in the perovskite films deposited on NiOx and modified NiOx HTLs (Figure 38A). The PL peaks at ~650 nm verify the bandgap of $CsPbI_2Br$ at about 1.91 eV. It is worth noting that the PL emission of most wide-bandgap organic-inorganic mixed halide perovskites exhibits a redshift compared with the absorption edge due to the photoinduced halide segregation. The consistency in the PL and absorption reflected in k from spectroscopic ellipsometry of $CsPbI_2Br$ confirms its better stability against phase segregation. We then conducted the PL/TRPL measurements from the glass side to study the hole extraction at the HTL/$CsPbI_2Br$ interface. As seen in Figure 38B and C, the $CsPbI_2Br$ films prepared on HTLs show quenched PL intensity and a shorter TRPL lifetime compared with the $CsPbI_2Br$ film prepared on a bare glass substrate, which is attributed to the efficient hole extraction by HTLs. The quenching effect is more pronounced for the modified NiO_x/$CsPbI_2Br$ than NiO_x/$CsPbI_2Br$, indicating improved hole extraction after surface modification by P3CT-N.

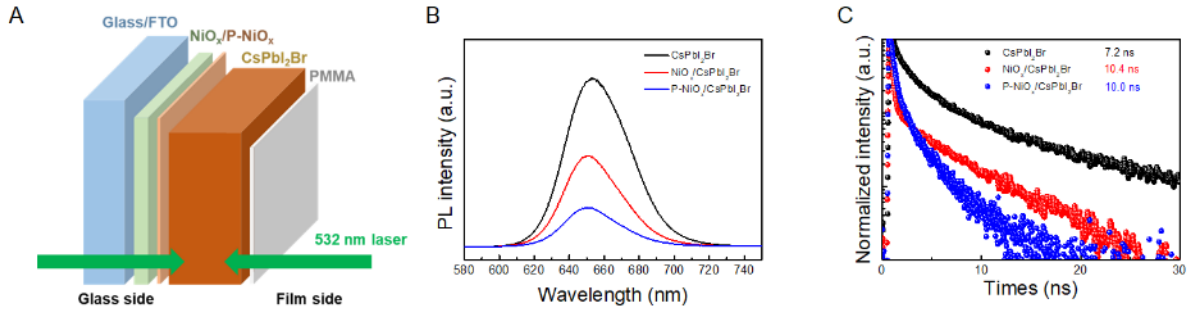

Figure 38. (A) Schematic diagram of photoluminescence (PL) and time resolved PL (TRPL) measurements from different directions. (B) PL results of $CsPbI_2Br$ thin films made on NiO_x and modified NiO_x HTLs and measured from the glass side. (C) TRPL results of $CsPbI_2Br$ thin films made on NiO_x and modified NiO_x HTLs and measured from the glass side.

To evaluate the effect of the P3CT-N modification on solar cell performance, $CsPbI_2Br$ PSCs with the p-i-n device configuration of glass/FTO/NiO_x or modified NiO_x/$CsPbI_2Br$/C_{60}/SnO_2/Ag were fabricated. The device performance of $CsPbI_2Br$ PSCs based on NiO_x and modified NiO_x HTLs are statistically compared in Figure 39A. $CsPbI_2Br$ PSCs with the NiO_x HTL show an average PCE of ~12%, with a V_{OC} of ~1.18 V, a J_{SC} of ~14.2 mA/cm^2, and a FF of ~72%, while the devices with the modified NiO_x HTL deliver an average PCE of ~15%, with V_{OC}, J_{SC}, and FF improved by ~60 mV, ~1.2 mA/cm^2, and 4%, respectively. The improved device performance is attributed to the enhanced hole extraction and reduced non-radiative combination at the HTL/$CsPbI_2Br$ interface. Figure 39B shows the current-voltage (J–V) curves of our best-performing $CsPbI_2Br$ PSCs with the NiO_x and modified NiO_x HTLs. The NiOx based device shows a PCE of 12.47% with a V_{OC} of 1.18 V, a J_{SC} of 14.42 mA/cm^2, and a FF of 73.2% under reverse voltage scan. The cell with the P3CT-N modification delivers an improved PCE of 15.26% with a V_{OC} of 1.25 V, a J_{SC} of 15.44 mA/cm^2, and a FF of 78.8%. The measured J_{SC} values were confirmed by external quantum efficiency (EQE) measurements (Figure 39C). The cell with P3CT-N modification shows an overall increase in EQE over the entire spectral range of 350 to 660 nm.

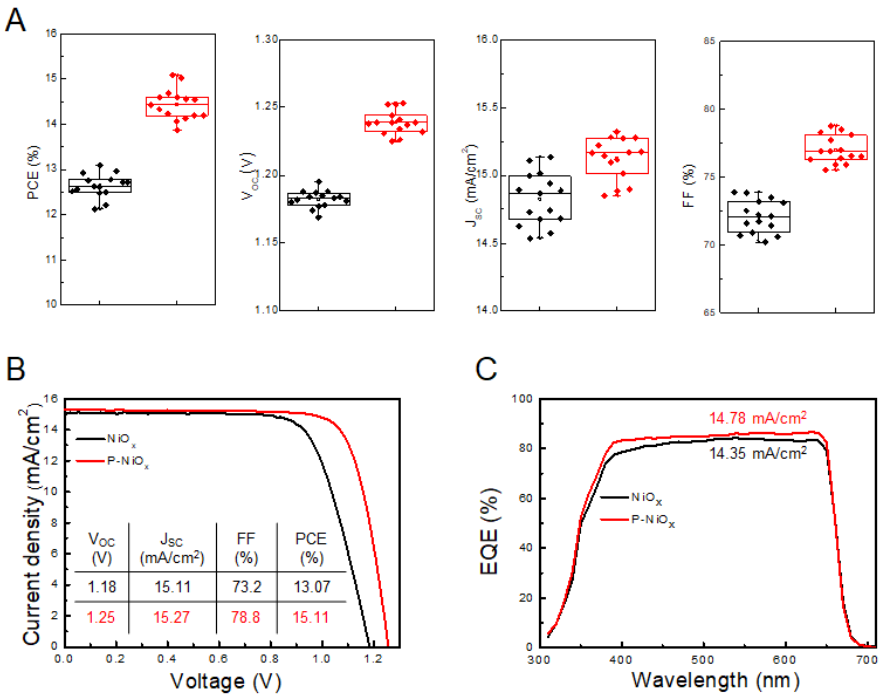

Figure 39. (A) Schematic diagram of photoluminescence (PL) and time resolved PL (TRPL) measurements from different directions. (B) PL results of $CsPbI_2Br$ thin films made on NiO_x and modified NiO_x HTLs and measured from the glass side. (C) TRPL results of $CsPbI_2Br$ thin films made on NiO_x and modified NiO_x HTLs and measured from the glass side. (D-G) Device performance statistics of $CsPbI_2Br$ PSCs fabricated on NiO_x and modified NiO_x HTLs. (H) Current-voltage (J-V) curves of champion $CsPbI_2Br$ PSCs fabricated on NiO_x and modified NiO_x HTLs. (I) External quantum efficiency (EQE) spectra of champion $CsPbI_2Br$ PSCs fabricated on NiO_x and modified NiO_x HTLs.

We further optimized the performance of our Pb-based perovskite/perovskite tandem photoelectrodes. The construction is depicted in Figure 40A: glass/FTO/NiO_x or modified NiO_x/$CsPbI_2Br$/C_{60}/SnO_2/ITO/PEDOT:PSS/$FA_{0.95}Cs_{0.05}PbI_3$/C_{60}/SnO_2/Ag, and a typical cross-sectional SEM image of the tandem devices is shown in Figure 40B. Figure 40C displays the wavelength-dependent light absorbance distribution in a tandem device with the optimal thickness combination, which demonstrates complementary light harvesting across the visible light and near-infrared range of the solar spectrum by $CsPbI_2Br$ and $FA_{0.95}Cs_{0.05}PbI_3$ perovskite absorber layers.

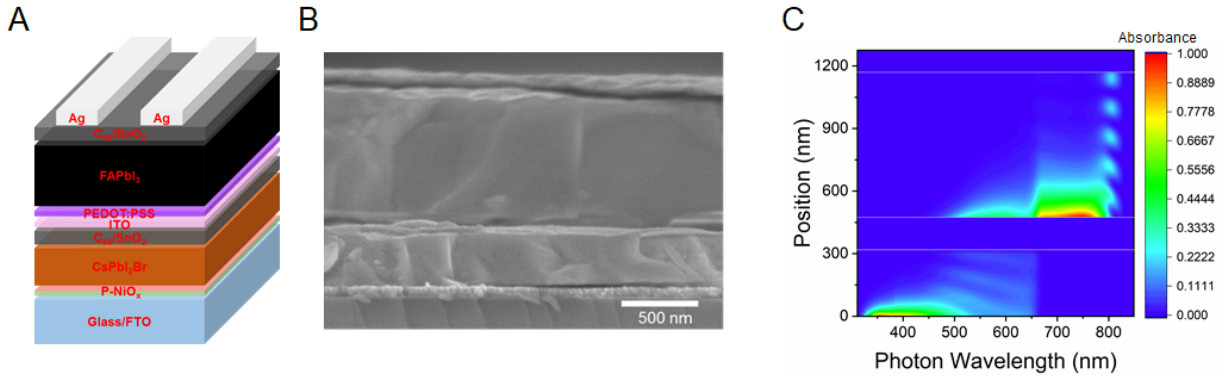

Figure 40. (A) Device sketch of a photoelectrode. (B) Cross-sectional SEM image of a photoelectrode. (C) Absorbance distribution in a photoelectrode.

Figures 41A compares the statistical PV parameters of photoelectrodes based on NiO_x and modified NiO_x, measured under reverse voltage scan. The photoelectrodes based on NiO_x show a V_{OC} of ~2.05 V, a J_{SC} of ~11.5 mA/cm^2, and a FF of ~77% to yield an average PCE of ~18%. The tandem devices based on modified NiO_x showed a higher PCE of ~21.5%, with a V_{OC} of ~2.13 V, a J_{SC} of 12.3 mA/cm2, and a FF of ~82% on average. Figure 41B shows the J-V curves of the best-performing photoelectrodes based on NiO_x and modified NiO_x. The champion cell with the P3CT-N modification exhibits a PCE of 22.20% with a V_{OC} of 2.15 V, a J_{SC} of 12.44 mA/cm^2, and a FF of 82.8%. The steady-state efficiency measurement of the tandem cell also shows a stable output of the device (Figure 41C). We further measured the J_{SC} generated in the two subcells by conducting EQE measurements under different light bias conditions (Figure 41D). The integrated J_{SC} for the top and bottom subcells are 12.31 and 12.05 mA/cm^2.

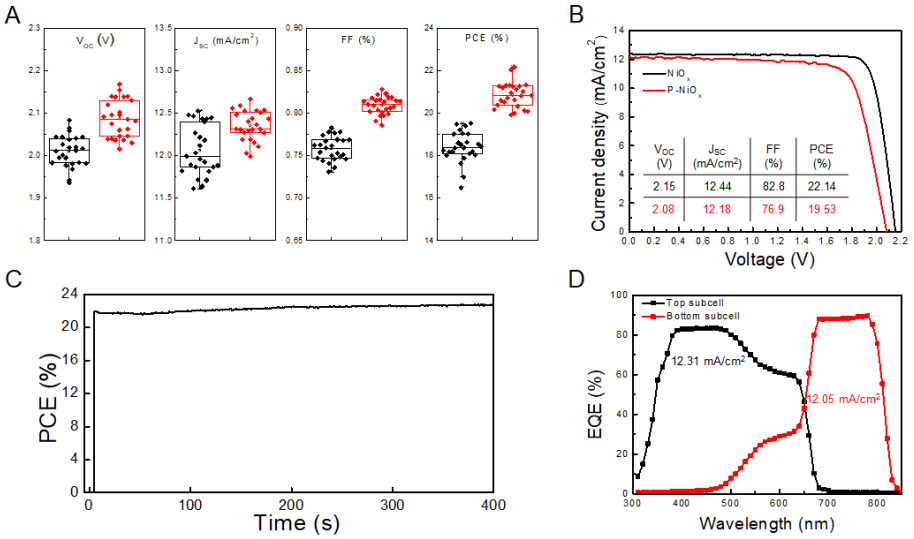

Figure 41. (A) Statistics of PV parameters of photoelectrodes fabricated on the NiOx and modified NiOx HTLs. (B) J-V curves of the best-performing photoelectrodes fabricated on the NiOx and modified NiOx HTLs. (C) Steady-state power output of the photoelectrode fabricated

on the modified NiOx HTL. (D) EQE curves of top and bottom cells of perovskite tandem photoelectrodes.

The inclusion of the P3CT-N interfacial modification also contributes to improved device stability. We first compared the thermal stability of $CsPbI_2Br$ PSCs by an accelerated aging test at 85 °C in an N_2-filled glovebox. Figure 42A shows the evolution of the PCE of $CsPbI_2Br$ PSCs measured periodically after the thermal aging. The cells with the modified NiO_x HTL exhibit much improved thermal stability than the NiO_x HTL devices. The rapid degradation in the NiO_x devices is mainly caused by the loss of J_{SC}. The PCE of a modified NiO_x based device remained unchanged for more than 100 h, whereas a NiO_x based cell retained only ~75% of its initial efficiency after 100 h of MPP tracking. The results show that light and thermal stresses can accelerate the degradation of $CsPbI_2Br$, presumably originating at the NiO_x/perovskite interface. The introduction of P3CT-N surface modification can isolate the NiO_x from the perovskite layer, preventing detrimental reactions between NiO_x and perovskites and effectively mitigating the thermal and photo degradation of perovskite layers. Benefiting from the stability advantages of the P3CT-N passivated $CsPbI_2Br$ top cell, our all-Pb photoelectrodes exhibit superior operational stability. Figure 42B shows that a tandem photoelectrode retained almost no change for more than 1600 hours of MPPT under one sun illumination at ~65 °C in the air, which is much improved compared with our conventional Pb/Sn-Pb tandem photoelectrodes.

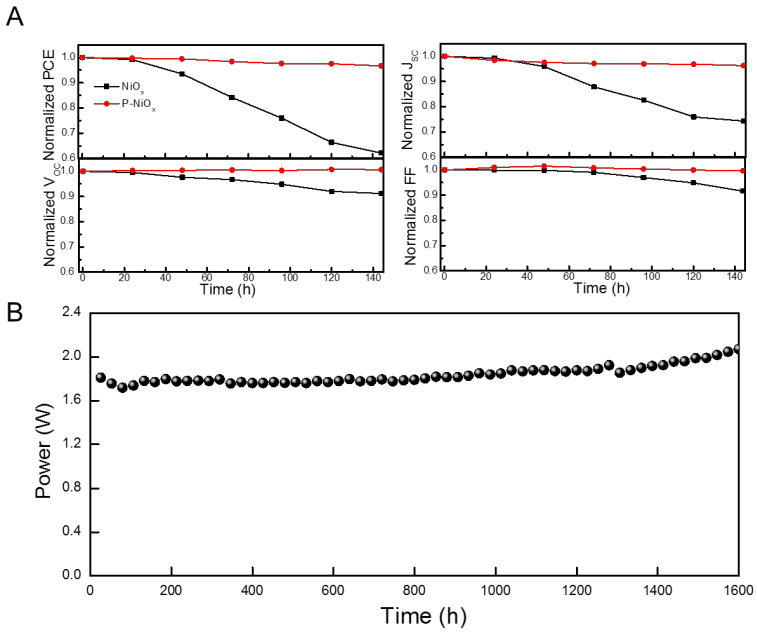

Figure 42. (A) Thermal stability of CsPbI2Br PSCs prepared on NiOx and modified NiOx HTLs. (B) MPP tracking of a photoelectrode tandem measured at ~65 °C in the air.

9. Perovskite/perovskite tandem photoelectrodes powered photovoltaic-electrochemical (PV-EC) devices for unassisted water splitting

In this activity, we demonstrated Pb-based perovskite/perovskite tandem photoelectrodes with a solar power conversion efficiency (PCE) of > 21%. In this quarter, we collaborated with the NREL EMN node to perform PV-EC characterization under standardized measurement protocols to determine the maximum possible STH efficiency of our perovskite/perovskite tandem photoelectrodes. Our perovskite/perovskite tandem photoelectrodes were fabricated with a device structure of glass/ITO/PTAA/wide-E_g perovskite/C_{60}/SnO_2/ITO/PEDOT:PSS/narrow-E_g perovskite/C_{60}/BCP/Cu following our previously reported procedures. The wide-E_g perovskite absorber layer has a general composition of $FA_{0.8}Cs_{0.1}MA_{0.1}Pb(Br_{0.3}I_{0.7})_3$, while two narrow-$E_g$ perovskites were used in the tandem photoelectrodes, including $FA_{0.9}Cs_{0.05}MA_{0.05}PbI_3$ and $MA_{0.3}FA_{0.7}Pb_{0.5}Sn_{0.5}I_3$, to compare the PEC performance.

Figure 43 shows the experimental setup for PV-EC measurements of our perovskite/perovskite tandem photoelectrodes, consisting of a light source with an AM1.5G filter, a chopper system, a photoelectrode, a multi-port electrolyzer, and electrical measurement tools, including multimeter, potentiostat, and computer. The simulated light intensity was first calibrated to 100 mW/cm^2 (corresponding to the AM 1.5G solar irradiance) using a certified Si reference cell. The test device was then mounted to the location with the calibrated light intensity (Figure 43, left). The cathode of the perovskite tandem photoelectrode was connected to a Pt electrode for hydrogen evolution reaction (HER), while the anode was connected to an IrO_x coated NiFeMo alloy (80:15:4.2 wt%) electrode for oxygen evolution reaction (OER). The reference electrode of Ag/AgCl ($E^0_{Ag/AgCl}$ = +0.197 V vs. NHE at 25 ˚C) was used for three-electrode measurements. The electrolyte solution was prepared using 0.5 M sulfuric acid with a PH value of 0.4. 100 µL of triton x-100 surfactant was added to the electrolyte solution to ensure that the evolved gas bubbles remained small and did not stick to the electrode surface.

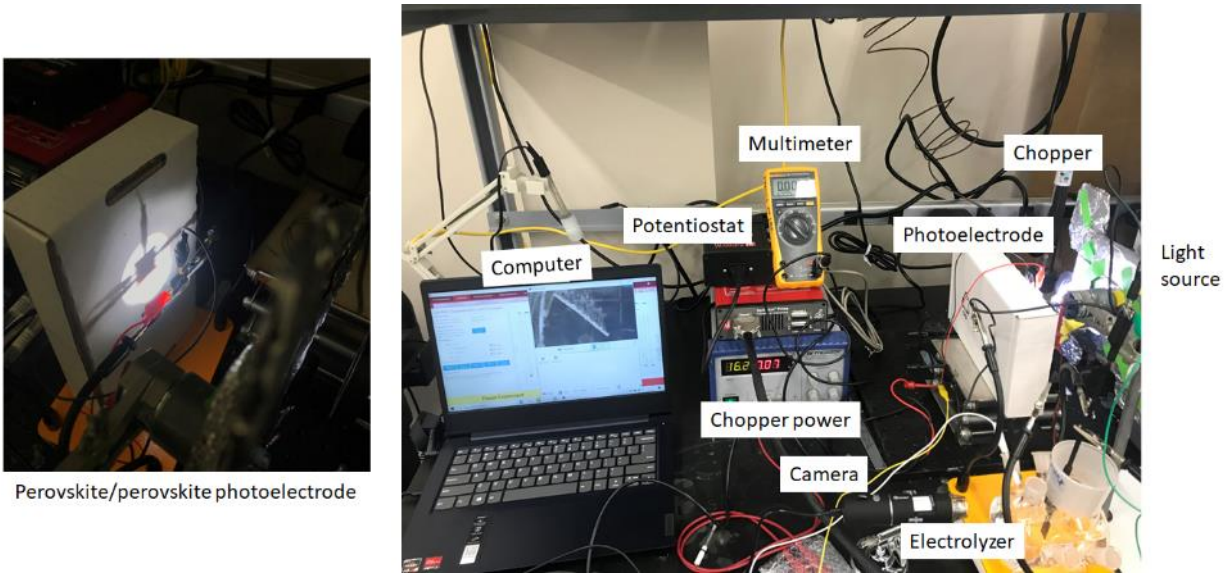

Figure 43. Photos of a perovskite/perovskite photoelectrode under illumination (left) and experimental setup for PV-EC measurements (right).

Figure 44 shows typical linear sweep voltammetry (LSV) curves of a Pb-based perovskite/perovskite photocathode in a three-electrode figuration under continuous and chopped illumination conditions. The experiment was carried out under a voltage sweep from open-circuit voltage to the reverse bias. The photo-responses of the perovskite tandem photoelectrode under continuous and chopped light are overlayed. The current density at the reversible potential for HER ($J^{\circ}_{E=HER}$), corresponding to 0 V vs. RHE, is determined to be 10.3 mA/cm^2. Thanks to the high photovoltage of the perovskite/perovskite tandem photoelectrode, the onset voltage for HER ($V_{onset,HER}$) is as high as ~2.07 V, allowing a wide potential range of photocurrent generation for HER. The photocurrent becomes almost saturated at voltages below 0.8 V vs. RHE, indicating a great potential to achieve unassisted water electrolysis using a two-electrode configuration.

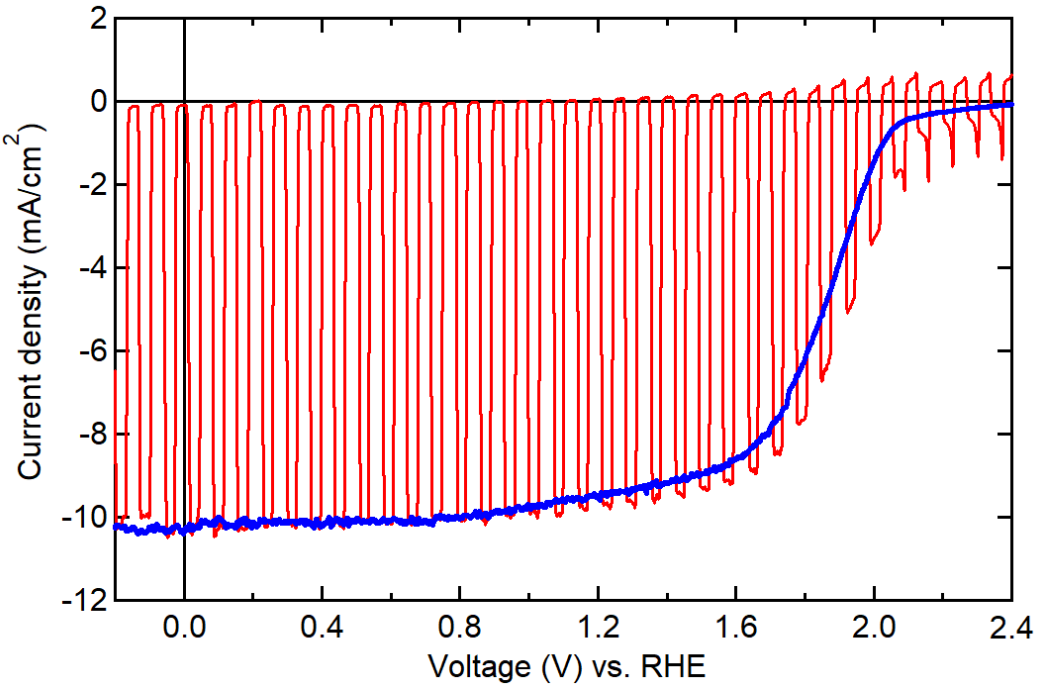

Figure 44. Linear sweep voltammetry curves of a Pb-based perovskite/perovskite photocathode in a three-electrode figuration under continuous and chopped illumination conditions.

STH conversion efficiency is the most important figure of merit to characterize the performance of a photoelectrode for PEC water splitting. The short-circuit photocurrent density (J_{SC}) as zero applied bias in a two-electrode configuration is critical in determining the STH conversion efficiency. Therefore, to determine the maximum possible STH of our perovskite/perovskite tandem photoelectrodes, we further conducted two-electrode PV-EC characterization. Figure 45a shows the LSV curve of a Pb-based perovskite/perovskite photocathode-powered PV-EV device in a two-electrode figuration under chopped AM1.5G illumination. The maximum photocurrent density at 0 V vs. IrOx is ~9.7 mA/cm^2 under AM 1.5G one sun illumination in 0.5 M H_2SO_4. Assuming every photogenerated electron and hole drive the HER and OER,

respectively, corresponding to Faradaic efficiency of 100%, the STH conversion efficiency for this perovskite tandem photoelectrode is estimated to be ~11.9%. To confirm the unassisted water splitting by the perovskite/perovskite tandem photoelectrodes, we conducted the chronoamperometry measurement at 0 V bias vs. IrO_x counter electrode under chopped AM1.5G illumination. Figure 45b shows a photo of an ongoing chronoamperometry test. Hydrogen bubble generation at the Pt electrode can be clearly seen in the photo captured by a camera. The PV-EC test demonstrates that the perovskite/perovskite tandem photoelectrodes can be potentially used for high-efficiency PEC water splitting.

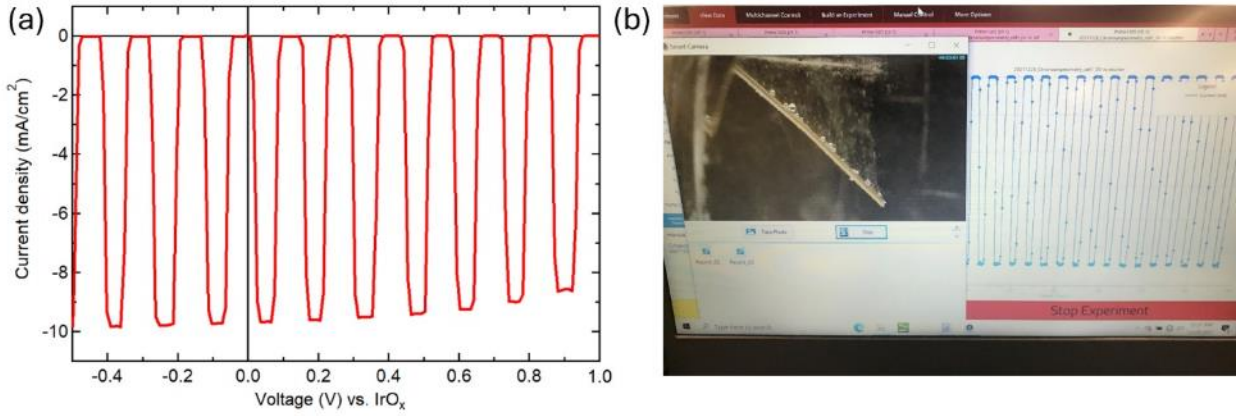

Figure 45. (a) Linear sweep voltammetry curve of a Pb-based perovskite/perovskite photocathode in a two-electrode figuration under chopped AM1.5G illumination. (b) Photo of a chronoamperometry measurement of unassisted water splitting powered by a perovskite/perovskite photoelectrode in two-electrode figuration at 0 V bias under chopped illumination. The camera captured hydrogen generation at the Pt electrode.

Motivated by the promising PV-EC performance of our perovskite/perovskite tandem photoelectrodes, we further fabricated wired perovskite tandem photoelectrodes, as shown in Figure 46. In brief, we integrated a stainless steel metal foil to the cathode (i.e., Ag back contact) of our tandem device using conductive Ag epoxy and soldered two Cu wires to the outer edge of the anode (i.e., ITO front contact). The perovskite tandem photoelectrode was then covered by non-conductive epoxy to ensure electrical and chemical isolation from the electrolyte except for the active area of the working electrode surface.

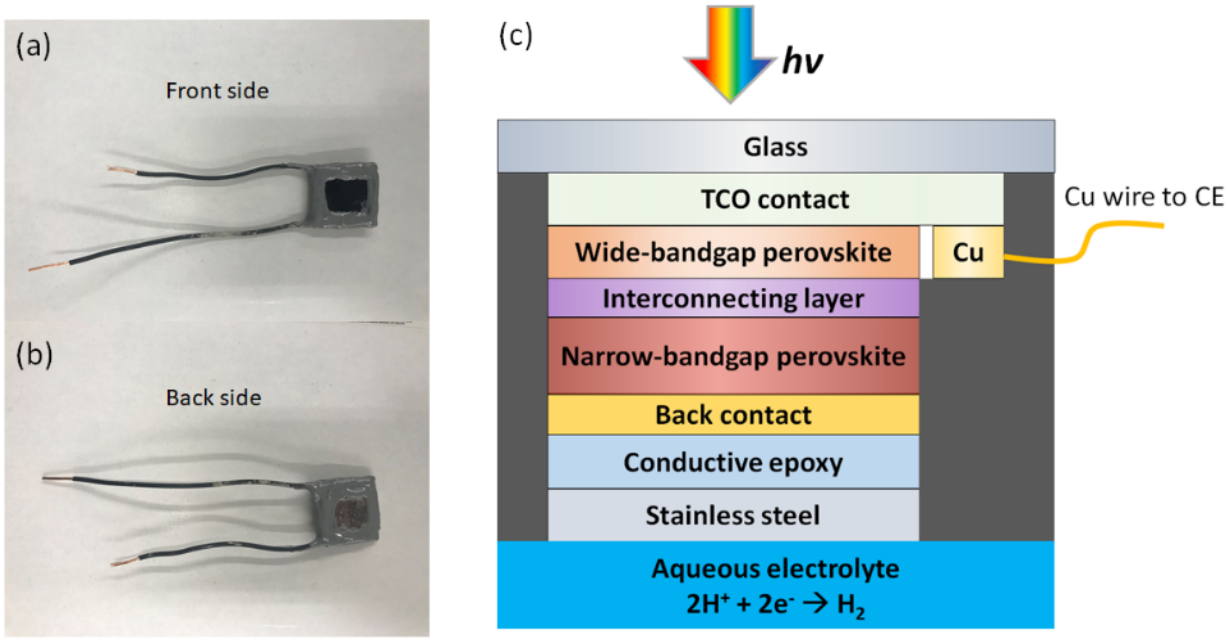

Figure 46. Photos of the (a) front and (b) back side of a wired perovskite/perovskite photoelectrode. (c) Schematic of a wired perovskite/perovskite photoelectrode

We then tested the performance of our wired perovskite/perovskite photoelectrode in a PEC setup, as shown in Figure 47. The PEC cell consists of a perovskite/perovskite tandem photocathode as the working electrode, an Ag/AgCl reference electrode, and a Pt wire counter electrode. Although Pt is not the desired OER counter electrode, the three-electrode measurement is just a hall-cell reaction whose metrics are affected by the counter electrode material.

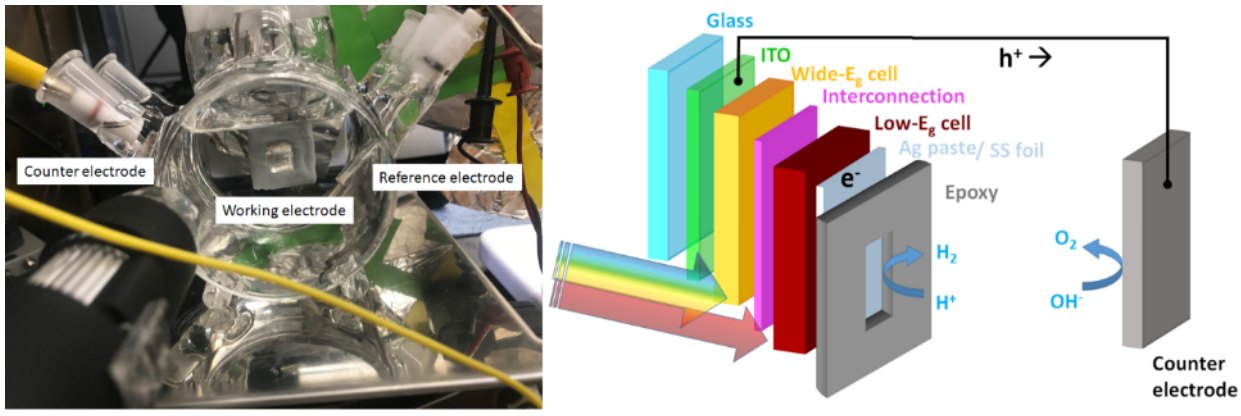

Figure 47. Photo of a PET test setup for perovskite/perovskite tandem working photoelectrode and schematic of wired perovskite photoelectrode.

Figure 48 shows the LSV curve of a wired Pb/Sn-Pb-based perovskite/perovskite photoelectrode in a 0.5 M H_2SO_4 solution. The current density at 0 V vs. RHE is 14.6 mA/cm^2. The higher current density than the Pb-based perovskite/perovskite tandem device is due to the extended absorption range of the narrow-bandgap perovskites from 800 nm ($FA_{0.95}Cs_{0.05}PbI_3$) to 1000 nm ($MA_{0.3}FA_{0.7}Sn_{0.5}Pb_{0.5}I_3$). However, the onset voltage for HER is slightly lower than that of Pb-Pb tandem photoelectrodes. The lower fill factor is likely caused by the added resistance of the conductive Ag epoxy that bonded the back contact of the perovskite tandem cell to the stainless-steel metal foil.

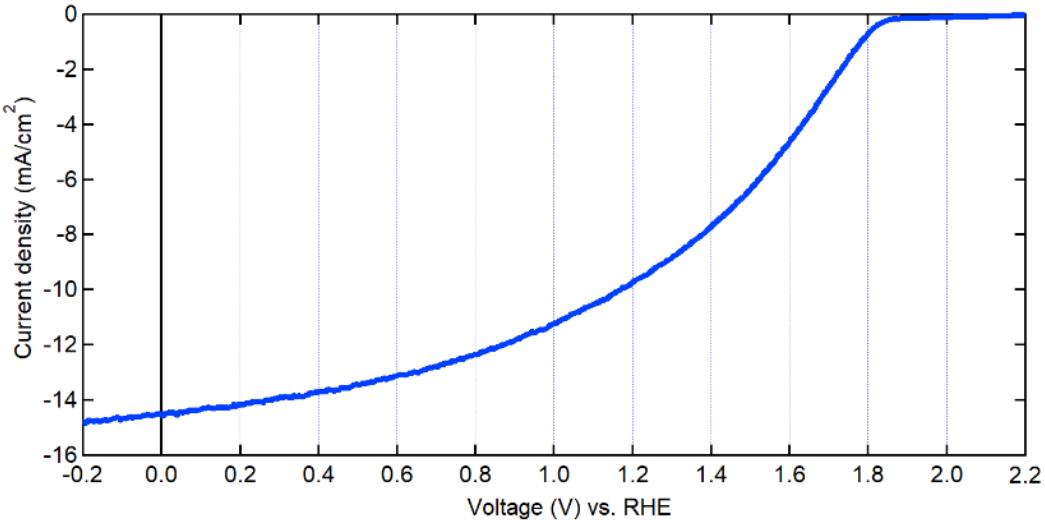

Figure 48. Linear sweep voltammetry curve of a wired Pb/Sn-Pb perovskite/perovskite photocathode in a three-electrode figuration under continuous illumination.

Figure 49 shows the LSV curve of a wired Pb/Pb-Sn-based perovskite/perovskite tandem photocathode cell under chopped AM1.5G illumination. The maximum photocurrent density at 0 V vs. counter electrode is ~12.5 mA/cm^2 under AM 1.5G one sun illumination in 0.5 M H_2SO_4. Assuming 100% Faradaic efficiency of 100%, the STH conversion efficiency for this perovskite tandem photoelectrode is as high as 15.4%. It should be noted that the wired perovskite tandem photoelectrodes are constructed using stainless steel and NiFeMo foils instead of commonly used precious catalyst materials (e.g., Pt, Ti, IrOx, RuO_x, etc.). This result demonstrates the great potential of using perovskite tandem photoelectrode for low-cost high-efficiency unassisted water splitting. We monitored the performance of unassisted water splitting by a wired Pb/Pb-Sn-based perovskite/perovskite photocathode at 0 V vs. counter electrode under chopped illumination (Figure 50). The photoelectrode shows almost constant photocurrent in one hour of operation under chopped light, showing promising operational stability. The long-term stability of wired perovskite/perovskite tandem photoelectrodes will be evaluated in the next quarter.

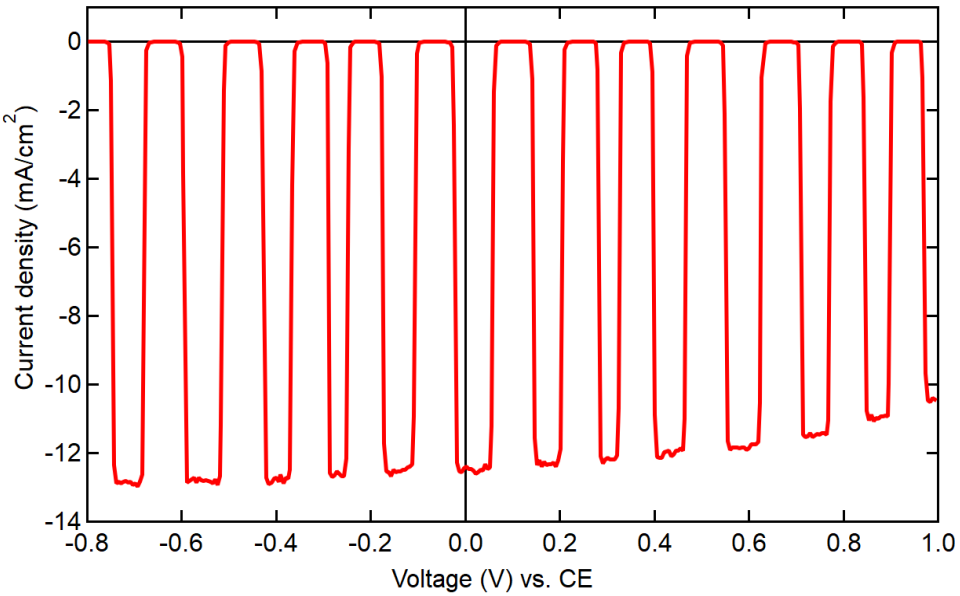

Figure 49. Linear sweep voltammetry curve of a wired Pb/Sn-Pb based perovskite/perovskite photocathode in a two-electrode figuration under chopped AM1.5G illumination.

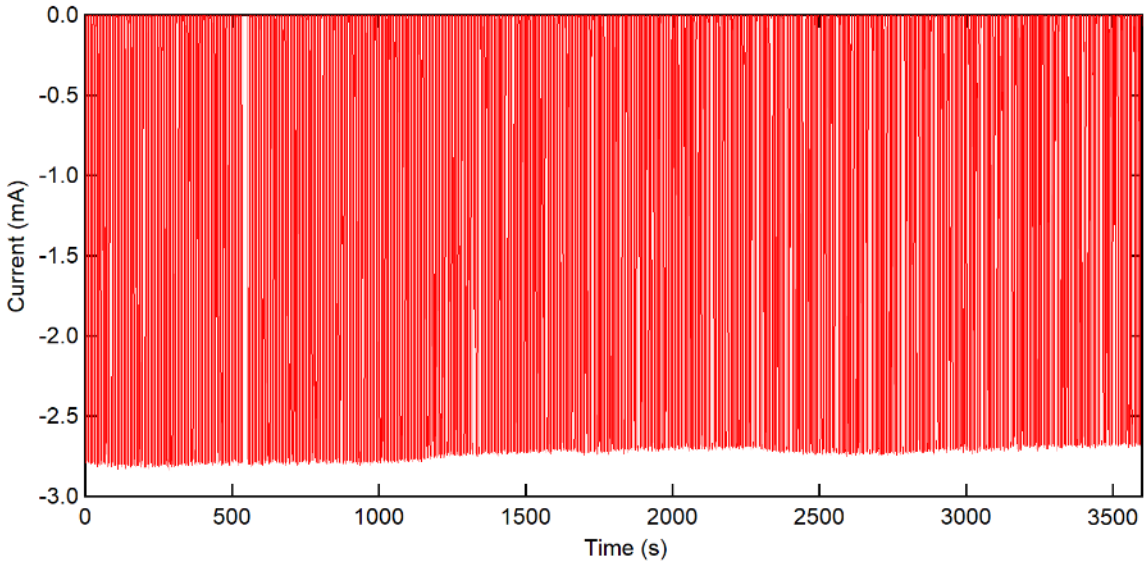

Figure 50. Chronoamperometry curve of unassisted water splitting of a wired perovskite/perovskite photoelectrode (active area = 0.16 cm^2) in two-electrode figuration at 0 V bias under chopped illumination.

10. Perovskite/perovskite tandem photoelectrodes for unassisted water splitting

In this activity, we continued our investigation on perovskite/perovskite tandem photoelectrodes. Figure 51a shows our current design for perovskite/perovskite tandem photoelectrodes. The tandem photoelectrode consists of a glass substrate, a transparent conducting oxide (TCO) front contact, a hole-transport layer (HTL), a wide-bandgap mixed halide (Br-I) perovskite photoabsorber, an electron-transport layer (ETL), an interconnecting (recombination) layer, an HTL, a narrow-bandgap mixed tin-lead perovskite photoabsorber, an ETL, a back contact, a conductive epoxy for photoelectrode integration, and a metal foil to protect the perovskite layers and interface with the electrolyte. Figure 51b shows a schematic band diagram of the perovskite/perovskite photocathode. The quasi-Fermi level difference between electrons ($E_{F,n}$) and holes ($E_{F,p}$) of the tandem photoelectrode under illumination adequately straddles the hydrogen-evolution and oxygen-evolution half-reactions (OER and HER). The sum of photovoltages generated by the 1.75-eV wide-bandgap and 1.25-eV narrow-bandgap perovskite layers is more than 2 V, sufficiently higher than the minimum thermodynamic voltage for splitting water (ΔE^0 = 1.23 V) plus the overpotentials required for OER and HER.

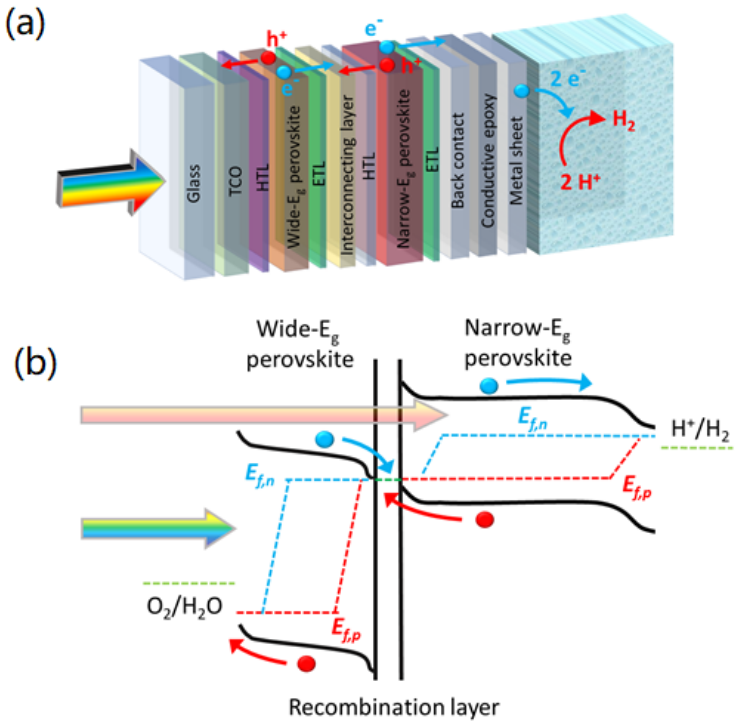

Figure 51. Schematics of (a) device architecture and (b) band diagram of a wired perovskite/perovskite tandem photocathode. The energy level and thickness of the layers are not at scale.

To evaluate the water-splitting performance of our perovskite/perovskite tandem photoelectrodes, we designed two sets of experiments. For the first configuration, we have a photovoltaic-driven electrochemical catalyst system (PV-EC) with a PV tandem cell connected to an electrolyzer with two separated electrodes through two external wirings. For the second configuration, a perovskite/perovskite tandem photoelectrode works as a photocathorde in the

electrolyte, and is wired to an anode. Figure 52a and b shows the front and back images of a perovskite/perovskite tandem cell for PV-EC applications. Figure 52 c and d shows the front and back images of a perovskite/perovskite tandem photocathodes in an electrolyzer. For both configurations, perovskite/perovskite tandem photoelectrodes were fabricated with a device structure of glass/ITO/PTAA/wide-E_g perovskite/C_{60}/SnO_2/ITO/PEDOT:PSS/narrow-E_g perovskite/C_{60}/BCP/Cu following our previously reported procedures. The wide-E_g perovskite absorber layer has a general composition of $FA_{0.8}Cs_{0.2}MA_{0.1}Pb(Br_{0.4}I_{0.6})_3$. The narrow-$E_g$ perovskite has a composition of $MA_{0.3}FA_{0.7}Pb_{0.5}Sn_{0.5}I_3$.or $FA_{0.8}Cs_{0.1}MA_{0.1}PbI_3$.

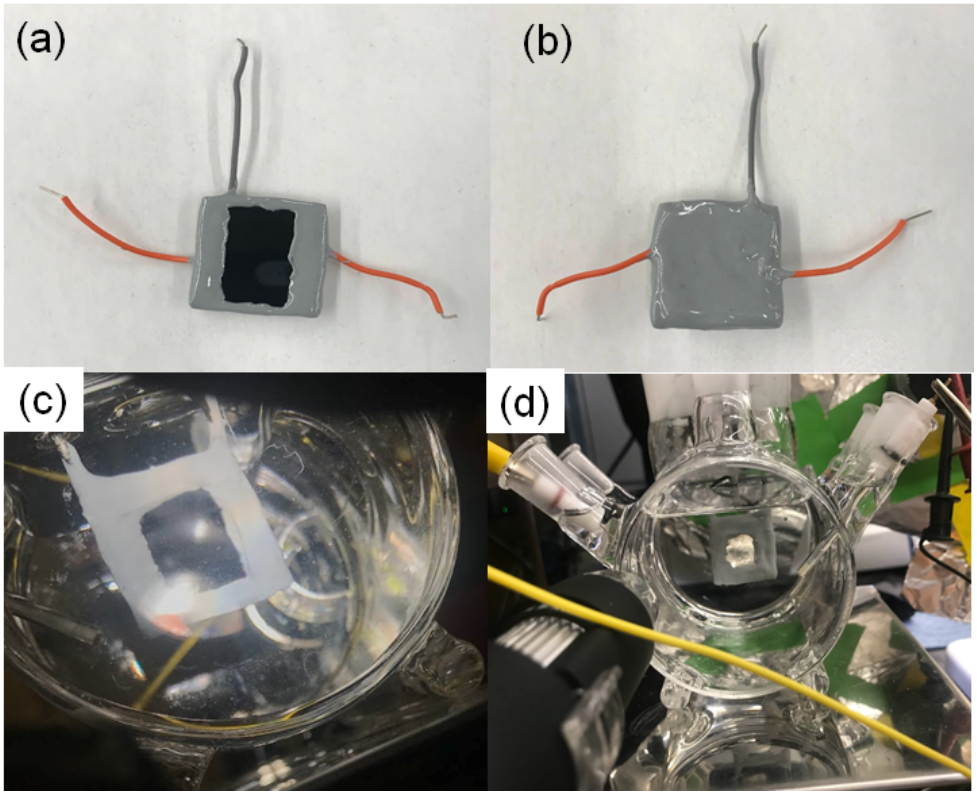

Figure 52. Photos of (a) the front and (v) back sides of perovskite/perovskite tandem cell wired for PV-EC applications. Photos of (c) the front and (d) back sides of a perovskite/perovskite tandem photocathode in an electrolyzer.

Figure 53a shows the current density-voltage (J-V) curves of a typical perovskite/perovskite tandem photoelectrode. The solar-to-electrical power conversion efficiency is 25.4 (24.7)%, with an open-circuit voltage (V_{OC}) of 2.08 (2.08) V, a short-circuit current density (J_{SC}) of 14.9 (14.9) mA/cm^2, and a fill-factor (FF) of 81.7 (79.8)%, determined by the reverse (forward) voltage sweep. Figure 53b shows the external quantum efficiencies of the top and bottom photoabsorbers. The integrated short-circuit current densities for the wide-bandgap and narrow-bandgap perovskites are 15.4 and 14.9 mA/cm^2, respectively, showing matched photocurrent in the tandem device.

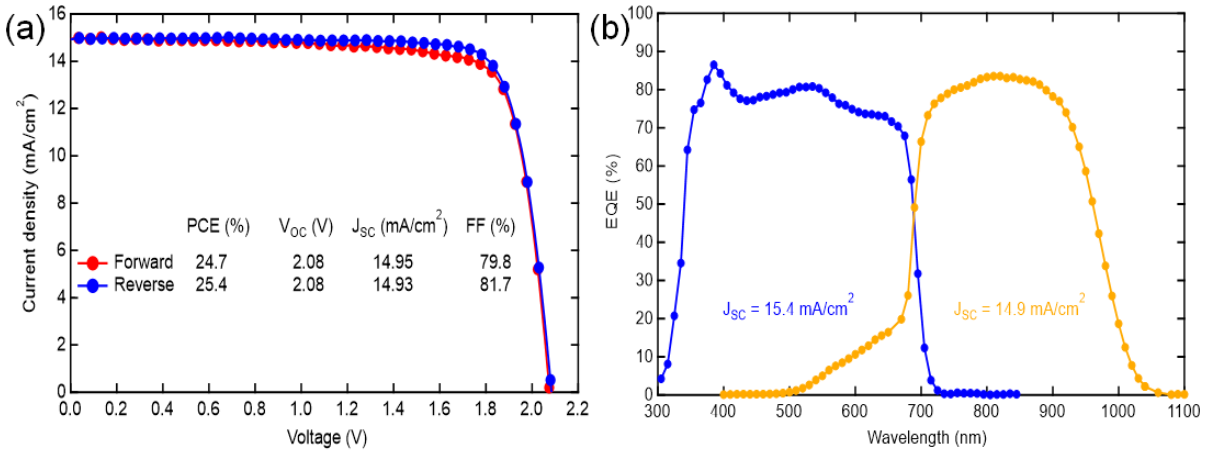

Figure 53. (a) J-V and (b) EQE curves of a typical perovskite/perovskite tandem photoelectrode.

To evaluate the water splitting potential of perovskite/perovskite tandem photoelectrodes, a perovskite/perovskite tandem device was connected to a potentiostat with a three-electrode configuration consisting of a Pt cathode for HER, an IrOx coated Ti anode for OER, and an Ag/AgCl reference electrode in a 0.5 M H_2SO_4 solution. Figure 54 shows the linear sweep voltammetry (LSV) curve of such a PV-EC system. The three-electrode PV-EC system shows a slightly lower onset voltage (V_{onset}) of 1.95 V than the V_{OC} of 2.08 V for the PV tandem cell. The 0.13 V difference is attributed to the HER overpotential of Pt in 0.5 M H_2SO_4. To further obtain the LSV behavior and STH efficiency of a two-electrode PV-EC system, we removed the reference electrode to construct a direct water splitting system. The LSV of a two-electrode PV-EC system is also displayed in Figure 54. Compared with the three-electrode system, the V_{onset} is further dropped by 1.07 V to ~0.88 V, due to the overpotential of OER at the IrO_x catalyst site. However, because of the high photovoltage and FF of the perovskite/perovskite tandem cell, the short-circuit current of the two-electrode PV-EC system retains a relatively high ratio of ~95%. As a result, the perovskite/perovskite tandem photoelectrode powered two-electrode PV-EC exhibits a high short-circuit current density of 13.7 mA/cm^2, corresponding to a maximum allowed STH efficiency of 16.85%. Such a high STH efficiency enables unassisted solar-driven water splitting, as hydrogen and oxygen gas bubbles were observed on the corresponding electrodes during the measurement.

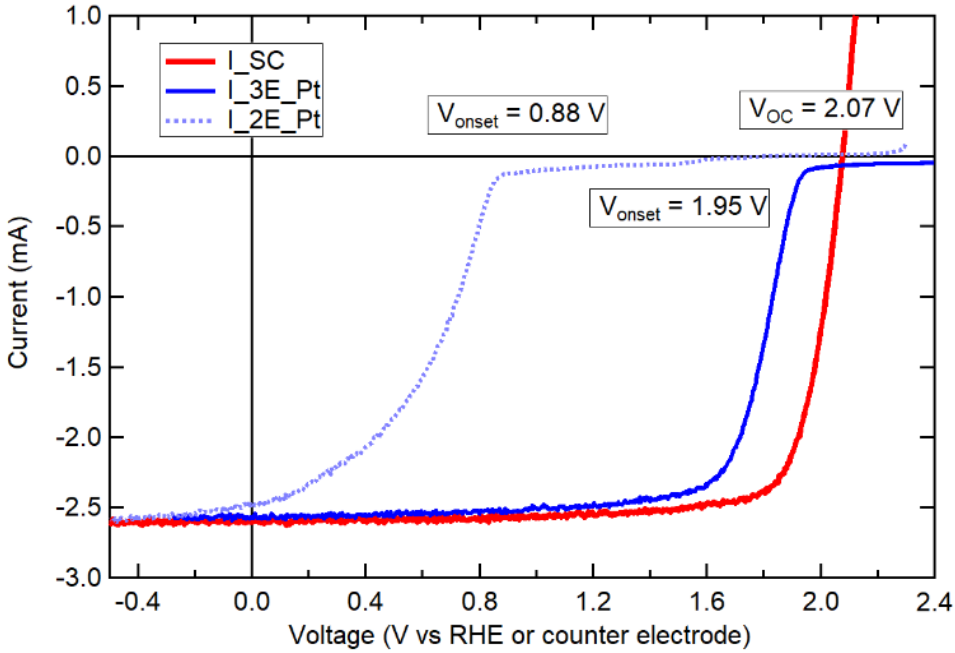

Figure 54. Linear sweep voltammetry curves of a Pb-based perovskite/perovskite photocathode in a three-electrode figuration under continuous and chopped illumination conditions. The active area of the tandem cell is 0.18 cm^2.

To construct low-cost integrated perovskite/perovskite tandem photocathodes, we need to have a proper metal sheet to protect the perovskite photoabsorber and minimize the HER overpotential at the electrode/electrolyte solid/liquid interface. We compared the overpotentials of a series of different cathode metal materials. Figure 55a shows the overpotential measurements of different metal electrodes. Figure 55b shows the photo of different metal electrodes. Among them, Pt shows the lowest HER overpotential. Stainless steel (SS), Mo, and Ni show relatively low HER overpotentials and are considered low-cost alternatives. Particularly, SS shows ~0.35 V higher overpotential than Pt. Perovskite/perovskite tandem photoelectrode can provide sufficient photovoltage to overcome this extra potential. To further evaluate the applications of different metal cathode foils in the integrated perovskite/perovskite tandem photocathodes, we measured the unassisted water splitting performance of a two-electrode PV-EC system with different working electrodes. Figure 56a plots the LSV curves of perovskite-tandem photoelectrode powered PV-EC systems based on different metal cathodes in two-electrode and three-electrode configurations. The performance difference at zero-bias (Figure 56b) represents the STH efficiency loss due to the HER overpotential different metal cathodes. The results show that Mo, Ni, and SS are suitable for constructing low-cost integrated perovskite/perovskite tandem photocathodes.

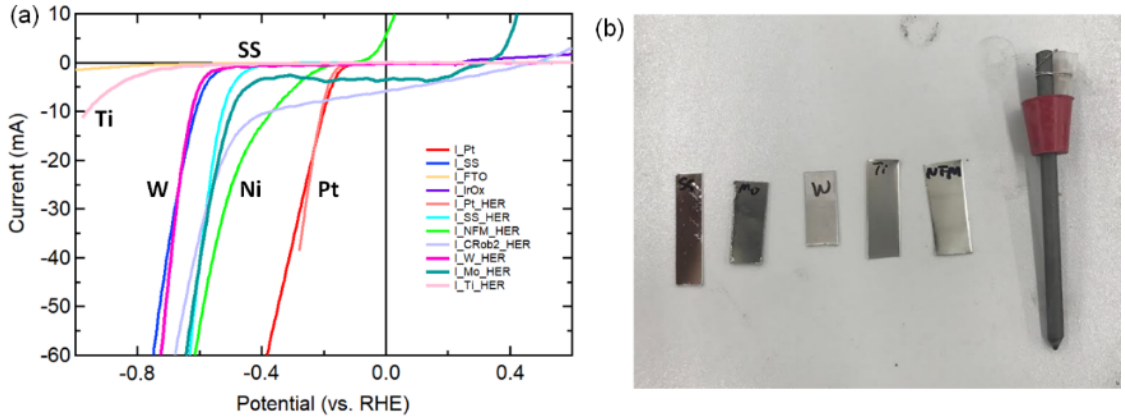

Figure 55. (a) LSV curves and (b) photo of different cathodes.

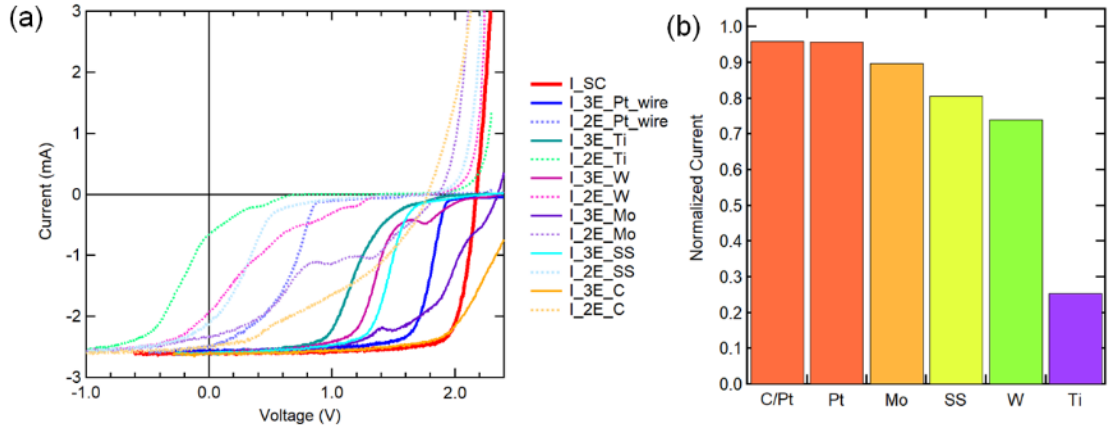

Figure 56. (a) LSV curves of two-electrode and three-electrode perovskite-tandem photoelectrode powered PV-EC system based on different metal cathodes. (b) The performance ratio of different cathode materials in two-electrode and three-electrode systems.

As a proof of concept, we used fabricated integrated perovskite/perovskite tandem photocathodes using an SS foil metal sheet coated with Pt nanoparticles (Sigma Aldrich). Figure 57 shows the PV, 3E-PEC, and 2E-PEC performance of an integrated perovskite/perovskite tandem photocathode. For 2E and 3E PEC measurements, IrO_X coated Ti and Ag/AgCl were used as the counter and reference electrodes. The electrolyte is 0.5 M H_2SO_4. The tandem photocathode exhibits excellent solar-driven water-splitting performance without external bias in an aqueous solution.

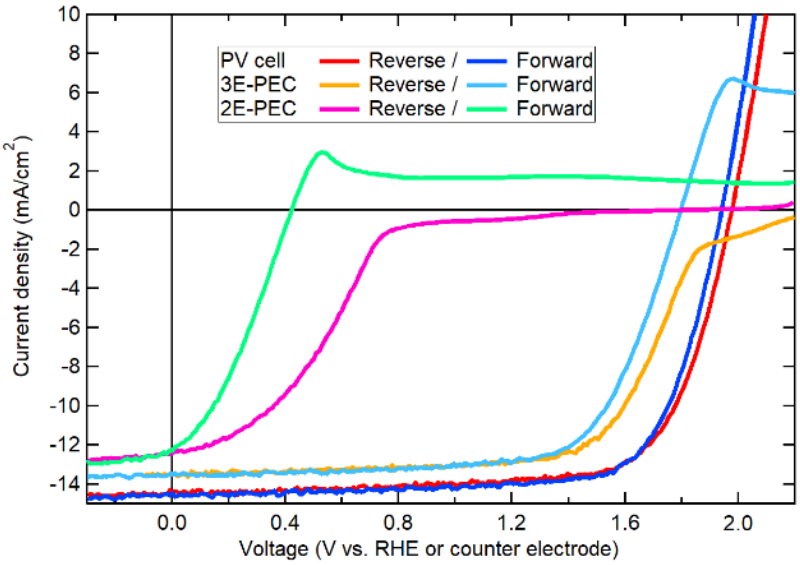

Figure 57. (a) LSV curves of an integrated perovskite-tandem photoelectrode for PV, and two-electrode and three-electrode PEC measurements.

Figure 58 shows the two-electrode LSV of an integrated perovskite/perovskite tandem photocathode under chopped AM1.5 G illumination. As discussed above, the tandem photoelectrode can perform unassisted water splitting with sufficient photovoltage to overcome the water redox potentials. The photocurrent density at zero bias vs. IrOx is determine to be 12.0 mA/cm^2 under AM1.5G one sun illumination in 0.5 M H_2SO_4, corresponding to an STH efficiency of 14.76%, assuming the Faraday efficiency is 1. The tandem photoelectrode shows a relatively stable operation in an aqueous solution. Figure 59 shows the chronoamperometry of a tandem photoelectrode at zero bias under chopped one-sun illumination. There is no photocurrent degradation after 5 hours of operation.

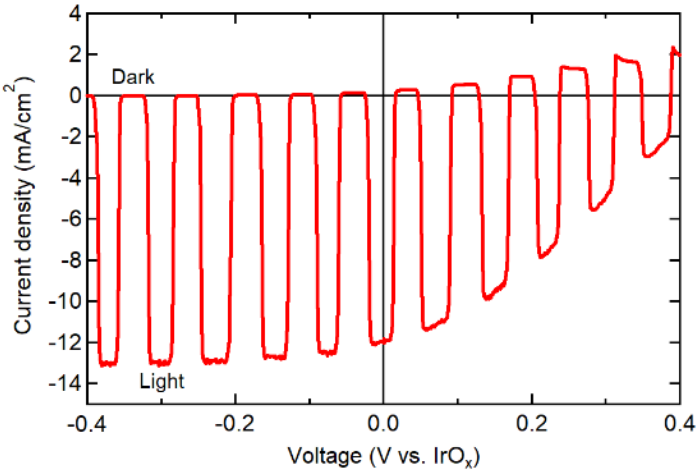

Figure 58. Two-electrode chopped J−V curve of a perovskite/perovskite tandem photoelectrode in 0.5M H_2SO_4 under chopped one-sun illumination. The photocathode sample area is 0.18 cm^2.

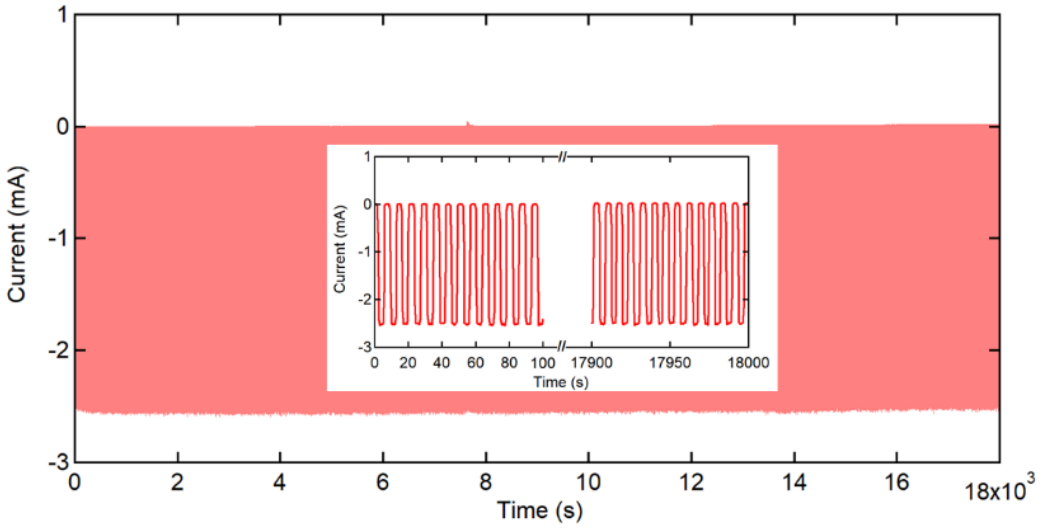

Figure 59. Chronoamperometry curve of unassisted water splitting of a perovskite/perovskite tandem photoelectrode (active area = 0.18 cm^2) in two-electrode figuration at 0 V bias under chopped illumination for ~ 5 hours. The inset shows the photocurrent in the first and last 100 s.

To accurately determine the STH efficiency of the perovskite/perovskite photoelectrode over time, we collected the hydrogen generation using a piece of laboratory Hoffman electrolysis apparatus for 24 hours. The cumulated charge generated by the tandem photoelectrode (active area = 0.18 cm^2) at zero bias is 49.9 mAh, and the collected hydrogen gas is 22.0 ml (Figure 60). The Faraday efficiency is calculated to be 98%. Therefore, the actual STH efficiency of our perovskite/perovskite tandem photoelectrode is determined to be 14.5%.

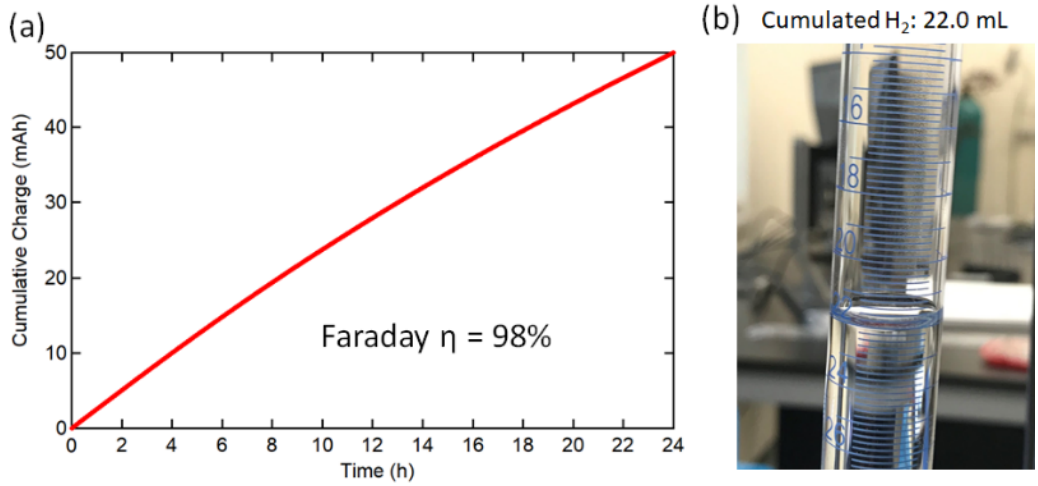

Figure 60. (a) Cumulative charge of a wired perovskite/perovskite tandem photocathode working at the 2-electrode mode under continuous illumination for 24 hours. Hydrogen generated by the tandem photoelectrode over 24 hours.

Figure 61 shows the long-term operational stability of a perovskite tandem photocathode under continuous 1-sun illumination at zero bias in an acidic aqueous electrolyte. The photocurrent of the photoelectrode decreased to ~46% of the initial value after 50 hours of operation. We suspect the slow water ingression through the epoxy encapsulation layer caused the degradation of perovskite photoabsorbers. An investigation is ongoing to understand the degradation and develop mitigation strategies.

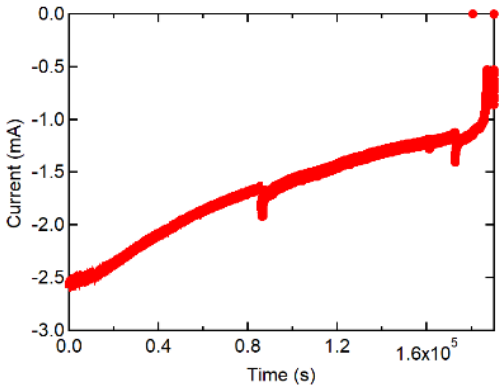

Figure 61. Stability measurement of perovskite/perovskite photocathode in an aqueous solution under continuous 1-sun illumination.

We also tested the photocurrent stability of Pb/Pb-based perovskite tandem photocathode in an acidic aqueous electrolyte. Figure 62 shows the evolution of the normalized STH efficiency of a wired Pb/Pb perovskite tandem photocathode with time. The STH efficiency of the tandem photocathode was measured without external bias under continuous AM 1.5G illumination using a 2-electrode configuration in 0.5 M H_2SO_4 solution. The 1.8/1.55 eV perovskite tandem photoelectrode exhibited an initial STH efficiency of 9.8% and retained 80% of its initial STH efficiency after 100 hours of continuous operation. The device experienced a catastrophic failure at ~ 105 h, likely caused by the damage of the epoxy in acid and water ingress induced degradation in the perovskite active layers.

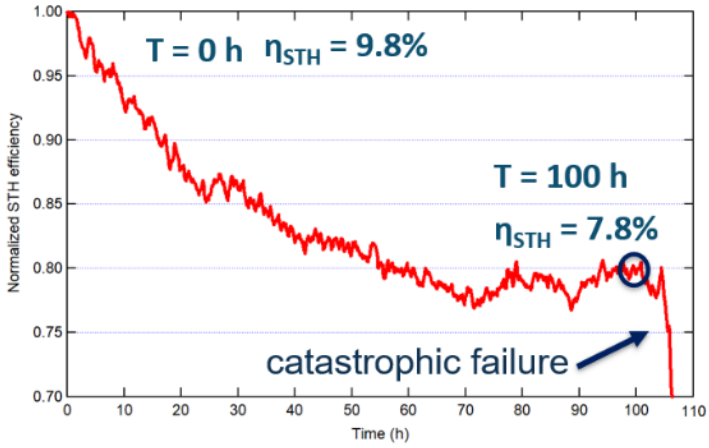

Figure 62. Stability measurement of perovskite/perovskite photocathode in an aqueous solution under continuous 1-sun illumination.

We continued our investigation toward demonstrating proof-of-concept perovskite/perovskite tandem photoelectrodes with an STH efficiency of > 10% in a wired two-electrode system and maintaining 80% of the initial efficiency for more than 100 hours. We assembled integrated perovskite/perovskite tandem photoelectrodes in the superstrate configuration, as shown in Figure 63(a). The perovskite/perovskite thin film tandem stacks were fabricated on TCO-coated glass substrates using the procedures previously developed in our lab. The device structure consists of a stack of glass/ITO/PTAA/wide-E_g perovskite/C_{60}/SnO_2/ITO/PEDOT:PSS/narrow-E_g perovskite/C_{60}/BCP/Ag following our previously reported procedures. The wide-E_g perovskite absorber layer has a composition of $CsPbI_2Br$ or $FA_{0.8}Cs_{0.2}MA_{0.1}Pb(Br_{0.4}I_{0.6})_3$. The narrow-$E_g$ perovskite has a composition of $MA_{0.3}FA_{0.7}Pb_{0.5}Sn_{0.5}I_3$.or $FA_{0.8}Cs_{0.1}MA_{0.1}PbI_3$. The completed tandem cells were integrated into a metal foil (e.g., Pt, stainless steel, NiFeMo) using conductive epoxy consisting of a mixture of Ag paste and C particle adhesive. The stainless steel metal foils were functionalized by Pt nanoparticles before the photoelectrode integration to enhance HER activities. The non-active areas were protected by non-conductive epoxy. The cathode terminal of the photoelectrode was wired to an IrOx/Ti counter electrode. Figure 63(b) shows a photo of the active stainless steel surface of a perovskite tandem photoelectrode in an aqueous electrolyte.

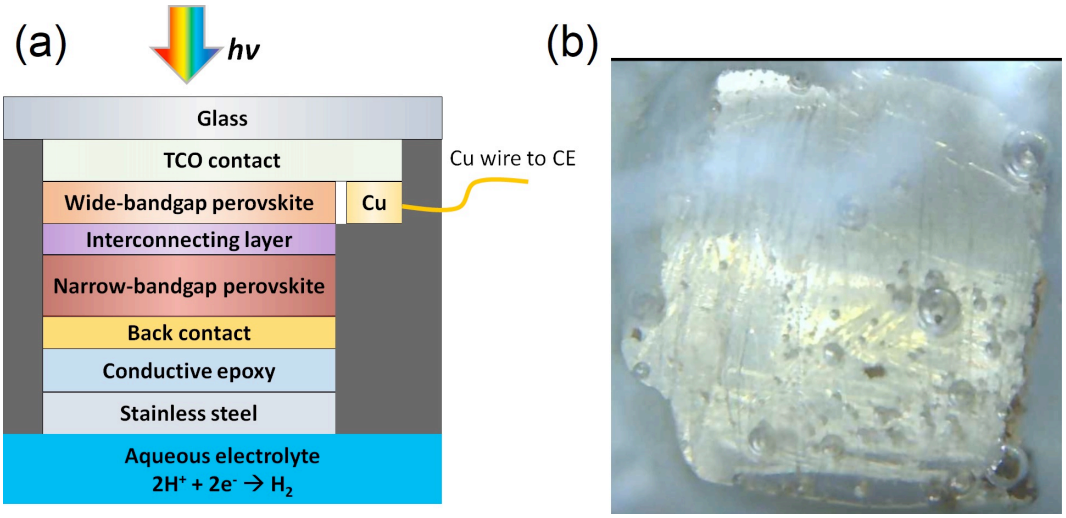

Figure 63. (a) Schematic of a perovskite tandem photoelectrode device architecture. (b) Photo of the stainless steel foil side of a perovskite tandem photoelectrode in an aqueous electrolyte.

To test the performance of perovskite/perovskite tandem photoelectrodes with different metal foils, we fabricated a series of perovskite/perovskite tandem devices using the combination of 1.9-eV $CsPbBrI_2$ and 1.25-eV $MA_{0.3}FA_{0.7}Pb_{0.5}Sn_{0.5}I_3$. The integrated tandem photoelectrodes were tested under the PV mode, 3-electrode (3E), and 2-electrode (2E) photoelectrochemical

(PEC) modes. Figure 64 plots the results of linear sweep voltammetry measurements of 4 different perovskite/perovskite photoelectrodes. The representative perovskite/perovskite tandem photoelectrode working in the PV mode shows a high open-circuit voltage (V_{OC}) of ~2.1 V and a high short-circuit current density (J_{SC}) of ~15 mA/cm^2. It is worth noting that the fill factor (FF) of this batch of tandem devices is relatively low (~45%), likely due to the processing damages caused during the mechanical integration of the tandem cell into metal foil using the conductive epoxy. The relatively high humidity in summer could also be a factor for the inferior performance. Our tandem photoelectrodes fabricated in winter shows much better FF and efficiency. Nonetheless, the high V_{OC} and J_{SC} of perovskite/perovskite tandem photoelectrodes can still enable efficient unassisted solar water splitting. The tandem photoelectrodes under a 3-electrode configuration show a slightly lower onset voltage (1.9 V, relative to RHE) than the PV cell due to the hydrogen evolution overpotential at the Pt metal foil interface. When measuring the photoelectrode in the 2-electrode mode, the onset potential is further reduced to ~1.2 V due to the oxygen evolution overpotential at the Ti/IrOx counter electrode. Due to the reduced onset potential, the zero-bias photocurrent density of the tandem photoelectrode is reduced to 10.8 mA/cm^2, corresponding to a solar-to-hydrogen (STH) efficiency of 13.3%. This result confirms that even with a relatively low FF in the integrated tandem device, the perovskite/perovskite tandem photoelectrode can still deliver an STH efficiency of more than 13%.

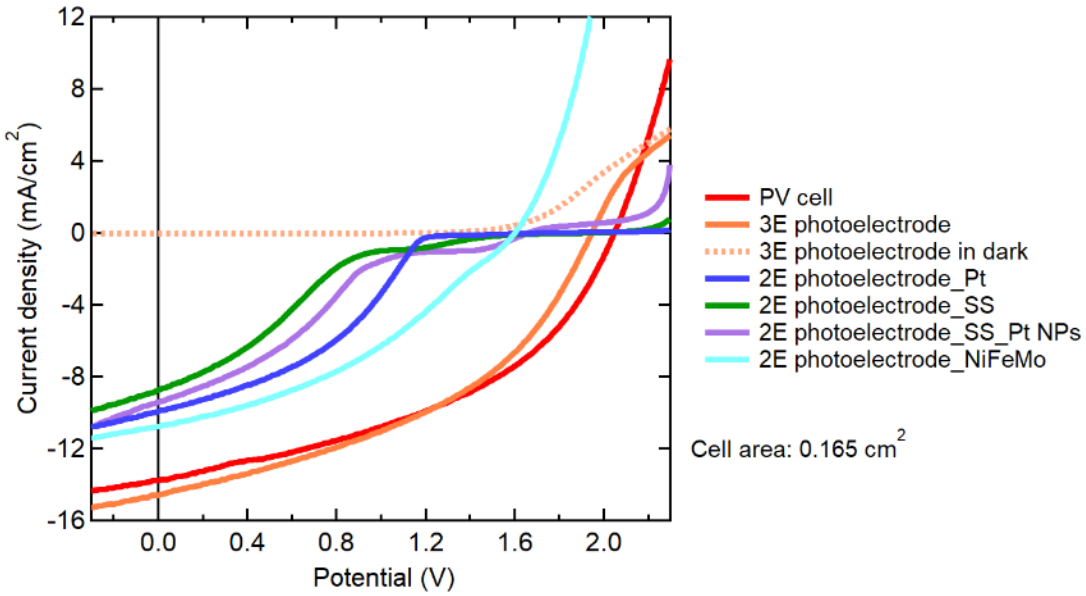

Figure 64. Linear sweep voltammetry curves of a batch of perovskite/perovskite tandem devices in different configurations, including a PV tandem cell, a stand tandem photoelectrode in a three-electrode configuration measured under illumination and in the dark, photoelectrodes integrated to Pt foil, stainless steel foil, stainless steel functionalized by Pt nanoparticles, and a NiFeMo foil.

We also tested alternative metal foils for perovskite/perovskite tandem photoelectrodes. We first tested low-cost 304 stainless steel (SS) foil to replace expensive Pt foil. Due to a higher HER overpotential, the tandem photoelectrode with the SS metal shows a ~0.45 V lower onset

potential and a lower J_{SC} of 8.8 mA/cm^2, corresponding to an STH efficiency of 10.8%. We then functionalized the surface of SS metal foils with a trace dose of Pt nanoparticles (Sigma Aldrich, 99.99%, 0.1% Pt colloid dispersion in H_2O). The catalyst functionalization increases the onset potential, enhancing J_{SC} and STH efficiency to 9.4 mA/cm2 and 11.6%, respectively. We further tested another low-cost alternative based on a nickel-based metal alloy foil (NiFeMo). The tandem photoelectrode based on this low-cost metal alloy foil shows a J_{SC} and STH efficiency of 10.8 mA/cm^2 and 13.3%, respectively. Figure 65 shows the STH measurement under chopped illumination, consistent with the LSV measurements under continuous illumination. We tracked the photocurrent density of a perovskite/perovskite tandem photoelectrode at zero bias under continuous AM1.5G illumination. The device retained 80% and 70% of its initial efficiency after continuously working for 70 and 100 hours (Figure 66), respectively, demonstrating decent device stability of the tandem photoelectrode. The mechanism of device degradation is still under investigation. These results show that low-cost metal foils can be used in integrated perovskite/perovskite tandem photoelectrodes for efficient unassisted solar hydrogen production.

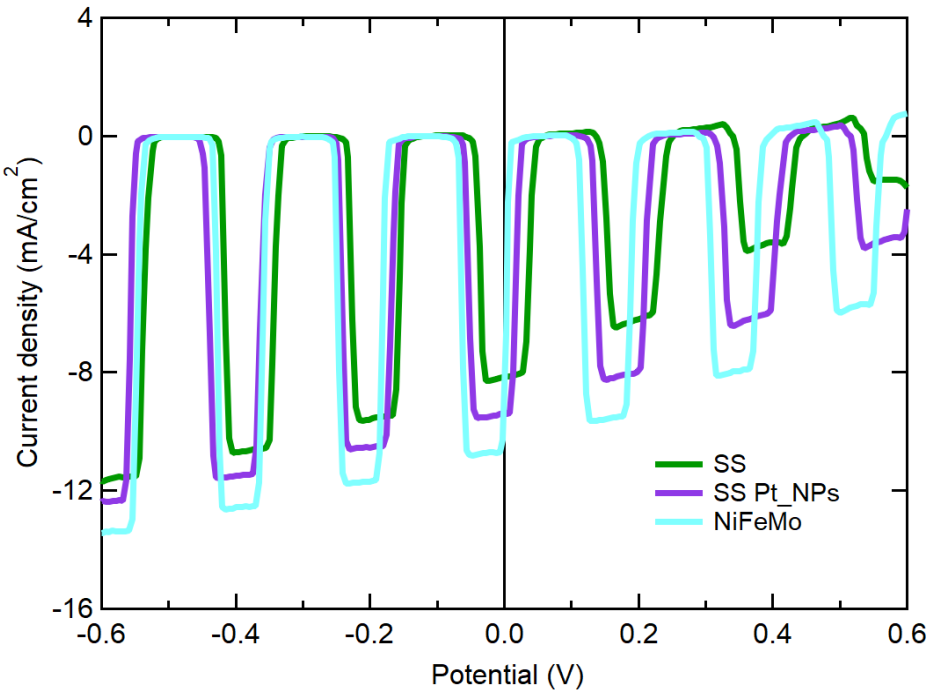

Figure 65. Linear sweep voltammetry curves of 2-E perovskite/perovskite tandem photoelectrodes integrated into different metal foils, including stainless steel, stainless steel loaded with Pt nanoparticles, and NiFeMo alloy.

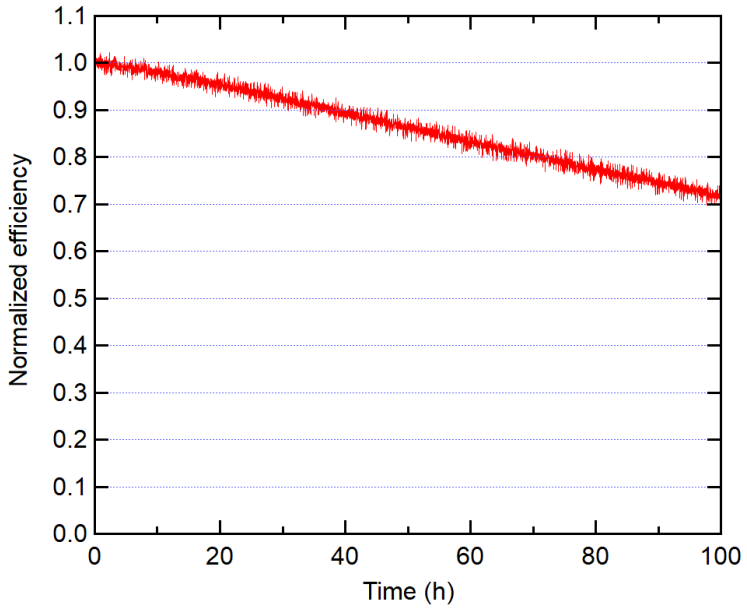

Figure 66. Normalized STH efficiency of a perovskite/perovskite tandem photoelectrode based on stainless steel foil and in an aqueous electrolyte.

We also compared the water-splitting performance of perovskite tandem photoelectrodes paired with low-cost carbon counter electrodes instead of Ti/IrOx. The perovskite/perovskite film stacks consisting of 1.8-eV $FA_{0.8}Cs_{0.2}Pb(Br_{0.4}I_{0.6})_3$ and 1.25-eV $MA_{0.3}FA_{0.7}Pb_{0.5}Sn_{0.5}I_3$ were completed earlier in a good fabrication batch in late March, and only Ag conductive epoxy was used for metal electrode integration. This batch of devices retains high FF and PCE after metal electrode integration. They represent the benchmark performance of our best PV tandem cells. Figure 67 compares the water splitting performance of several tandem photoelectrodes. It can be seen that replacing state-of-the-art Ti/IrOx counter electrodes with glassy carbon leads to a reduction of onset voltage of ~0.2 V, due to a higher overpotential of carbon for OER compared with IrO_x. J_{SC} dropped by ~5% after replacing Ti/IrO_x with glassy carbon, showing less efficient hole injection and high resistance at the carbon/electrolyte interface. However, because of the high open-circuit voltage (2.1 v) of the perovskite tandem devices, the tandem photoelectrodes still deliver high photocurrent density at zero bias in the two-electrode configuration. All three photoelectrodes, based on stainless steel, Pt foil, and Pt foil functionalized with Pt nanoparticles show high photocurrent densities of higher than 13.5 mA/cm^2 at zero external bias, corresponding to an STH efficiency of 16.6%.

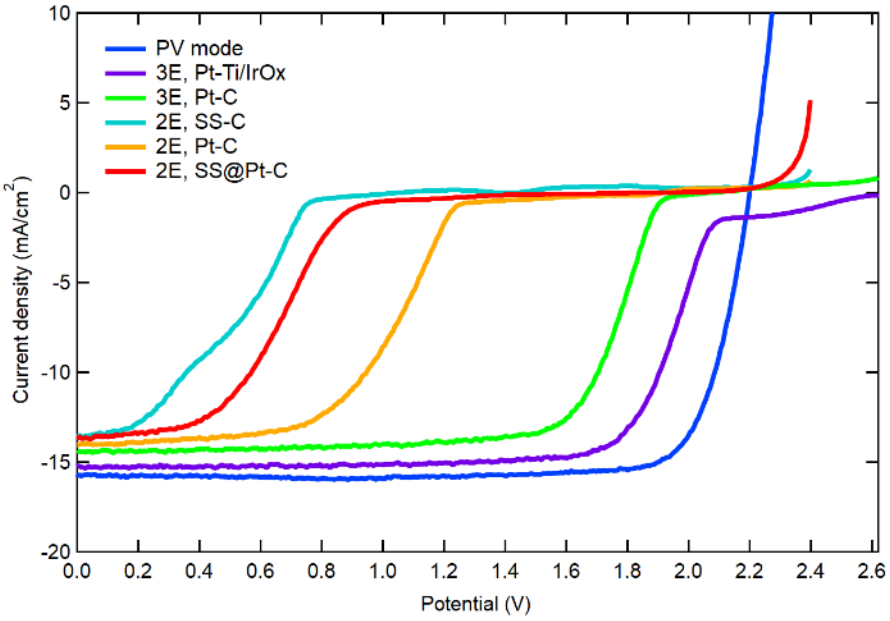

Figure 67. Linear sweep voltammetry curves of a batch of perovskite/perovskite tandem devices in different configurations, including a PV tandem cell, a stand tandem photoelectrode in a three-electrode (Pt-Ti/IrO_x-Ag/AgCl)configuration, a tandem photoelectrode in a three-electrode (Pt-C-Ag/AgCl)configuration, a stainless steel-based tandem photoelectrode, a Pt-based tandem photoelectrode, a Pt nanoparticle functionalized stainless steel-based tandem photoelectrode. Carbon was used as the counter electrode for all two-electrode measurements.

We further tested the stability of three almost-identical perovskite/perovskite tandem photoelectrodes based on stainless steel foils and wired to a glassy carbon counter electrode in a two-electrode configuration in an acidic aqueous electrolyte. Figure 68 shows the normalized photocurrent as a function of operation time under continuous AM 1.5G solar illumination. The T_{80} lifetimes (efficiency drops to 80% of its initial value) of these three devices are 13, 33, and 70 hours. These three devices show quite different operational lifetimes, which are significantly lower than the lifetimes of a tandem PV device fabricated in the same batch, which has a T_{80} lifetime of more than 110 hours. The two quick failure devices (Photoelectrode 1 & 2) clearly show the degradation of perovskite materials (see Figure 69). The white color is likely due to the formation of decomposition products of perovskite, such as lead halides and hydroxides. The most stable device shows no obvious perovskite material degradation from visual inspection. Because all three almost-identical photoelectrodes were operated in the same environment, it is likely that the non-conductive epoxy package and the water permeability of the metal/conducive adhesive interface play a key role in protecting the perovskite absorber materials from water-induced degradation.

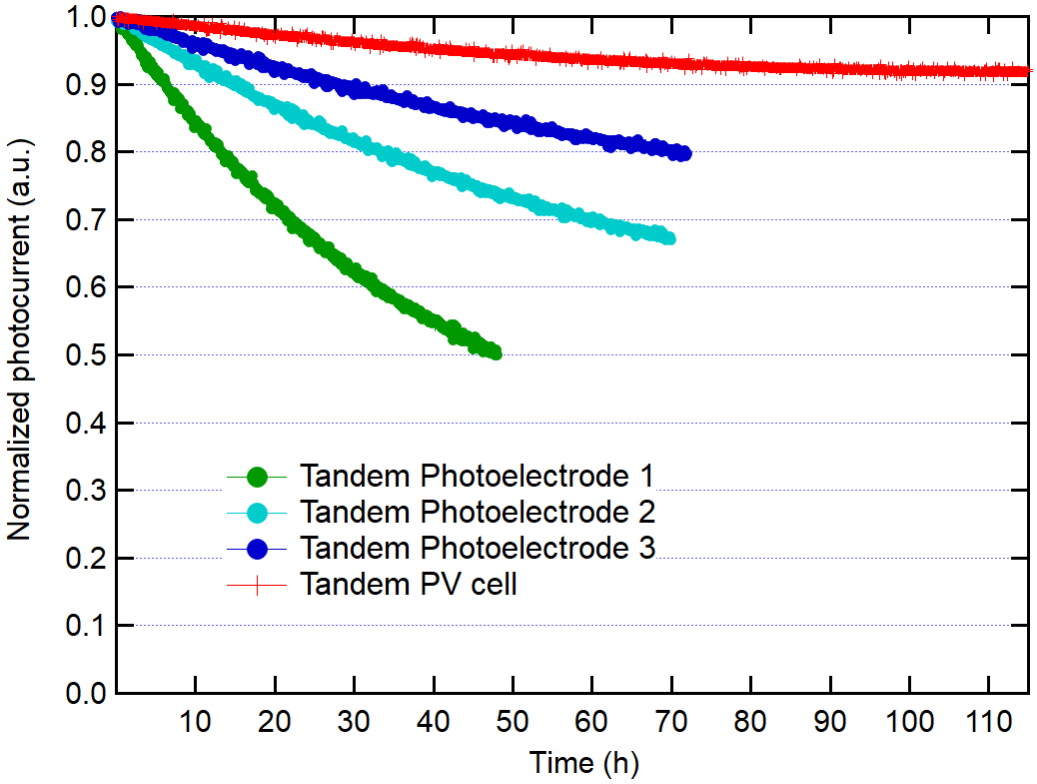

Figure 68. Normalized photocurrent of 3 perovskite/perovskite tandem photoelectrodes based on stainless steel foil and wired to a glassy carbon counter electrode in an aqueous electrolyte.

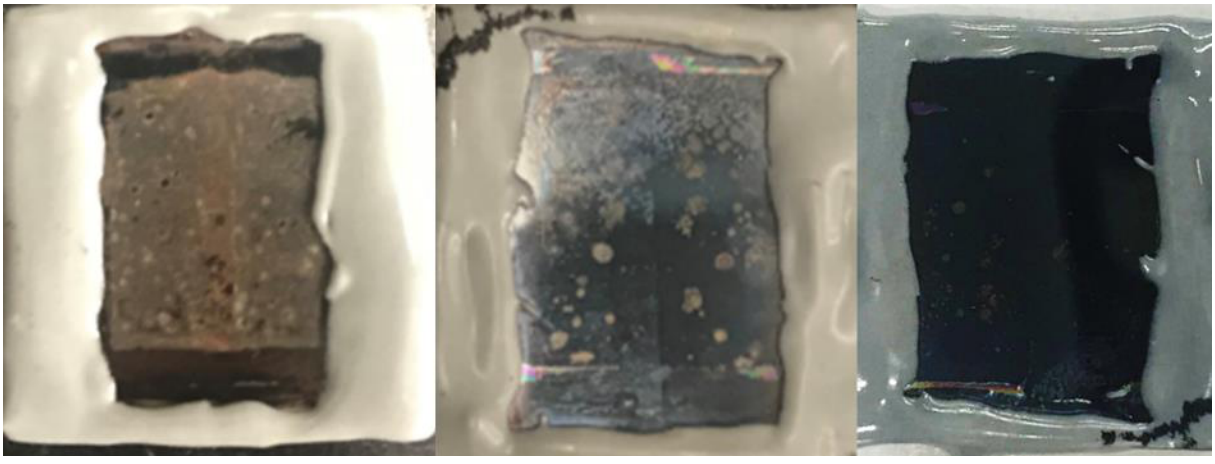

Figure 69. Photos of perovskite/perovskite photoelectrodes after 72 hours of continuous operation in an acidic aqueous electrolyte. From Left to right, photoelectrode 1, 2, and 3.

We sent two perovskite/perovskite tandem photoelectrodes to NREL Hydrogen nodes for standardized solar hydrogen production measurements. Figure 70 shows the PEC measurement results of our Pb-Sn based perovskite photoelectrodes in a 0.5 M sulfuric acid electrolyte with an IrOx OER anode. The ABET Solar Simulator light source was calibrated with 1.8 eV GaInP reference cell. The PEC device was totally submerged in water. Our tandem photoelectrode show unassisted water splitting at zero bias. The JSC is ~7 mA/cm^2, corresponding to ~8.6% STH conversion efficiency. It is worth noting that this photoelectrode has a stainless-steel metal foil back electrode without catalysts. The results confirm that our perovskite/perovskite tandem photoelectrodes can be used for low-cost solar hydrogen production even without using any expensive Pt catalysts.

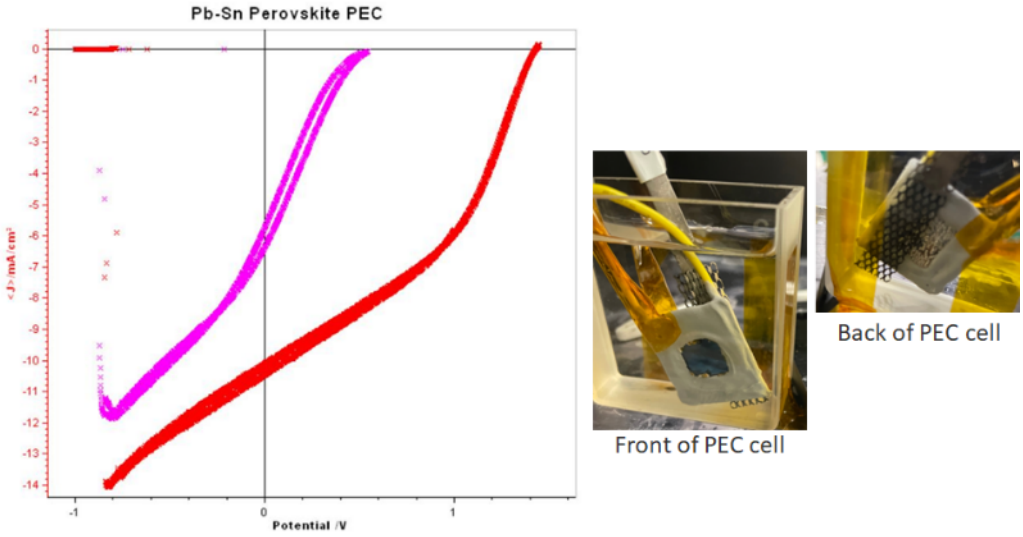

Figure 70. PEC measurement results and photos of our PEC tandem cell.

We also measured PEC durability at NREL HydroGEN node. The PEC tandem device was measured at short circuit submerged operation. The device showed nearly 3 hours of spontaneous STH conversion in PEC configuration (Figure 71). Unfortunately, the failure of epoxy packaging led to rapid device degradation. Images in Figure 71 show that epoxy discoloration is evident in the post durability device. Epoxy swelling was also observed with total perovskite dissolution and only metal foil intact. The stability measurement confirms the importance of using an orifice interface electrolyzer design to separate PEC photoelectrode from the aqueous acidic electrolyte but keeps only the metal foil interface with water. Device stability evaluation will continue in the next quarter.

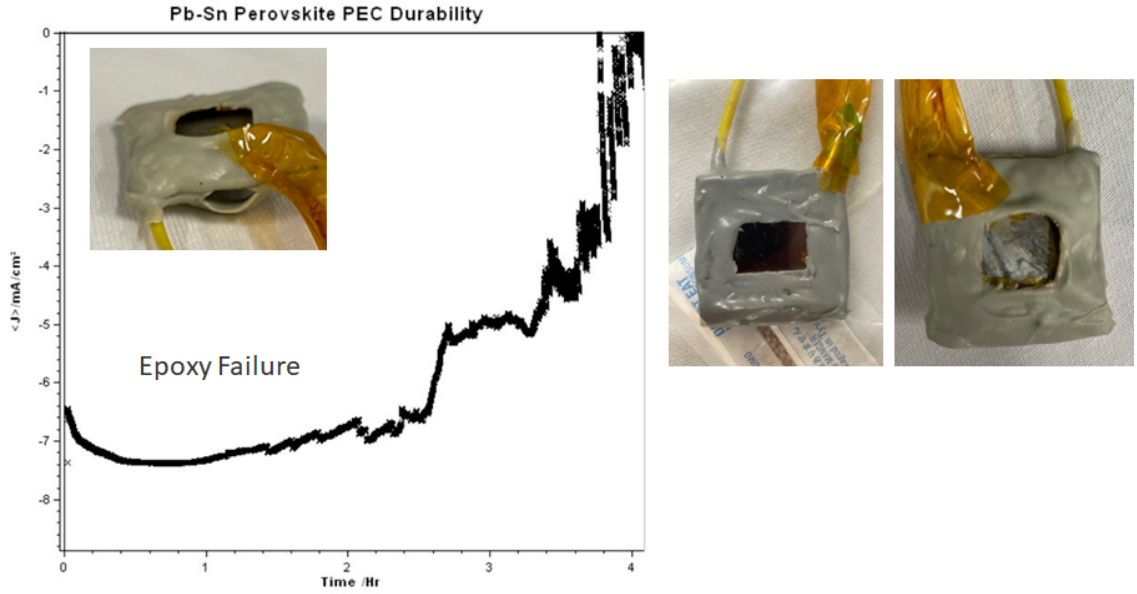

Figure 71. Degradation of perovskite photoelectrode due to epoxy failure.

We also fabricated several Pb/Pb perovskite/perovskite tandem photoelectrodes for stability measurements. We tested the operation of the tandem photoelectrode in an acidic aqueous electrolyte (0.5 M H_2SO_4) using a two-electrode configuration with a wired Ti/IrO_x anode electrode. The perovskite/perovskite tandem photoelectrode can generate hydrogen under illumination at zero bias voltage at an STH efficiency of ~12%. We monitored the operational stability of a tandem photoelectrode in an acidic aqueous electrolyte under continuous 1-sun illumination at zero bias (Figure 72). The tandem photoelectrode delivered an initial STH efficiency of 12.5%. It retained ~85% of its initial efficiency after 100 hours of operation, showing the promising stability of these perovskite tandem photoelectrodes.

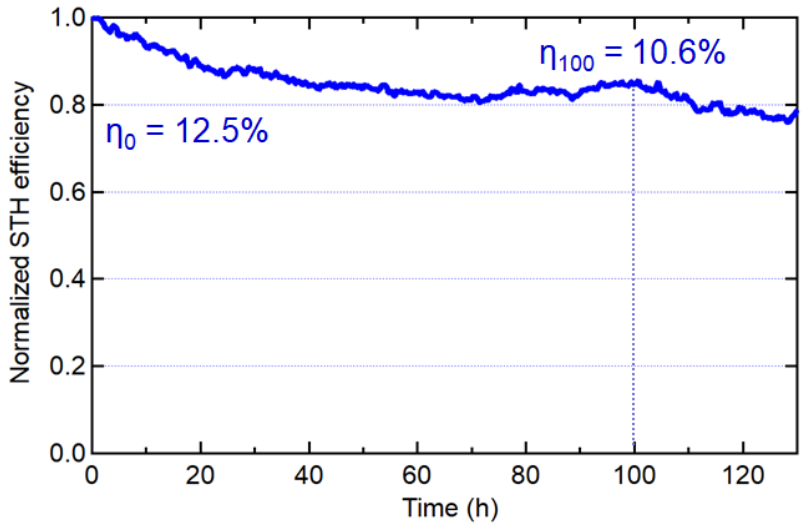

Figure 72. Stability measurement of a Pb/Pb perovskite tandem photoelectrode in an acidic aqueous electrolyte under continuous 1-sun illumination at zero bias.

11. Optimizing perovskite/perovskite tandem devices

In this activity, we fabricated 2-terminal perovskite/perovskite tandem solar cells by combining 1.25-eV low-E_g $FA_{0.7}MA_{0.3}Pb_{0.5}Sn_{0.5}I_3$ bottom subcells with 1.79-eV wide-Eg $FA_{0.8}Cs_{0.2}Pb(I_{0.6}Br_{0.4})_3$ top subcells. Figure 73a presents the structure of a tandem cell, which has a configuration of Glass/ITO/[2-(9H-Carbazol-9-yl)ethyl]phosphonic acid (2PACz)/Wide-E_g perovskite/C_{60}/ALD-SnO_2/Au/PEDOT: PSS/Low-E_g perovskite/C_{60}/BCP/Ag. Figure 73b shows the J-V curves of champion tandem cells. For the target device, we introduced potassium citrate to stabilize the perovskite and PEDOT:PSS interface. The target device with the optimal HTL treatment achieved the highest PCE of 26.08% (25.65%), with a V_{OC} of 2.09 V (2.08 V), a J_{SC} of 15.50 mA cm-2 (15.51 mA cm^{-2}), and a FF of 80.5% (79.5%) under reverse (forward) scans, whereas the control device only exhibited a champion PCE of 24.68% (23.90%), with a V_{OC} of 2.04 V (2.03 V), a J_{SC} of 15.20 mA cm^{-2} (15.27 mA cm^{-2}), and a FF of 79.6% (77.1%). The EQE spectra of the two subcells in both control and target devices are presented in Figure 73c. The EQE spectra of wide-E_g subcells did not notably change in the two tandem devices. However, the EQE of the low-E_g subcell in the target device (15.45 mA cm^{-2}) was slightly higher than that of the low-E_g subcell in the control device (15.14 mA cm-2), consistent with the results shown in the low-E_g single-junction solar cells. Figure 73d shows that the steady-state efficiency outputs of the best-performing control and target tandem devices are 24.45% and 25.98%, respectively, which agrees with the J-V results.

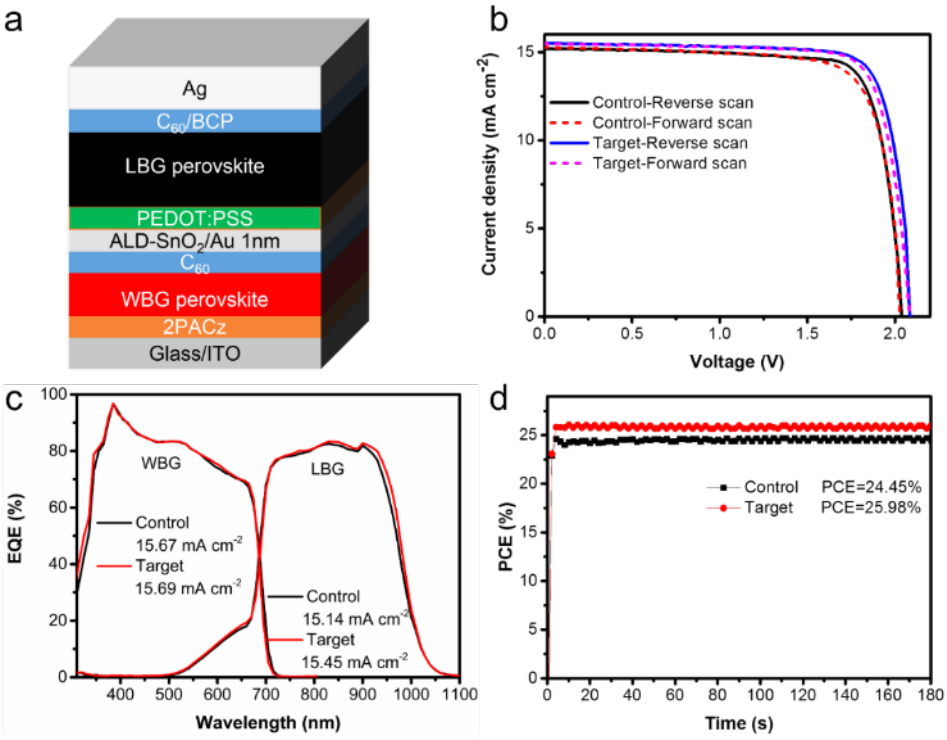

Figure 73. (a) Schematic structure of a 2-Terminal all-perovskite tandem device. (b) J-V curves of the champion control and target tandem devices. (c) EQE spectra of top subcell and bottom subcell in control and target tandem devices. (d) Steady-state efficiency outputs of the champion control and target tandem devices.

In addition, the target devices were reproducible with an average PCE of ~25.4% and a narrower distribution, while the control devices yielded an average PCE of ~23.6% and a wider distribution (Figure 74a). We further investigated the light stability of tandem devices. Figure 74b shows the MPP tracking of tandem cells under one-sun illumination in ambient air. The target device exhibited enhanced light stability, retaining 90% and 80% of its initial PCE for ~300 and ~700 h, respectively, significantly outperforming the control device.

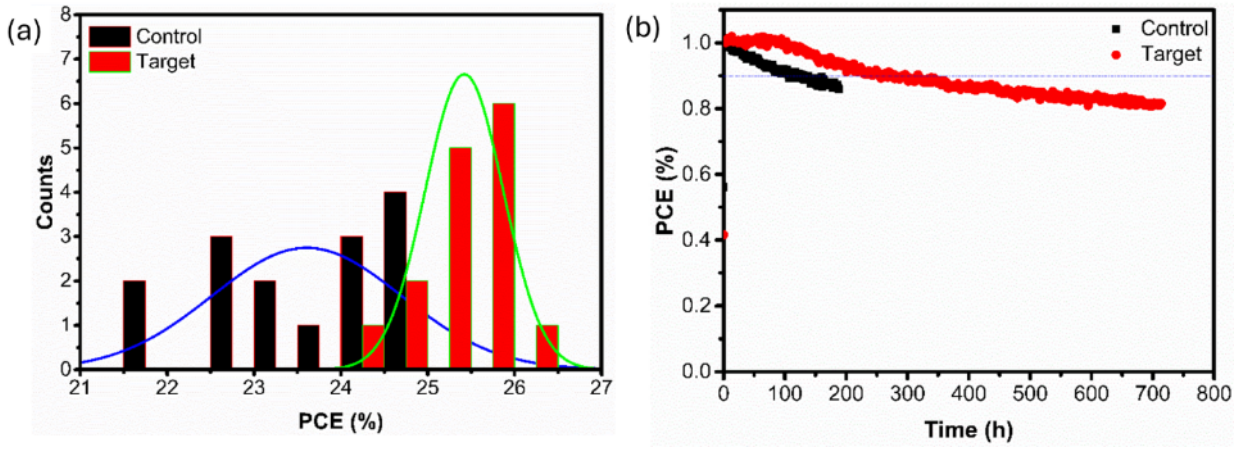

Figure 74. (a) PCE histograms of control and target tandem devices (15 devices in count). (b) MPP tracking of control and target tandem devices.

12. Optimizing perovskite/perovskite tandem photoelectrodes

To evaluate the theoretical STH efficiency limit of our perovskite/perovskite tandem photoelectrodes, we conducted a detailed balance calculation of general dual-junction tandem photoelectrodes as a function of the bandgaps of top and bottom light absorbers. State-of-the-art catalysts were taken into consideration to minimize the OER and HER overpotential losses to ~0.3 V.

Detailed balance efficiency calculation of double-junction tandem absorbers was performed following the work of Shockley and Queisser. In brief, for an ideal semiconductor absorber, the total rate of recombination at the short circuit condition is only determined by the blackbody radiation from both sides of the absorber layer with photon energy above its bandgap. The dark saturated current density (J0) can be calculated using this equation:

$$J_0 = 2q \int_{E_g}^{\infty} \frac{1}{\exp(h\nu/kT)-1} \frac{2\pi\nu^2}{c^2} d\nu,$$

where q is the unit charge, E_g is the bandgap of the solar cell, h is the Planck constant, k is the Boltzmann constant, T is the temperature of the cell, v is the photon frequency, and c is the speed of light.

The short-circuit photocurrent density (J_{SC}) of a top semiconductor absorber is calculated by

$$J_{SC,top} = \int_{\lambda_i}^{1240/E_{g,top}} [I_0(\lambda)]\, d\lambda,$$

where $I_0(\lambda)$ is the AM1.5G solar spectrum, λi is the shortest wavelength for the illumination spectra, and $E_{g,top}$ is the bandgap of the top subcell with a unit of eV.

The short-circuit photocurrent density (J_{SC}) of a bottom semiconductor absorber is calculated by

$$J_{SC,bot} = \int_{1240/E_{g,top}}^{1240/E_{g,bot}} [I_0(\lambda)]\, d\lambda,$$

where $E_{g,bot}$ is the bandgap of the bottom subcell with a unit of eV.

The J-V curve of an ideal subcell can be calculated by the Shockley diode equation:

$$J = J_0 \left[\exp\left(\frac{V}{kT}\right) - 1\right] - J_{SC}.$$

The J-V curves of individual subcells were numerically solved in a bandgap range of 1 to 2 eV for the bottom cell and 1-3 eV for the top cell with a step size of 0.05 eV. The J-V curves of a tandem solar cells were obtained by numerically solving the equations:

$$J_{tandem} = J_{top} = J_{bot}$$

$$V_{tandem} = V_{top} + V_{bot}.$$

For the J-V curves of an ideal water electrolyzer, we assumed 0.05 and 0.25 eV overpotentials for HER and OER reactions and simulated an ideal diode behavior.

$$J_{electrolyzer} = J_{0,electrolyzer} \left[\exp\left(\frac{V}{2kT}\right) - 1\right].$$

The saturated current density (J_0,electrolyzer) was set to 10^{-13} mA/cm^2 to obtain an electrolyzer on-site voltage of ~1.55 eV. After that, we numerically solve the PV electrolytic operational photocurrent density (J_{op}) and voltage (V_{op}) by finding the intercept:

$$J_{op} = J_{tandem}(V_{op}) = J_{electrolyzer}(V_{op})$$

The STH efficiency of the tandem photoelectrode was then calculated by:

$$\eta_{STH} = \frac{J_{op} \times 1.23\ (V)}{100\ mW/cm^2} \times 100\%.$$

Figure 75a plots the STH efficiency map of tandem photoelectrodes with different bandgap combinations. Unlike photoelectrodes based on a single semiconductor material, the dual-junction tandem device utilizing two perovskite absorbers with complementary light absorption can harness the visible and near-infrared range of the solar spectrum more efficiently, significantly improving the operating photocurrent for the water-splitting reaction. As a result, APTPEs have the potential to achieve >22% STH efficiency by pairing two perovskite absorbers, significantly outperforming the theoretical STH efficiency limit of 15% for PEC photoelectrodes based on a single light absorber (Figure 75b), promising for cost-effective solar hydrogen fuel production.

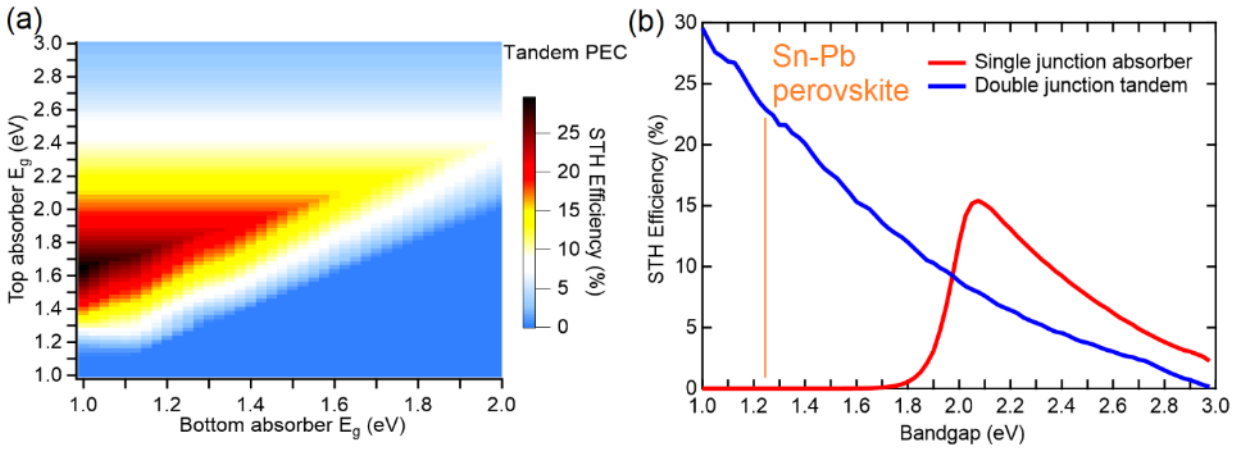

Figure 75. (a) Calculated detailed balanced STH efficiency limits of an ideal double-junction tandem photocathode. (b) Detailed balanced calculation of STH efficiency limits of single-junction and double-junction photoelectrodes as a function of the bandgap of a single absorber or the bottom absorber of a tandem photoelectrode. The line indicates the minimum bandgaps of Sn-Pb perovskites.

We fabricated integrated perovskite/perovskite tandem photoelectrodes and measured their performance. We first fabricated two-electrode perovskite/perovskite tandem photoelectrodes by integrating a monolithic perovskite tandem thin-film stack to a thin metal foil using a mixed graphite/Ag paste and wired the TCO contact to an external IrOx anode. We found the mixed graphite/Ag paste is critical for the metal foil integration into the all-perovskite tandem film stack. The isopropanol-based graphite paste is perovskite-compatible but has relatively high electrical resistivity (sheet resistance of 1800 Ω/sq). Mixing graphite and Ag pastes can significantly decrease the sheet resistance of the paste to 0.06 Ω/sq (Figure 76a) without deteriorating the underneath perovskite layers (Figure 76b).

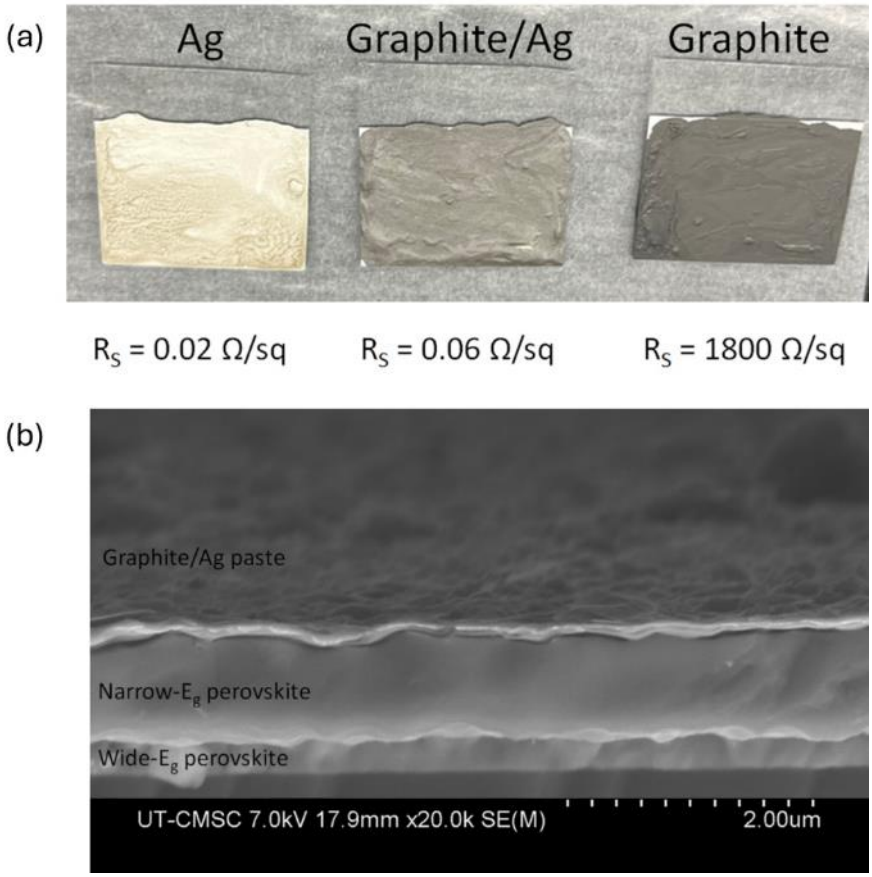

Figure 76. (a) Photos of Ag, graphite, and mixed graphite/Ag pastes coated on soda-lime glass substrates. The sheet resistance values were measured by four-point probe measurements. (b) Cross-sectional SEM image of mixed graphite/Ag paste coated on top of an all-perovskite tandem solar cell. The underneath perovskite layers are intact after coating the conductive paste.

We found that the conductive paste significantly influences the LSV characteristics of APTPEs (Figure 77). The PEC water-splitting performance was evaluated using two-electrode (2-E) and three-electrode (3-E) configurations in an aqueous 0.5 M H_2SO_4 electrolyte under simulated AM 1.5G one-sun illumination. The device based on a graphite conductive paste with a higher sheet resistance shows lower FF and lower operating photocurrent density than the one based on mixed graphite/Ag paste, whereas the device with Ag paste shows poor junction quality and low J_{SC}.

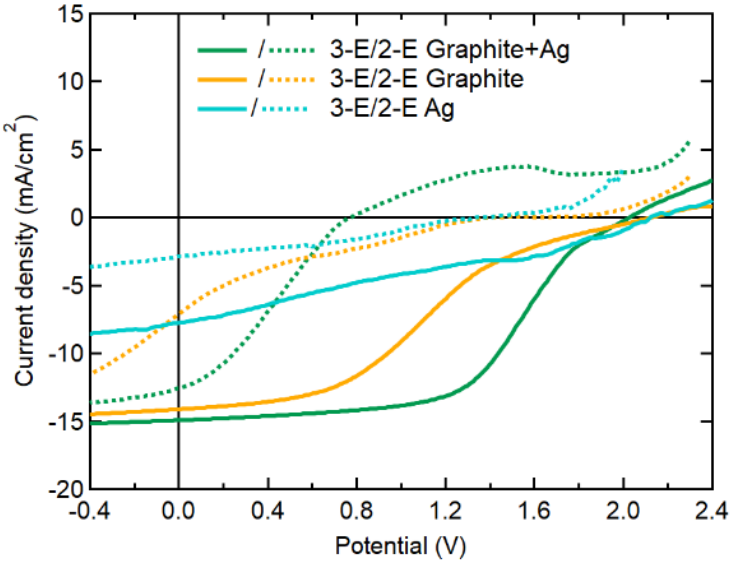

Figure 77. LSV curves of all-perovskite-tandem photoelectrode integrated with graphite, Ag, and graphite/Ag pastes in 2-E and 3-E configuration under simulated AM1.5G illumination.

After optimizing the tandem photoelectrode integration process, we obtained devices with improved V_{OC} and FF. Figure 78a displays the linear sweep voltammetry (LSV) curve of the best perovskite/perovskite tandem photoelectrode in 2-E and 3-E configurations under one-sun illumination. Figure 78b shows the 2-E LSV of the same tandem photoelectrode. This photoelectrode exhibited an operating photocurrent density of ~15 mA cm^{-2} at zero bias vs. IrO_x, corresponding to an STH efficiency of 18.5%. The high zero-bias operating photocurrent density of 15 mA/cm^2 is benefits from the high V_{OC} of ~2.1 V and consistent with the J_{SC} of 15.5 mA/cm^2 of all-perovskite tandem solar cells.

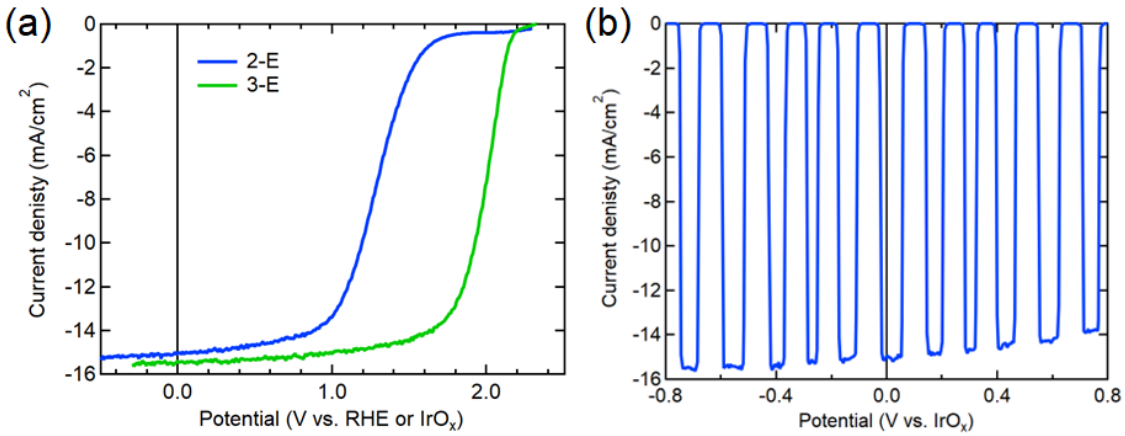

Figure 78. (a) LSV curves of a perovskite/perovskite tandem photoelectrode in three-electrode and two-electrode configurations. (b) LSV of a two-electrode photoelectrode under chopped light.

The operational stability of a perovskite tandem photoelectrode in the acidic electrolyte was measured using chronoamperometry under chopped light for 5 h, showing no sign of degradation (Figure 79). The average photocurrent density was 15 mA cm^{-2}, corresponding to a maximum STH efficiency of 18.45%.

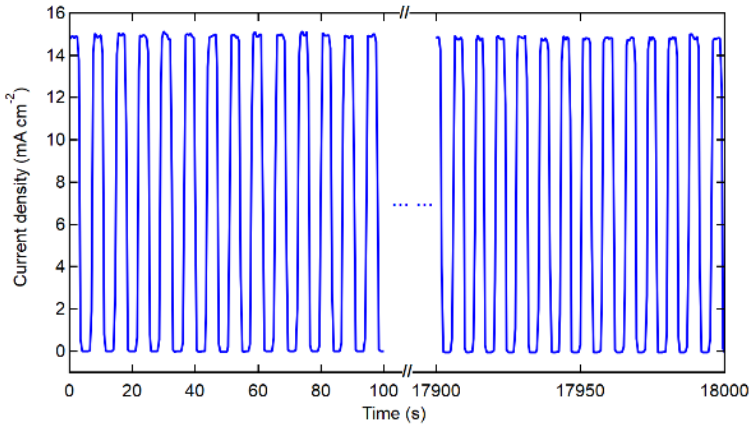

Figure 79. Chronoamperometry curves of a two-electrode APTPE under chopped light.

The long-term stability of a photoelectrode was measured under continuous one-sun illumination in an acidic electrolyte. A tandem device retained ~90% of initial STH efficiency after continuous operation for ~240 h at zero bias vs IrOx in 0.5 M H2SO4 electrolyte under AM1.5G illumination (Figure 80). The efficiency drop was mainly attributed to the degradation of the tandem perovskite photoabsorbers. The operating photocurrent of the perovskite tandem photoelectrodes decreased with time, which is likely attributed the instability of Sn-Pb perovskite layer caused by the ease of oxidation of Sn^{2+} to Sn^{4+} in the presence of structural defects and external stimuli as well as photo-induced corrosion caused by the acidic PEDOT: PSS hole-transport layer.

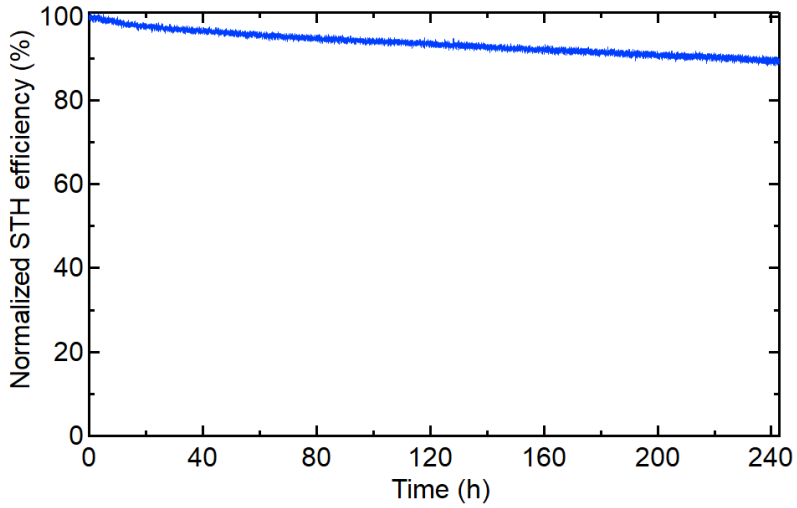

Figure 80. Long-term stability measurement of a perovskite/perovskite tandem photoelectrode under continuous AM1.5G one-sun illumination.

To better understand the degradation of perovskite/perovskite tandem photoelectrodes, we conducted pre- and post-catalysis analysis of devices and the corresponding catalysts and provided a more explicit discussion. Figure 81 compares the catalytic characteristics of a Pt metal foil used in all-perovskite tandem photoelectrode and wired IrOx anode for water reduction and oxidation half-reactions, respectively, in a 0.5 M H2SO4 before and after ~120 hours of water catalysis experiment. The pre- and post-catalysis HER/OER overpotentials for both electrodes remained unchanged, indicating the performance degradation of our tandem photoelectrodes is mostly attributed to the buried PV junctions. We further measured the external quantum efficiencies (EQE) of the two subcells in the tandem device and found that photocurrent densities in both subcells were reduced by ~ 1 mA/cm^2 after continuous operation for 120 hours (Figure 82). Therefore, the reduced STH efficiency is ascribed to the decreased photocurrent of the tandem photoelectrode.

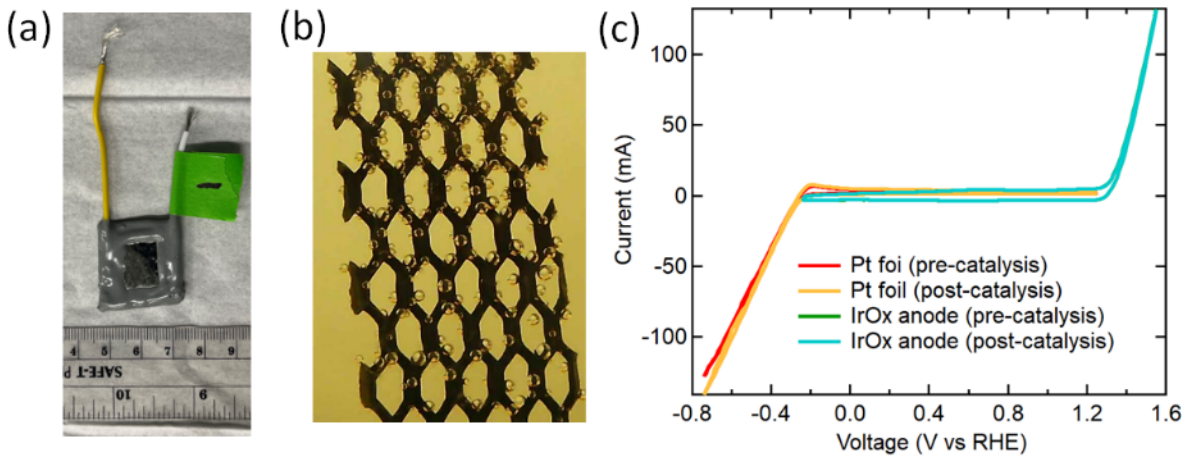

Figure 81. Photos of (a) a typical all-perovskite tandem photoelectrode and (b) an IrOx anode used for catalysis measurement. A wire labeled as "-" is connected to the Pt metal foil electrode to allow independent measurement of the catalytic characteristics of the metal foil. (b) LSV curves of the Pt foil used in a perovskite tandem photoelectrode and IrOx anode in a 0.5 M H2SO4 electrolyte before and after a catalysis stability measurement.

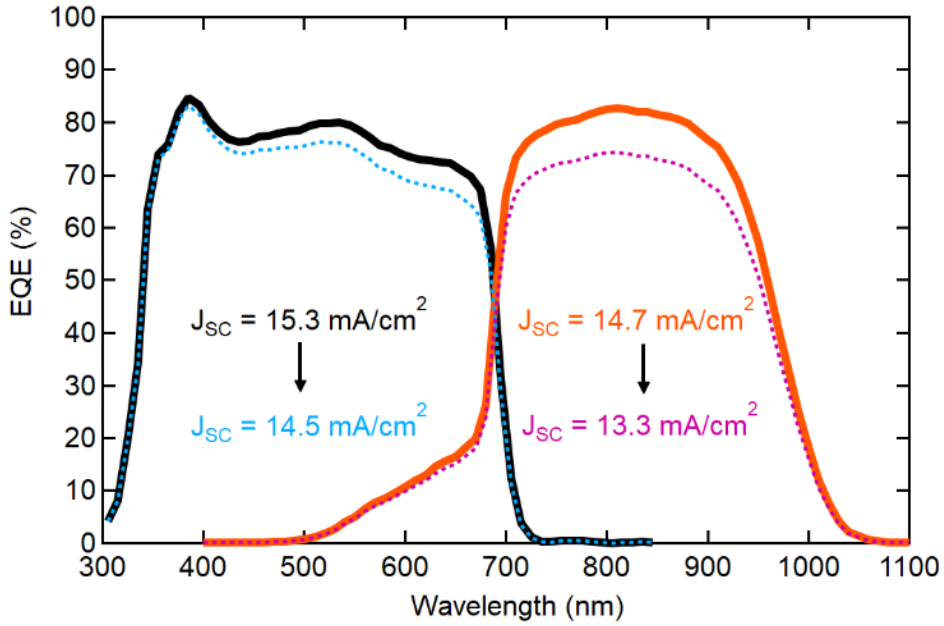

Figure 82. EQE of wide- and narrow-bandgap perovskite subcells before and after a catalysis stability measurement.

13. Optimizing perovskite/perovskite tandem photoelectrodes

Up to now, PEDOT: PSS is the almost irreplaceable hole transport layer (HTL) for high-efficiency low-bandgap perovskite and perovskite/perovskite tandem solar cells. However, polystyrene sulfonate dopants with a strong acid nature always accelerate the oxidation reaction of iodide ions ($2I^- \rightarrow I_2$) in halide perovskites. The resultant I_2 can further oxidize Sn^{2+} into Sn^{4+}, inducing massive interface defects and stability issues. In addition, high-efficiency low-bandgap perovskite solar cells still present a larger opening circuit voltage (V_{oc}) deficit (> 0.35 V) than normal-bandgap Pb-based PSCs (< 0.33 V). One of the key issues is the large valance band difference between the low-bandgap perovskite and HTL. Thus, seeking an ideal HTL material with better-aligned energy levels and less acidity plays a vital role in stabilizing and further advancing low-bandgap perovskite and perovskite tandem solar cells.

Poly[3-(4-carboxylbutyl)thiophene (P3CT) has been employed as the HTL for high-performance normal-bandgap Pb-based perovskite solar cells. Compared with widely used PEDOT: PSS, P3CT features less acidity and a deeper valance band. Still, its energy band levels do not sufficiently match with that of low-bandgap Sn-Pb perovskites.

To overcome this shortcoming, we propose molecular doping of P3CT with PbI_2 to adjust the electronic states in the thiophene main chain. As shown in Figure 83a, the electrons from the thiophene ring of P3CT can strongly interact with PbI_2 via coordination bonds, pulling electron density away from the thiophene chain of P3CT, resulting in enhanced p-type doping. As a result, the HOMO level of P3CT shifts down due to a higher hole density, minimizing the energy levels difference with the valence band of Sn-Pb perovskites.

Figure 83b-d compares the x-ray photoelectron spectroscopy (XPS) spectra of Pb-4f, I-3d, and S-2p from PbI_2, PC3T, and PC3T-PbI_2. As shown in Figure 83b, in comparison to PbI_2, the Pb 4f levels signals present a shift toward lower binding energy after forming P3CT-PbI_2, confirming the electron enrichment around Pb atoms. Figure 83c shows a slight shift of the I-3d signal toward a lower binding energy shift, in agreement with the electron withdrawing from PC3T to PbI_2. For the S-2p signals shown in Figure 83d, the S on thiophene displays a shift to higher binding energy after mixing with PbI_2, which indicates the electrons moving from thiophene toward Pb. These shifts confirm our hypothesis of the strong coordination between P3CT and PbI_2.

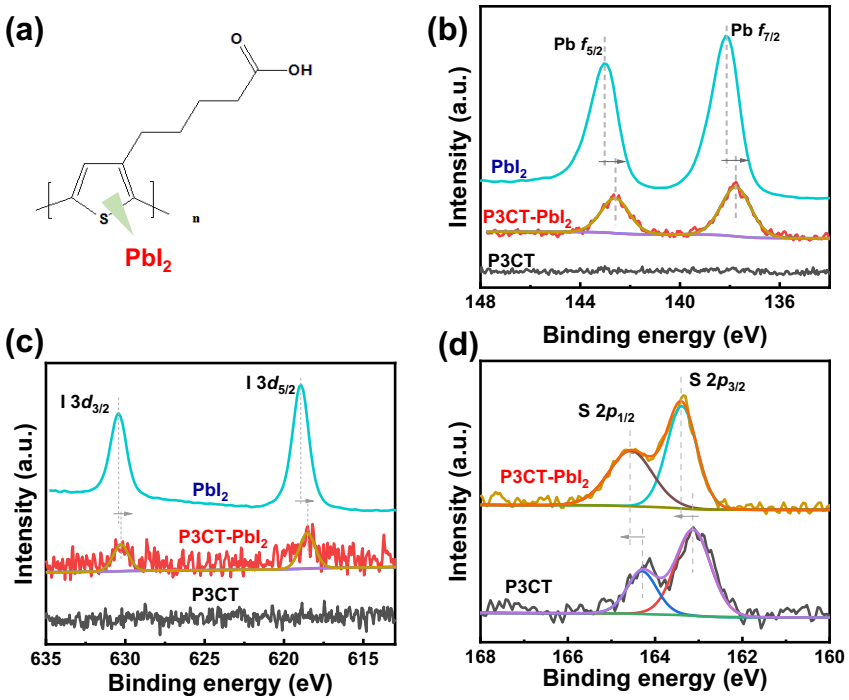

Figure 83. (a) Molecular structure of P3CT-PbI_2. (b-d) XPS spectra of Pb level (b), I level (c) and S level (d) of PbI2, P3CT, and their mixture.

Good crystallization and compact morphology of the perovskite absorber layer are also vital parameters for perovskite solar cells and photoelectrodes. To evaluate the crystalline quality of low-bandgap Sn-Pb perovskite grown on the functionalized P3CT HTLs, we examined the perovskite films on various HTLs via X-ray diffraction (XRD) measurements. As shown in Figure 84, all Sn-Pb perovskite films present the pure α phase of the perovskite structure with a strong (100) peak at 14.5° and a (200) peak at 28.7° diffraction angles. Taking the diffraction intensity into comparison, we identified that the crystallinity of perovskite film deposited on P3CT is higher than one deposited on PEDOT: PSS, and the intensity further increases after introducing PbI_2 into P3CT. The results reveal that the perovskite film grown on the target HTLs (P3CT-PbI_2) exhibits better crystallization than conventional PEDOT: PSS HTL.

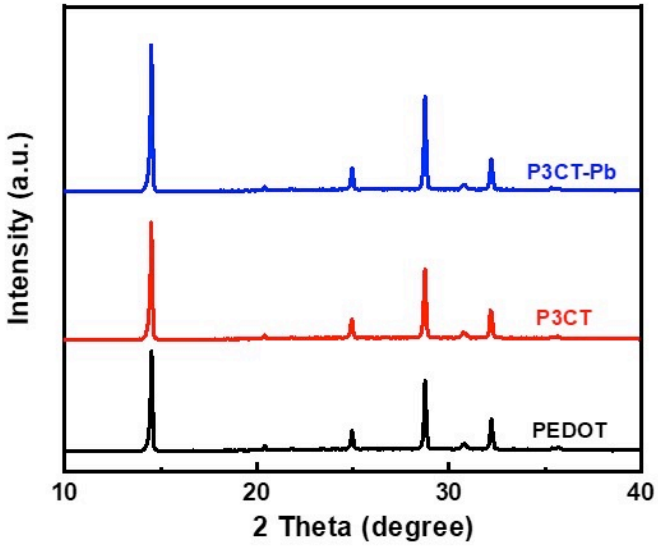

Figure 84. XRD patterns of Sn-Pb perovskite films coated on various HTLs.

We also conduct atomic force microscopy (AFM) and scanning electron microscopy (SEM) on the various perovskite films to observe the morphology and microstructure changes due to different HTLs (Figure 85). The surface morphology of Sn-Pb perovskite films grown on P3CT HTLs shows some grains with irregular shapes with uneven sizes. Interestingly, the perovskite grain domains are compact and have larger sizes. Particularly, obvious crystal terraces are identified in the Sn-Pb perovskite film deposited on the P3CT-PbI2 HTL, which indicates the high crystallinity of the perovskite grains. Associating growth dynamics of solution-process perovskite films, PbI_2 in P3CT-PbI_2 can act as the nucleation sites and form the heterogeneous nucleation crystal growth, thus yielding uniform morphology and high-quality crystallinity. Our AFM measurements show that the surface roughness of perovskite films is further decreased from 24.8 nm (PEDOT: PSS) to 20.5 nm (P3CT-PbI_2), profiling to better contact to the C_{60} ETL and better electron extraction.

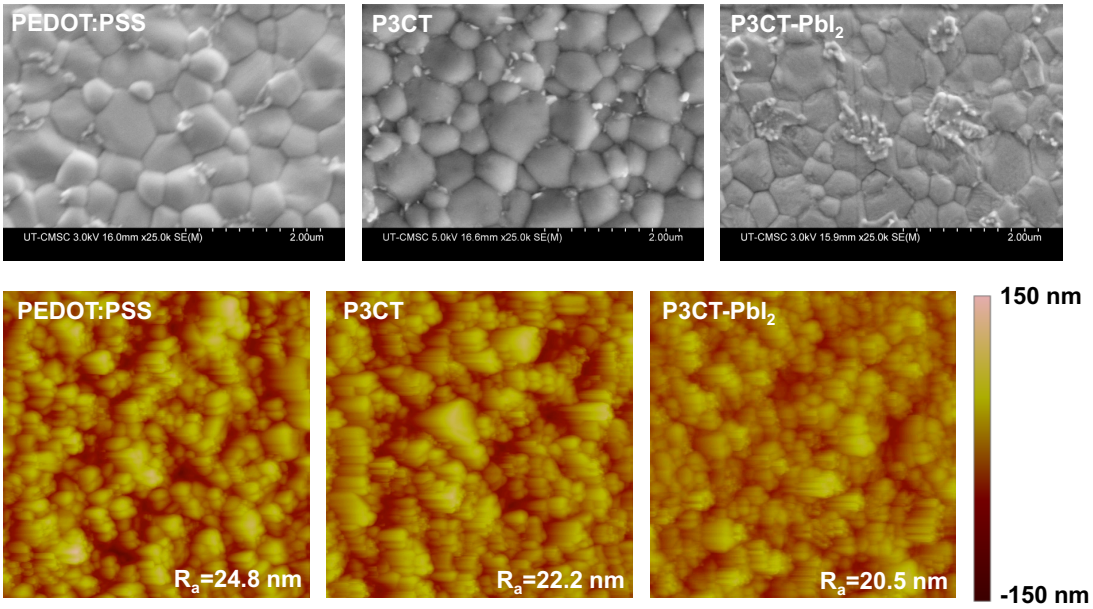

Figure 85. AFM and SEM images of perovskite films on different HTLs.

We fabricated the low-bandgap perovskite solar cells with a structure of glass/ITO/HTL/ perovskite/C_{60}/BCP/Ag based on various HTLs. We made 25 independent devices for each condition. Their PV performance statistics and detailed parameters are presented in Figure 86. The average efficiency is improved from 20% to 21.2% with improved V_{oc} and FF after replacing PEDOT:PSS with P3CT. After incorporating PbI_2 into the P3CT HTL, the device efficiency is further improved, approaching 22%, with a champion efficiency of 22.7%, FF of 80.2%, and V_{OC} of 0.89 V. The V_{OC} deficit is significantly minimized. The improved efficiency and V_{OC} are mainly attributed to the well-matched valence band of the Sn-Pb perovskite and the HOMO of P3CT as well as better crystallization of Sn-Pb perovskite films on the P3CT-PbI_2 HTL. This new HTL is expected to enable stable and efficient low-bandgap Sn-Pb perovskite solar cells and perovskite/perovskite tandem photoelectrodes. The stability measurement is ongoing, and the results will be reported in the next report.

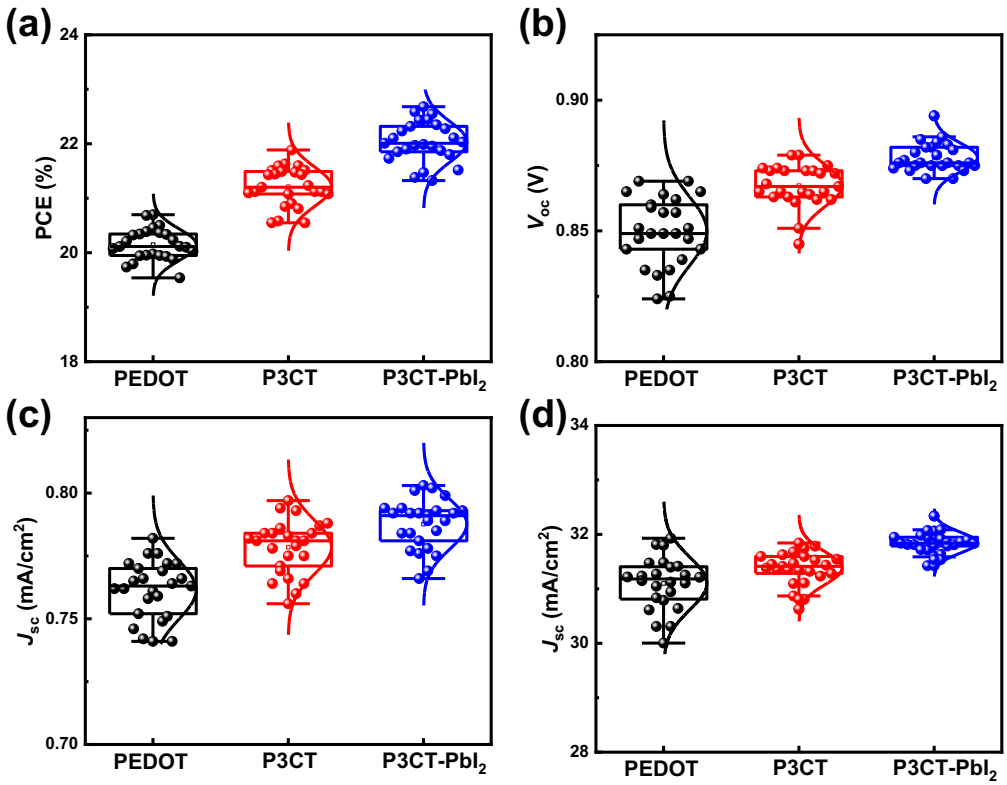

Figure 86. Photovoltaic parameters of LBG PSCs with various HTLs.

In comparison with acidic PEDOT: PSS (pH of around 2-3), P3CT-PbI_2 could effectively suppress the oxidization reactions at the buried interface of the Sn-Pb perovskite absorber layer, benefiting from its weak acidity (pH>6). The carbonyl group in P3CT could tightly bond to undercoordinated Sn atoms on the perovskite surface due to its stronger bonding energy than that of PSS and PEDOT moieties. Consequently, P3CT effectively suppresses the formation of iodine vacancy (V_I) defects and prevents Sn(II) oxidization. Interestingly, introducing the lead iodine (PbI_2) to P3CT modulates the charge distribution on thiophene chains, shifting Femi energy levels (E_f) down, which would minimize the valance band offset at the perovskite to reduce the V_{oc} deficit. Meanwhile, PbI_2 can act as the nucleation site that promotes the heterogeneous nucleation for uniform and high-quality Sn-Pb perovskite films. The perovskite films on P3CT-PbI_2 feature superior photoelectrical and crystalline properties and a stable buried interface compared with those on the PEDOT: PSS HTL.

Here, we investigated other alkali dopants in the P3CT by the Kelvin Probe Force Microscopy (KPFM) measurement of each HTL. As shown in Figure 87, the E_f of P3CT upshifted from -4.55 to -4.43 eV after adding MA. In contrast, when P3CT was functionalized with the metal cations of Cs and Pb, its E_f was downshifted to -4.61 and -4.98 eV. The higher p-type doping benefits minimize the valance band offset between the P3CT HTL and Sn-Pb perovskite absorber, enhancing V_{OC} of the device. Among all tested HTLs, P3CT-PbI_2 features the strongest p-type doping and thus may yield the highest V_{OC} and efficiency.

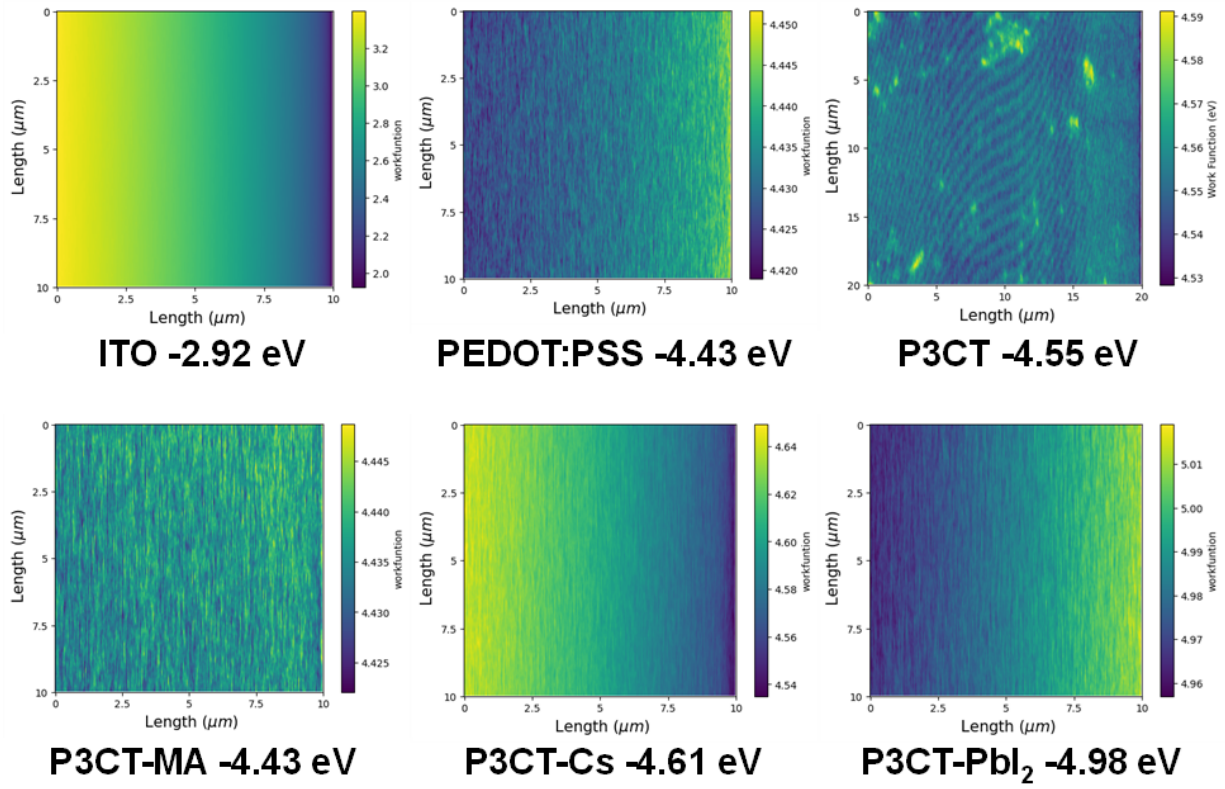

Figure 87. KPFM of the different HTLs on ITO substrates.

To further evaluate the photoelectrical properties of Sn-Pb perovskites on different P3CT-based HTLs, we measured the photoluminescence (PL) spectra of the corresponding perovskite films. As shown in Figure 88, compared with bare P3CT, the perovskite film on P3CT-MA shows a higher PL intensity owing to the passivation effect of MA molecules. The perovskite film on P3CT-CsOH shows higher PL intensity than P3CT and P3CT-MA. The perovskite film P3CT-PbI_2 shows the highest intensity, revealing the highest film quality and the most suitable for tandem devices.

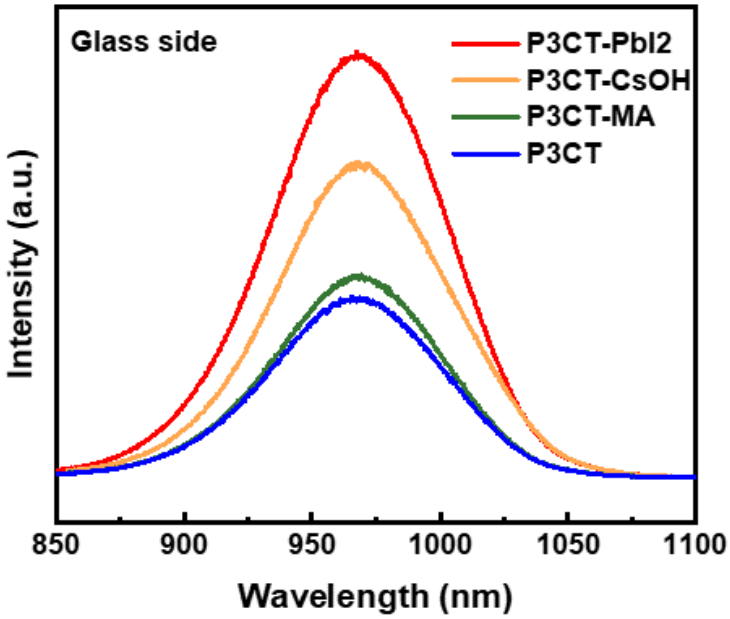

Figure 88. PL spectra of Sn-Pb perovskite films on different P3CT-based HTLs.

PEDOT: PSS is a non-ideal contact layer for iodine-based perovskite because it is likely to catalyze the oxidation reaction of iodide to from iodine monomer ($2I^- - 2e^- \rightarrow I_2$) due to its hygroscopic and strongly acidic nature. Even worse, I_2 can further oxidize Sn^{2+} into Sn^{4+} in Sn-Pb perovskites, forming n-type V_I and deep-energy-level V_{Sn} defects at the perovskite/PEDOT: PSS interface. These detrimental defects greatly hinder charge carrier extraction dynamics with severe non-radiative recombination at the anode. Moreover, the halide redox reaction at the buried interface can be exacerbated under stressed stimuli, leading to poor stability of PEDOT: PSS-based LBG and tandem perovskite photoelectrodes.

To better understand the degradation in LBG perovskites, we aged the Sn-Pb perovskite films on PEDOT: PSS and P3CT-PbI_2 under 0.9 sun illumination and 60 °C condition for 120 h. The films were encapsulated with a cover glass using UV-curable adhesive to prevent water and oxygen ingress. After aging, we peeled off the perovskite films from the ITO substrates and measured the SEM images. As shown in Figure 89a-b, the fresh samples appeal to be partially covered by the HTLs, indicating the strong interaction between perovskite and HTLs. Some residual DMSO molecules are likely trapped at the buried interface, resulting in voids under the bottom side. The Sn-Pb perovskite film deposited on P3CT-PbI_2 (Figure 89a, left) exhibits fewer pinholes than the film on the PEDOT: PSS HTL (Figure 5b, left), thanks to the more uniform heterogeneous nucleation enabled by the embedded Pb cations in the HTL. After aging for 120 h, the target sample deposited on P3CT-PbI_2 remained unchanged morphology (Figure 89a, right), whereas noticeable decomposition of perovskite on PEDOT: PSS was observed with many voids and larger size (Figure 89b, right). Additionally, for the PEDOT: PSS sample, the perovskite grains became clearer with less coverage of PEDOT: PSS on the perovskite surface, indicating poor adhesion between the PEDOT: PSS HTL and perovskite absorber layer and interface instability. In contrast, the perovskite on P3CT-PbI_2 (target) remained similar to the fresh sample, revealing a more stable buried interface of P3CT-PbI_2/perovskite.

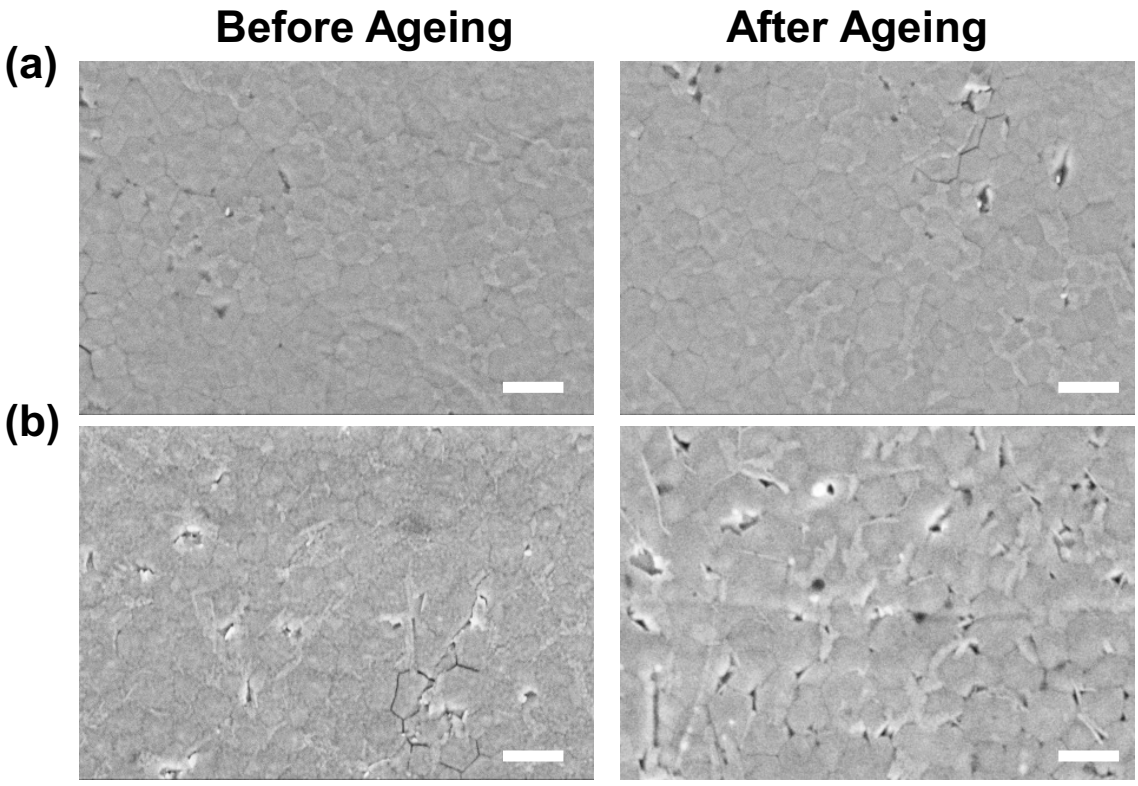

Figure 89. SEM images of the buried interface of perovskite on (a) P3CT-PbI_2 and (b) PEDOT: PSS before (left) and after (right) aged at 0.9 sun and 60 °C condition for 120 h.

To study the oxidization reaction at different HTLs, we peeled off the perovskite films, soaked them into a toluene solution, and stressed them under the same aging conditions for 72 h. Figure 90 shows pronounced I_2 and SnI_4 peaks of the reference sample (perovskite on PEDOT: PSS). The solution turned red after it was aged for 72 h. In comparison, the solution with the target sample (perovskite on P3CT-PbI_2) remained colorless with only weak signals of released I_2 and SnI_4, further proving the more stable buried interface of perovskite and P3CT-PbI_2.

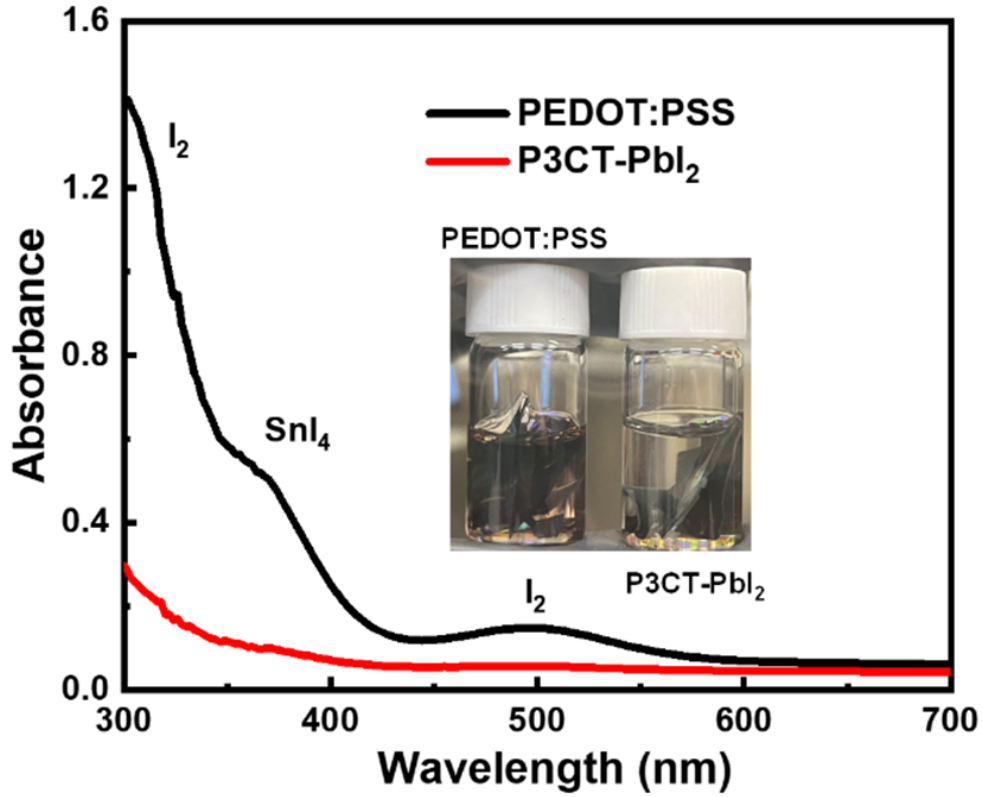

Figure 90. UV-vis spectra of the solution for reference (on PEDOT: PSS) and target (on P3CT-PbI_2) perovskite films. The inset image is a photo of the corresponding solutions.

We measured the stability of NBG Sn-Pb PSCs via maximum power tracking (MPP) under ambient conditions (temperature around 30 °C and relative humidity around 50%). As shown in Figure 91, the device based on the PEDOT: PSS HTL exhibited poor operational stability, with the efficiency decreasing to below 70% of its initial value within 400 h. In sharp contrast, the target device based on the P3CT-PbI_2 HTL retained >85% of its initial efficiency after tracking for more than 1,000 h. We would expect the lifetime of all-perovskite tandem photoelectrodes to be significantly improved with P3CT-PbI_2 as the HTL。

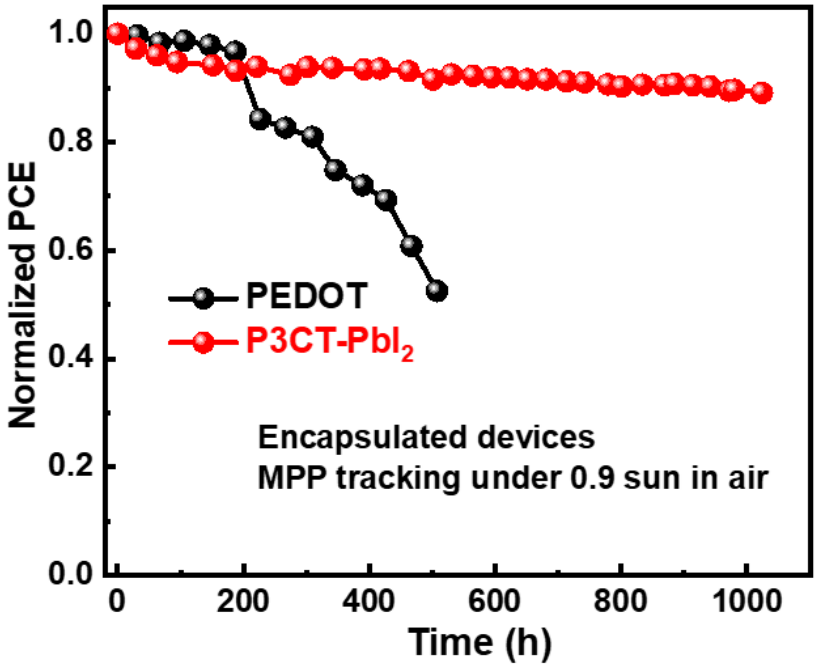

Figure 91. Operational stability measurement at maximum power point for the reference (PEDOT: PSS) and target (P3CT-PbI_2) LBG Sn-Pb perovskite devices.

We used to dissolve P3CT and PbI_2 powders in a pure DMF solvent to prepare the P3CT HTL. However, we found that the DMF solvent is likely to diffuse into and damage the front subcell during the coating of P3CT-PbI_2 in processing tandem photoelectrode integration. Consequently, solvent-damaged tandem devices typically show an abnormal J-V performance with much inferior PV parameters than standard devices (Figure 92). To avoid the solvent damage caused by DMF during the tandem integration, we prepared a high concentration (10 mg/mL) P3CT-PbI_2 solution first and then diluted it into 2 mg/mL with chlorobenzene. Using this approach, we are able to reproducibly fabricate the working tandem devices with a power conversion efficiency of more than 26% (Figure 92).

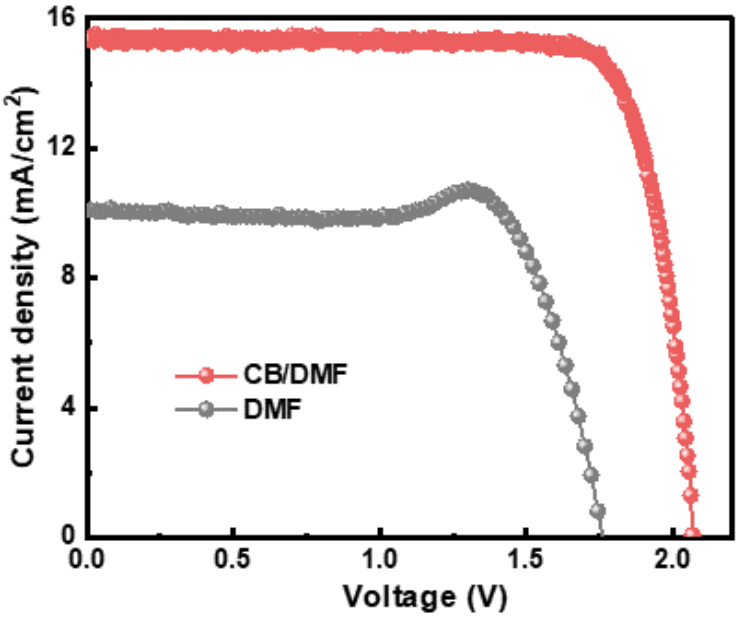

Figure 92. J-V curves of the tandem devices based on DMF-based (black) and CB/DMF mixed P3CT-PbI_2 HTLs.

Figure 93 shows the device structure of our current design of an all-perovskite tandem photoelectrode and the corresponding cross-section SEM image. The device consists of a film stack of ITO/NiOx/Me-4PACz/1.78-eV WBG perovskite/C_{60}/SnO_2-Au/P3CT/1.26-eV LBG perovskite/C_{60}/BCP/Ag. The tandem PV film stack is then mechanically integrated into a protective metal foil loaded with Pt nanoparticle catalysts using a conductive graphite/silver epoxy paste and encapsulated with non-conductive epoxy.

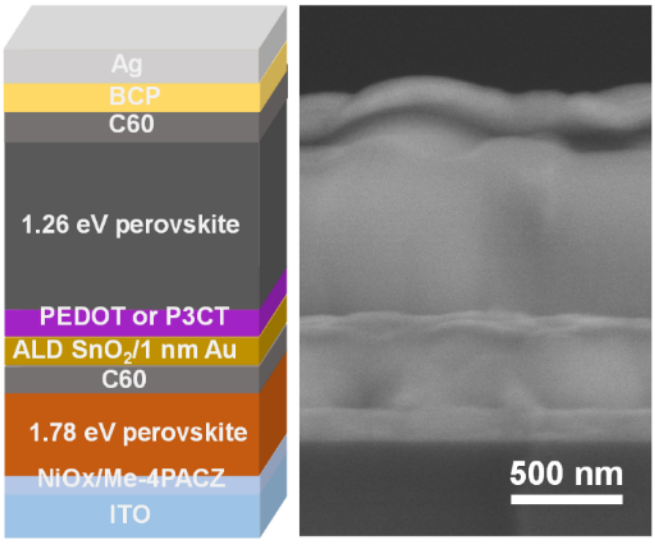

Figure 93. Schematic diagram and cross-section SEM image of an all-perovskite tandem device.

The J-V curves of champion efficiencies for all-perovskite tandem devices based on PEDOT: PSS and P3CT-PbI_2 are presented in Figure 194a. The device based on PEDOT: PSS delivers a champion efficiency of 26.4%, with a V_{OC} of 2.096 V. The P3CT-based tandem shows a higher efficiency of 27.9% with a higher V_{oc} of 2.147. The target tandem device also presents a higher and stable steady-state power output efficiency (27.6%) than the reference cell (25.9%), as shown in Figure 94b.

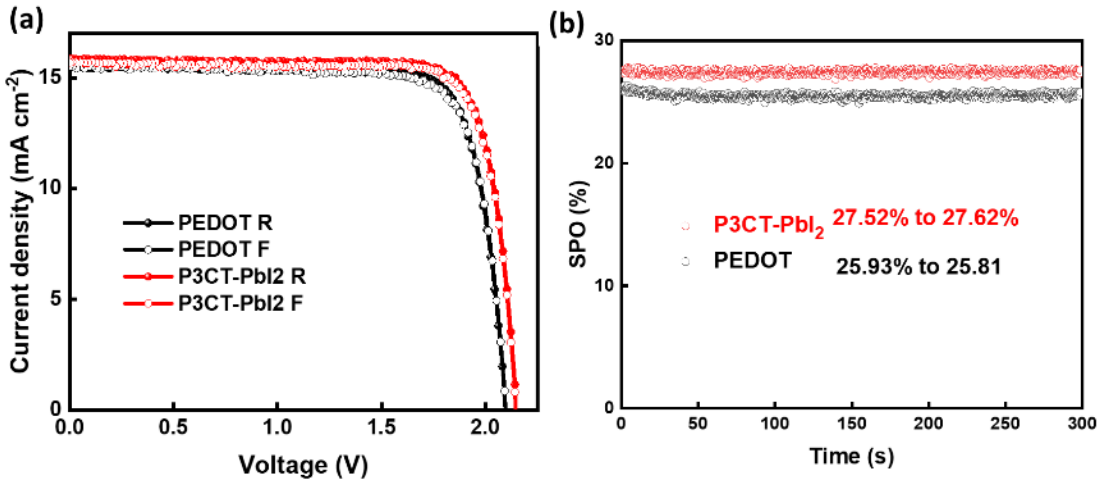

Figure 94. (a) J-V curves and (b) SPO efficiency of an all-perovskite tandem device.

Owing to the improved crystallization and carrier extraction properties of Sn-Pb perovskite films deposited on the P3CT-PbI_2 HTL, the target all-perovskite tandem devices present good reproducibility with a higher average efficiency than the PEDOT: PSS-based tandem (Figure 95). The average power conversion efficiency of our tandem cells is more than 27%.

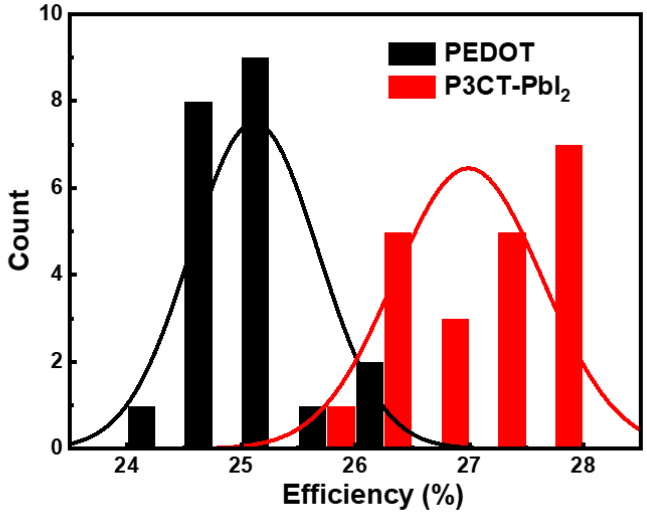

Figure 95. Efficiency statistics of all-perovskite tandem devices.

We also measured the operational stability of target tandem devices, as shown in Figure 96. The target all-perovskite tandem device exhibited excellent operational stability under AM1.5G illumination in ambient air, remaining >90% of its initial efficiency after power tracking for 1,000 h.

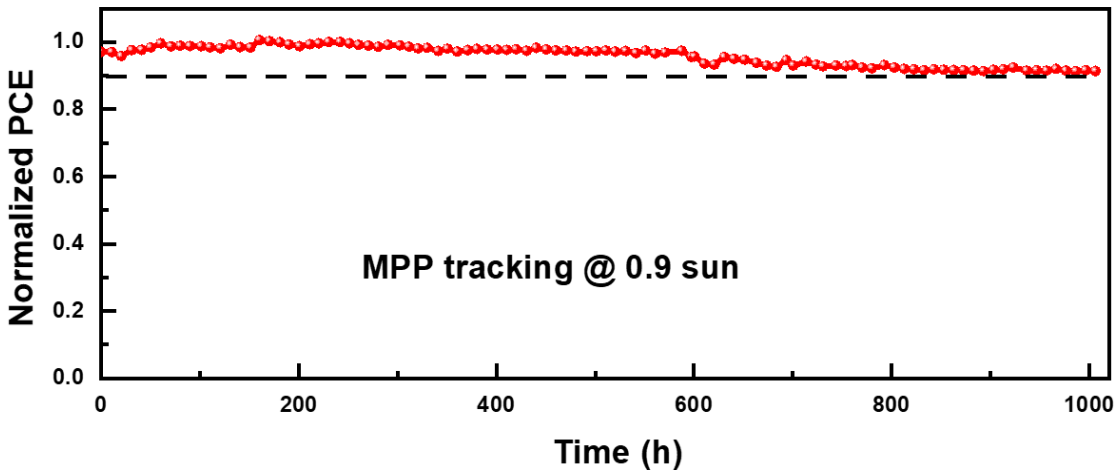

Figure 96. MPP tracking of the optimized device.

We then measured the solar water splitting performance of all-perovskite tandem photoelectrodes wired to an IrO_x anode in a two-electrode configuration in a 0.5 M H_2SO_4 electrolyte. Figure 97 plots the cyclic voltammetry curves of three tandem photoelectrodes. All three tandem photoelectrodes show similar behavior, demonstrating a decent reproducibility of the tandem devices. The J-V hysteresis of the perovskite-perovskite tandem junctions is negligible. The hysteresis at positive bias is mainly attributed to the oxidation of OH^- anions around the photoelectrode and may also be influenced by the dissolved multivalent transition metal cations (Fe, Ni, Cr, etc.) from stainless steel. Nonetheless, the tandem photoelectrodes show unassisted solar water-splitting performance at zero bias voltage, with a short-circuit current density of ~13.5 mA/cm^2, corresponding to an estimated solar-to-hydrogen conversion efficiency of 16.6%. We also measured the long-term stability of our all-perovskite tandem photoelectrodes. One all-perovskite tandem photoelectrode exhibited an initial STH conversion efficiency of 16.7% and retained 15.2% STH efficiency after 500 hours of continuous operation under simulated AM1.5G illumination (Figure 98). We will continue improving the efficiency and stability of our all-perovskite tandem photoelectrodes in the next quarter.

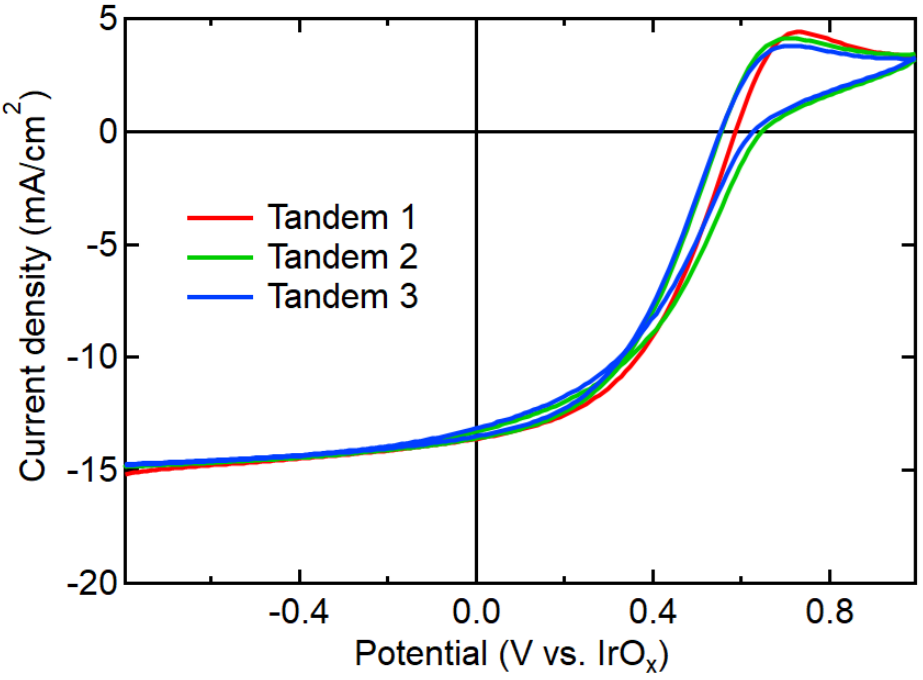

Figure 97. Cyclic voltammetry measurement results of three all-perovskite tandem photoelectrodes.

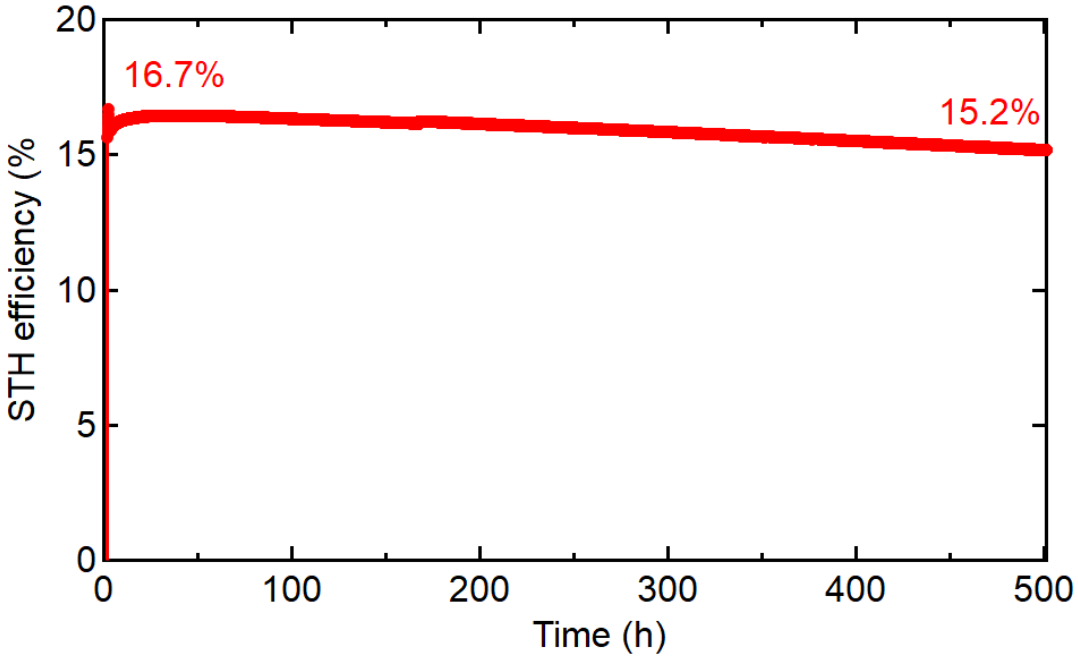

Figure 98. Stability measurement of an all-perovskite tandem photoelectrode.

We then conducted density-functional theory (DFT) calculations to understand the working mechanism of P3CT on stabilizing the perovskite/HTL interface.

Acidic functional groups are commonly included in the organic HTL of perovskite solar cells (PSCs) to form strong bonds with both the transparent conducting oxide (TCO) on the substrate and perovskite layer, promoting uniform perovskite film deposition over a large area. However, acid dissociation from HTLs may introduce a severe challenge to the durability of PSCs. Notably, the stability of most high-efficiency Sn-containing PSCs and all-perovskite tandem solar cells is seriously limited by the -SO_3H group in PEDOT:PSS, owing to the inevitable surface reactions, as shown in Figure 99a.

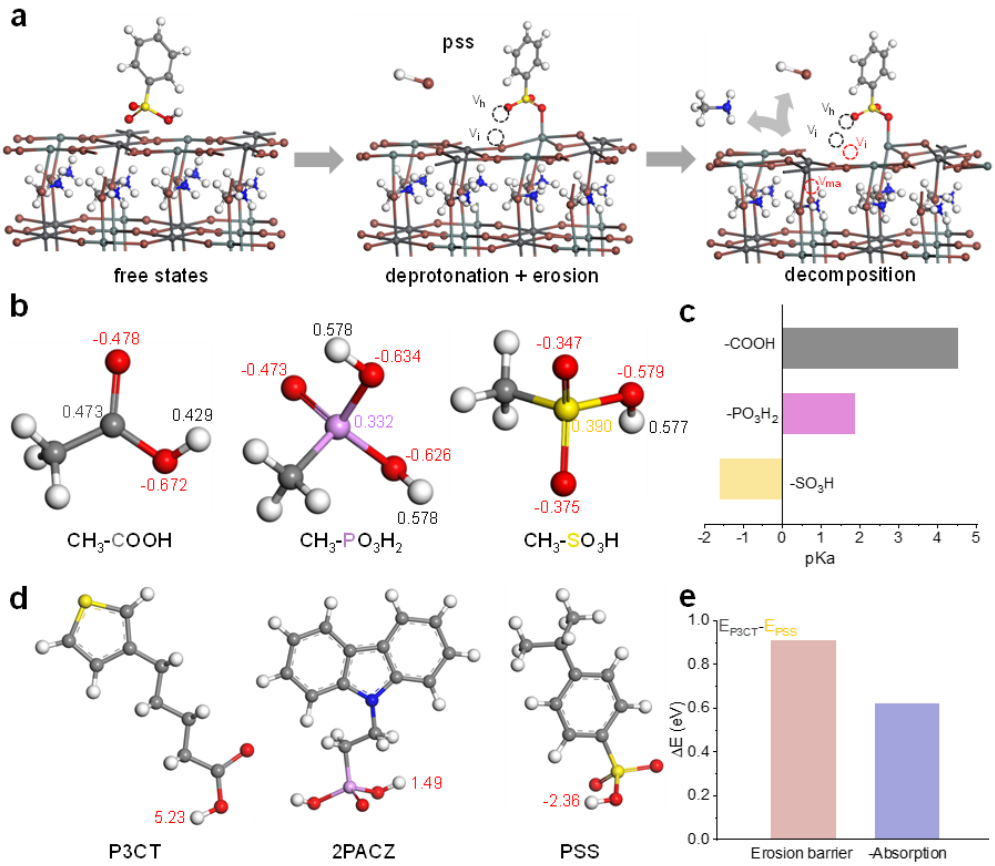

Figure 99. (a) The DFT simulations of the reaction and decomposition at the Sn-Pb perovskite/PEDOT:PSS interface. (b-c) Hershfield charge distributions (b) and the calculated pK_a (c) of the sulfonate, pyrophosphate and acetate groups and the molecules are constructed with the methyl end. (d) The molecular structures and pK_a numbers (red) of the reported HTLs for high-efficiency PSCs. (e) The energy difference (E_{P3CT}-E_{PSS}) of the surface bonding energy and the energy barriers of acidic erosion.

Figure 99b presents the Hirshfeld charge distribution in representative molecules. Their relative acidity, defined as the capability to donate a proton and form a conjugate base, can be evaluated by the negative charge located on the oxygen atom bonded with the hydrogen. The calculated charge distributions on the O of the -OH in carboxylic (-COOH), phosphonate (-PO_3H_2), and sulfonate (-SO_3H) moieties attached with a methyl group are -0.672, -0.626, and -

0.579, respectively. A more negative charge located on the O of -OH indicates a stronger O-H bond and a more polarized (less stable) conjugate base, corresponding to a lower acidity. Comparing these acidic groups, $-PO_3H_2$ and $-SO_3H$ show higher acidity than -COOH because of more delocalized negative charge distribution across three resonant O atoms than two, making their conjugate bases easier to accommodate the negative charge and more stable. Additionally, $-SO_3H$ with more electronegative S (2.58) than $-PO_3H_2$ with P (2.19) is better at accepting the negative charge, resulting in less electron polarizability and a more stable conjugate base, corresponding to an easier trend to lose the proton. To quantify the deprotonation properties of different acidic functional groups, we calculated the acid dissociation constant (pK_a) for these functional groups (Figure 99c). The sulfonate group shows the strongest acidity with pK_a of -1.61, while pyrophosphate and acetate groups show less acidity with pK_a of 1.87 and 4.54, respectively. Therefore, the close-to-neutral (high pK_a) functional group based on -COOH can potentially ameliorate interface degradation at the HTL/Sn-Pb perovskite interface.

Figure 99d shows the molecular structure and pK_a of the commonly used HTLs. The PSS presents an even lower pK_a (-2.36) than the CH_3-SO_3H, which is attributed to the increased electron delocalization of the benzene-SO_3 moiety in its conjugate base. In comparison, the widely used phosphonate acid carbazole (PACz)-based self-assembled monolayer HTL, such as 2PACz, shows a positive pK_a of 1.49, which may ameliorate the acid dissociation issues. Yet, their medium-strong acidity (pK_a<2) may still present a long-term stability challenge. In contrast, P3CT with an acetate group is difficult to deprotonate with a higher pK_a of 5.23. We found that the P3CT solution shows an almost neutral nature (pH 6-7), which is expected to suppress the interface decomposition significantly for efficient and stable Sn-Pb perovskite and all-perovskite tandem solar cells.

We then calculated energy barriers for the deprotonation-erosion process on the Sn-Pb perovskite surface with P3CT and PSS molecules, and the energy differences of P3CT and PSS were presented in Figure 99e. After replacing PSS with P3CT, the energy barrier of the acidic reaction on perovskite is increased by 0.91 eV, greatly hindering the undesirable acidic erosions at the buried interface. Additionally, P3CT also shows a higher bonding strength on perovskite than the PSS, with an energy difference ΔE_b of 0.62 eV, which prevents surface defect formation and inhibits the decomposition of perovskite. Furthermore, the energy barrier for the volitation of MA and HI from perovskite after deprotonation/erosion is increased by 0.1 eV with P3CT molecules. The calculations reveal that P3CT can suppress acidic erosion and increase bonding energy to the perovskite, promising superior efficiency and stability in all-perovskite tandem solar cells.

We compared the thermal stability of the low-bandgap perovskite solar cells with a structure of ITO/HTLs/Sn-Pb perovskite/C60/BCP/Ag by heating the devices on a 60 ˚C hotplate and collected the J-V curves regularly with time. As shown in Figure 100, the device based on PEDOT:PSS presented fast degradation and loss of its 80% efficiency after aging for 500 h. In comparison, the device based on the P3CT HTL exhibits much-improved stability, retaining 90% of its initial efficiency after the same aging condition.

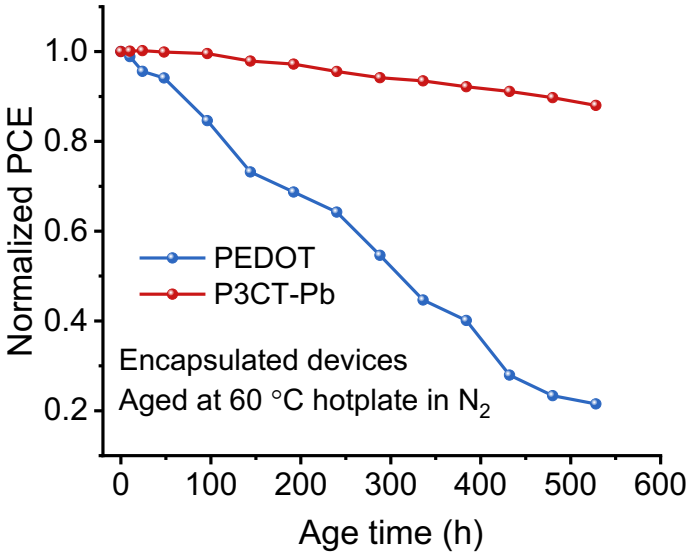

Figure 100. Thermal stability of low-E_g PSCs placed on a 60 ˚C hotplate in a glovebox.

We fabricated the all-perovskite tandem solar cells and photoelectrodes for solar-driven hydrogen production experiments. Figure 101a plots the J-V curves of the champion tandem device. The tandem device shows an efficiency of 26.8%, with a high V_{OC} of 2.11 V and a J_{SC} of 15.6 mA/cm^2. Figure 101b displays the spectral response of both subcells. The integrated J_{SC}s of the top and bottom subcells are 15.5 and 15.6 mA/cm^2, respectively, in agreement with the tandem's J_{SC} measured from the J-V scans. Further optimizations are needed to improve the performance of tandem devices, such as improving the quality of ALD-SnO_2, the film quality of both wide-E_g and low-E_g perovskites, and the recombination junctions.

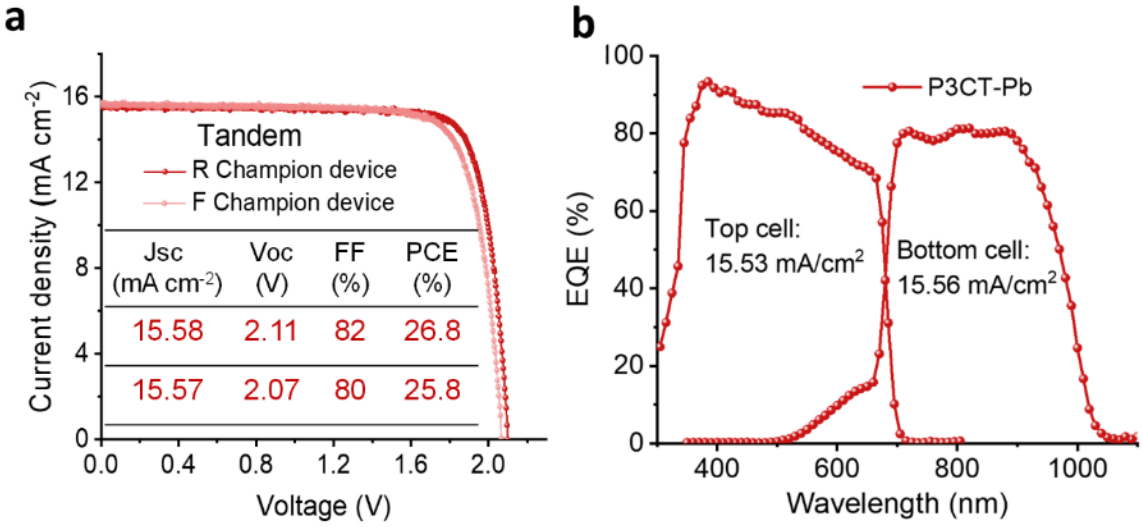

Figure 101. (a) J-V and (b) EQE curves of the champion efficiency of the tandem solar cells.

We then measured the solar water splitting performance of all-perovskite tandem photoelectrodes wired to an IrO_x/Ti anode in a two-electrode configuration in a 0.5 M H_2SO_4 electrolyte. The tandem photoelectrodes show unassisted solar water-splitting performance at zero bias voltage, with a short-circuit current density of ~14 mA/cm^2, corresponding to an estimated solar-to-hydrogen conversion efficiency of 17.2%. We tracked the long-term stability of the perovskite-perovskite tandem photoelectrode. The tandem photoelectrode retained an STH efficiency of 13.9%, corresponding to >80% of its initial efficiency, after 500 hours of continuous operation under simulated AM1.5G illumination (Figure 102). The efficiency drop occurred mainly in the first 200 hours. After that, hydrogen generation performance was relatively stable after ~200 hours.

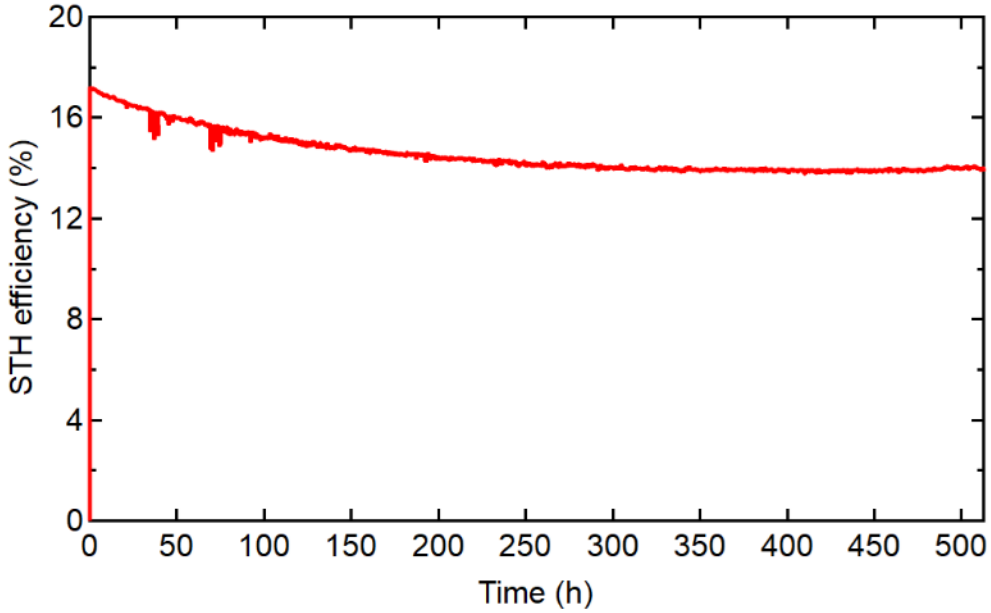

Figure 102. Stability measurement of an all-perovskite tandem photoelectrode.

We continued measuring the solar water splitting performance of perovskite/perovskite tandem photoelectrodes wired to an IrO_x/Ti anode in a two-electrode configuration in a 0.5 M H_2SO_4 electrolyte. We tested 5 other devices. All tandem photoelectrodes show unassisted solar water-splitting performance at zero bias voltage. The average zero-biased photocurrent density is ~14 mA/cm^2, corresponding to an estimated solar-to-hydrogen conversion efficiency of 17%. We tracked the long-term stability of these perovskite/perovskite tandem photoelectrodes. The most stable tandem photoelectrode retained STH efficiencies of ~14%, corresponding to ~80% of its initial efficiency, after ~500 hours of continuous operation under simulated AM1.5G illumination (Figure 103).

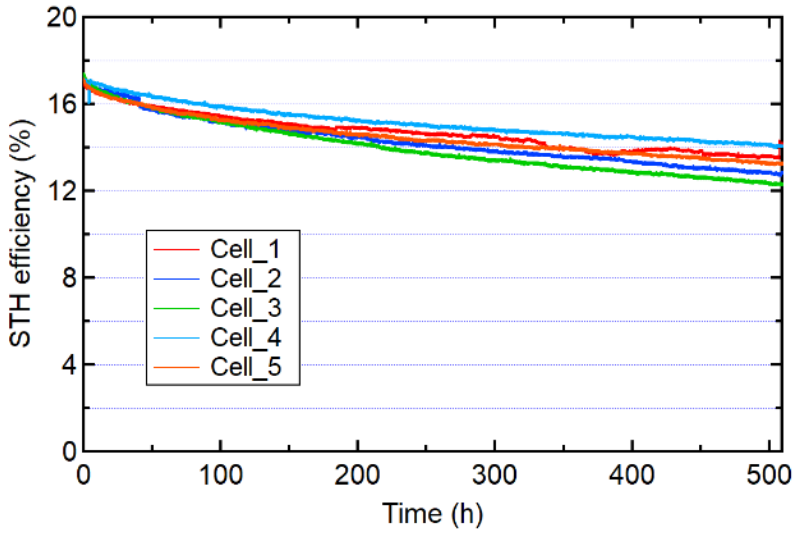

Figure 103. Stability measurement of an all-perovskite tandem photoelectrode.

14. Technoeconomic analysis of perovskite/perovskite tandem photoelectrodes

To further prove the potential application of perovskite/perovskite tandem photoelectrodes, we conducted a technoeconomic analysis using a bottom-up cost analysis method. The basic assumptions for perovskite tandem film stack manufacturing are the same as reported in our previous work. The fabrication process of all-perovskite tandem photoelectrode is shown in Figure 104. The process includes (1)TCO glass cleaning, (2) solution-deposition of top HTL, (3) solution-deposition of wide-Eg perovskite, (4) evaporation of top ETL, (5) ALD/sputter deposition of an interconnecting layer, (6) solution-deposition of bottom HTL, (7) solution-deposition of narrow-Eg perovskite, (8) evaporation of bottom ETL, (9) ALD deposition of bottom blocking layer, (10) evaporation of back contact layer, (11) printing of conductive paste, (12) mechanical integration of metal foil, (13) soldering of Cu external wire, (14) epoxy sealing.

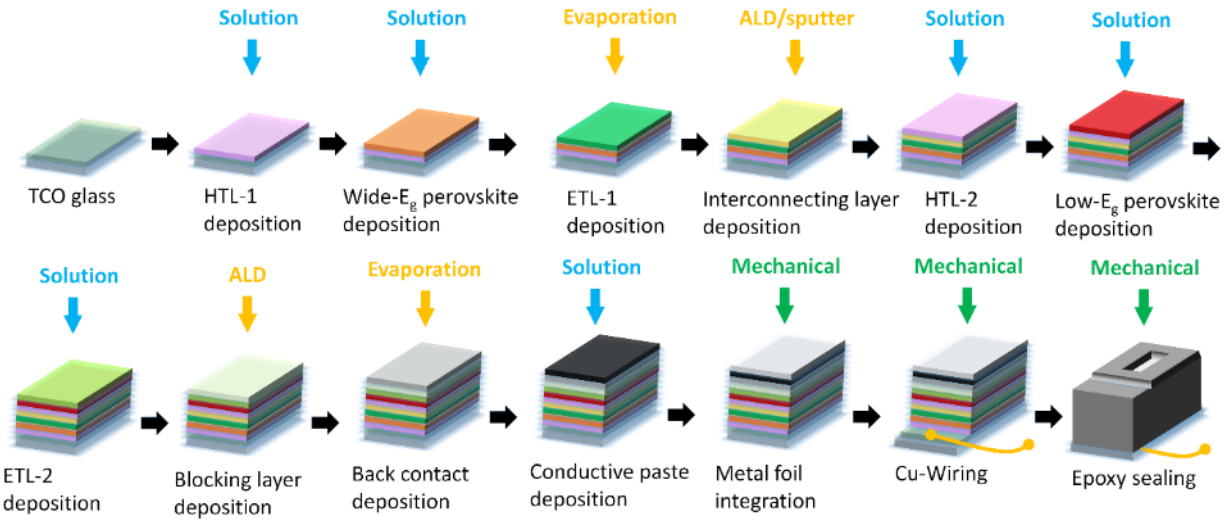

Figure 104. Schematic flow diagram of all-perovskite tandem photoelectrode fabrication procedure.

Each step contains five cost segments, including materials, utilities, labor, depreciation, and maintenance. The cost of each segment is tabulated in Table 1. The total costs of each processing step were summed up to show the cost of each process.

The manufacturing cost per unit area of the perovskite module (C) is calculated by adding up the costs of the individual manufacturing process in Figure S2 using the equation below:

$$C = \sum_i (M_i + U_i + L_i + E_i + D_i) \qquad \text{(Eq.1)}$$

Here, we consider the costs per unit area ($/m^2) for raw materials (M_i), utilities (U_i, including electricity and water), engineering and production line labor (L_i), equipment maintenance (E_i), and depreciation of the equipment and building (D_i) in the i^{th} step of the process. Because of the high material cost of precious metal Pt (Figure 105) and similar catalytic characteristics of Pt foil and Pt-coated stainless steel (Figure 106), we model the manufacturing cost of photoelectrodes using a stainless-steel foil functionalized with a few nm of Pt catalysts.

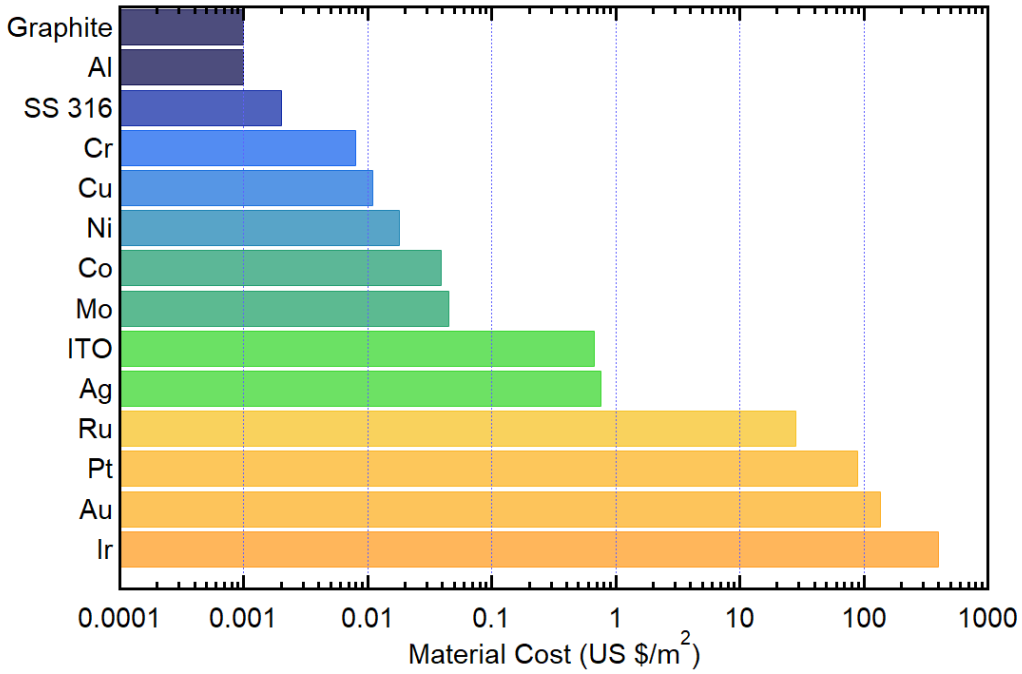

Figure 105. Materials cost comparison for 100 nm thick electrode materials.

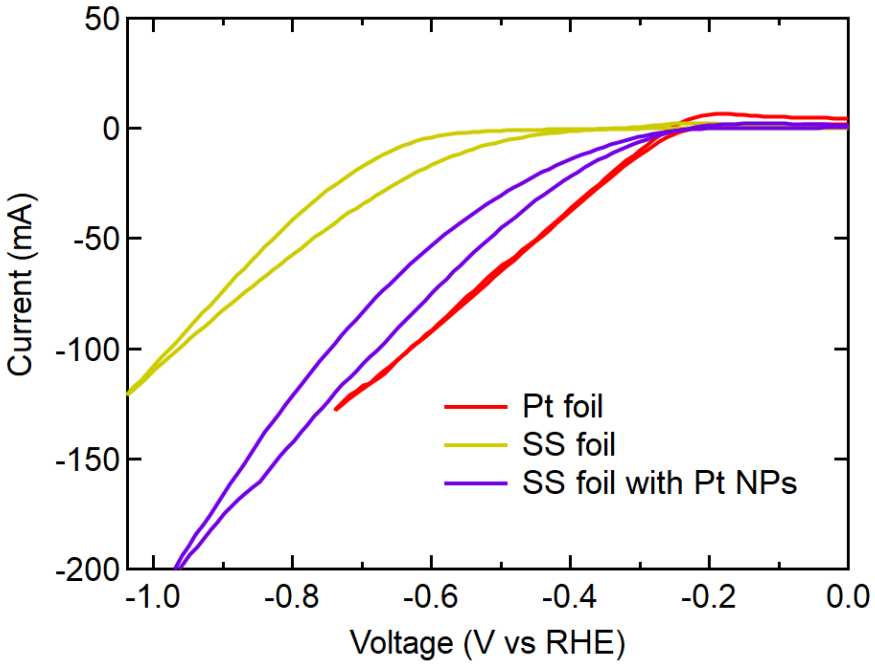

Figure 106. LSV curves of a Pt foil, a stainless steel (SS) foil, and a SS foil functionalized with Pt nanoparticles in a 0.5 M H_2SO_4 electrolyte.

Figure 107 and Table 1 exhibit detailed cost distributions for each manufacturing step. The expected manufacturing cost of perovskite/perovskite tandem photoelectrodes is ~\$30/m^2, which is more than two orders of magnitude lower than the production cost of III-V tandem devices at ~\$18,000/m^2. Notably, the all-perovskite tandem semiconductor film stack contributes

$8.1/m2, taking only 27% of the total photoelectrode costs. The detailed cost distribution is plotted in Figure 108a. The costs can be further reduced through the cost reduction of the balance of panel components, including glass substrate, conductive paste, metal foil/catalysts, and epoxy sealing. Particularly, the high photovoltage of more than 2 V for APTPEs may enable low-cost HER and OER catalysts, which would be a direction for future research.

Table 1. Estimated cost segment for each fabrication step of perovskite/perovskite tandem photoelectrodes.

No	Process	Materials ($/m^2)	Utilities ($/m^2)	Labor cost ($/m^2)	Depreciation ($/m^2)	Maintenance ($/m^2)
1	Front glass	4.500	0.259	0.232	0.160	0.011
2	TCO	0.806	0.394	0.116	0.901	0.232
3	HTL-1	0.015	0.130	0.038	0.297	0.083
4	Wide-E_g Perovskite	0.244	0.062	0.502	0.238	0.032
5	ETL-1	0.010	0.130	0.038	0.297	0.083
6	Interconnecting layer	0.403	0.197	0.116	0.901	0.232
7	HTL-2	0.015	0.130	0.038	0.297	0.083
8	Narrow-E_g perovskite	0.366	0.062	0.502	0.238	0.032
9	ETL-2	0.010	0.130	0.038	0.297	0.083
10	Metal contact	0.603	0.236	0.077	0.654	0.158
11	Conductive paste	1.710	0.066	0.270	0.203	0.023
12	Metal foil	4.175	0.130	0.038	0.297	0.083
13	Cu wire	3.200	0.008	0.019	0.201	0.023
14	Sealing	3.075	0.029	0.096	0.374	0.037

Note: Metal foil: 100 μm stainless steel with 3 nm Pt catalysis. Cost inventory is acquired from surveys on manufacturers and suppliers from online trading websites, global value pricing databases, government reports, and literature.

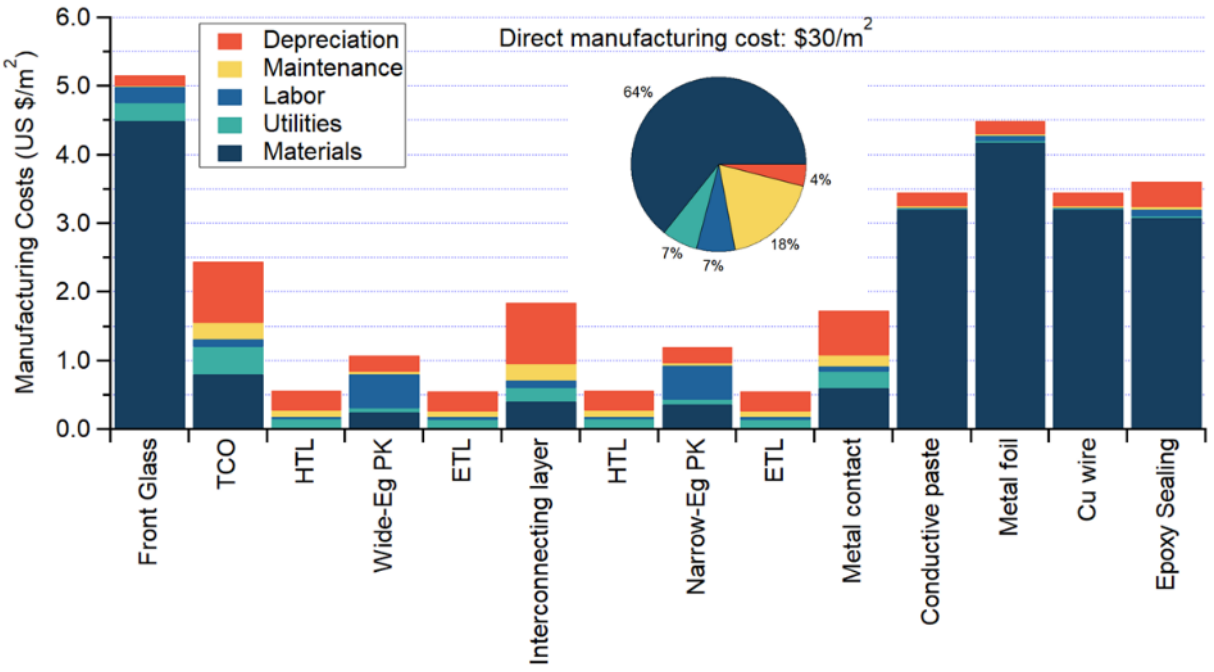

Figure 107. Cost distribution of direct manufacturing costs for low-cost all-perovskite tandem photoelectrodes, inducing cost segments of materials, utilities, labor, maintenance, and depreciation.

We performed a technoeconomic analysis to estimate the costs of solar hydrogen production using perovskite/perovskite tandem photoelectrodes as the working electrode. A simplified cost model was used for the levelized cost of hydrogen (LCOH) calculation, we selected Phoenix, Arizona, USA as the reference project location, where the average annual irradiance is 2677.51 kWh/m^2. Due to the project complexity of the hydrogen generation system, we only consider the costs of photoelectrodes. We assumed a moderate STH efficiency of 15% as a reference and only considered the cost of the photoelectrodes. The discount rate and degradation rates were set to be 6.5% and 0.5%. The LCOH is then calculated by:

$$LCOH = \frac{\sum_{i=0}^{n} \frac{C_i}{(1+d)^i}}{\sum_{i=0}^{n} \frac{H_i}{(1+d)^i}}$$

where C_i and H_i are the total cost of photoelectrodes ($) and hydrogen production (kg) in the i^{th} year, respectively, d is the discount rate, and n is the lifetime of the system.

The annual hydrogen production can be estimated by:

$$H_i = \frac{\eta_{STH} \times (1-r)^i \times Ir \times Area}{(237\ kJ/mol)} \times (0.0224\ m^3/mol) \times (0.084\ kg/m^3)$$

where r is degradation rate, I_r is annual irradiance, and Area is photoelectrode area.

Figure 108b compares the calculated levelized cost of hydrogen (LCOH) generated by all-perovskite and III-V tandem photoelectrodes as a function of their operating lifetime. For the simplicity of the cost analysis and fair comparison, only the photoelectrode cost contributions are taken into consideration in this comparison. Both photoelectrodes can wire to the same anode and couple with the same electrolyzer, and therefore, their balance of system costs would be similar. The technoeconomic analysis results show that low-cost APTPEs with a lifetime of more than ~2 years can reach the LCOH of less than $1/kg for the photoelectrode-specific cost, which is significantly lower than that of conventional tandem III-V technologies and show clearly the economic advantage over today's solar water splitting technologies.

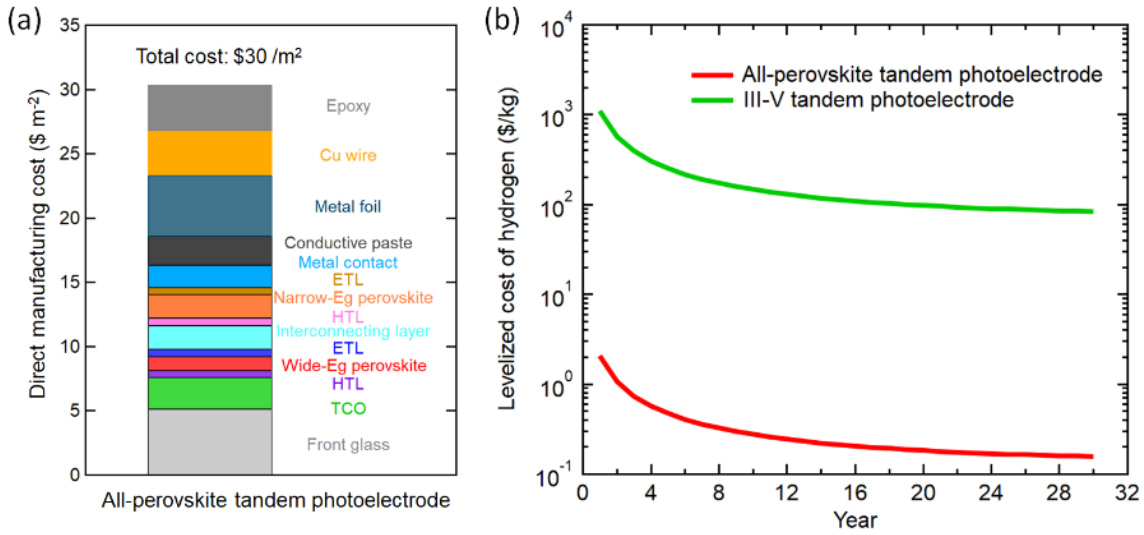

Figure 108. (a) Direct manufacturing cost breakdown for all-perovskite tandem photoelectrodes. (b) Levelized cost of hydrogen comparison of III-V and all-perovskite tandem photoelectrodes as a function of operation lifetime.

Products:

Journal Articles:

[1] C. Li, L. Chen, F. Jiang, Z. Song, X. Wang, A. Balvanz, E. Ugur, Y. Liu, C. Liu, A. Maxwell, H. Chen, Y. Liu, Z. Wang, P. Xia, Y. Li, S. Fu, N. Sun, C. R. Grice, X. Wu, Z. Fink, Q. Hu, L. Zeng, E. Jung, J. Wang, S. M. Park, D. Luo, C. Chen, J. Shen, Y. Han, C. A. R. Perini, J.-P. Correa-Baena, Z.-H. Lu, T. P. Russell, S. De Wolf, M. G. Kanatzidis, D. S. Ginger, B. Chen, Y. Yan and E. H. Sargent, "Diamine chelates for increased stability in mixed Sn–Pb and all-perovskite tandem solar cells," Nat. Energy, (2024). https://doi.org/10.1038/s41560-024-01613-8.

[2] S. Fu, N. Sun, Y. Xian, L. Chen, Y. Li, C. Li, A. Abudulimu, P. N. Kaluarachchi, Z. Huang, X. Wang, K. Dolia, D. S. Ginger, M. J. Heben, R. J. Ellingson, B. Chen, E. H. Sargent, Z. Song and Y. Yan, "Suppressed deprotonation enables a durable buried interface in tin-lead perovskite for all-perovskite tandem solar cells," Joule 8, 2220-2237 (2024). https://doi.org/10.1016/j.joule.2024.05.007.

[3] L. Chen, S. Fu, Y. Li, N. Sun, Y. Yan and Z. Song, "On the Durability of Tin-Containing Perovskite Solar Cells," Adv. Sci. 11, 2304811 (2024). https://doi.org/10.1002/advs.202304811.

[4] N. Sun, S. Fu, Y. Li, L. Chen, J. Chung, M. M. Saeed, K. Dolia, A. Rahimi, C. Li, Z. Song and Y. Yan, "Tailoring Crystallization Dynamics of CsPbI3 for Scalable Production of Efficient Inorganic Perovskite Solar Cells," Adv. Funct. Mater. 34, 2309894 (2024). https://doi.org/10.1002/adfm.202309894.

[5] L. Chen, C. Li, Y. Xian, S. Fu, A. Abudulimu, D.-B. Li, J. D. Friedl, Y. Li, S. Neupane, M. S. Tumusange, N. Sun, X. Wang, R. J. Ellingson, M. J. Heben, N. J. Podraza, Z. Song and Y. Yan, "Incorporating Potassium Citrate to Improve the Performance of Tin-Lead Perovskite Solar Cells," Adv. Energy Mater. 13, 2301218 (2023). https://doi.org/10.1002/aenm.202301218.

[6] Z. Song, C. Li, L. Chen, K. Dolia, S. Fu, N. Sun, Y. Li, K. Wyatt, J. L. Young, T. G. Deutsch and Y. Yan, "All-Perovskite Tandem Photoelectrodes for Unassisted Solar Hydrogen Production," ACS Energy Lett. 8, 2611-2619 (2023). https://doi.org/10.1021/acsenergylett.3c00654.

[7] Q. Jiang, J. Tong, R. A. Scheidt, X. Wang, A. E. Louks, Y. Xian, R. Tirawat, A. F. Palmstrom, M. P. Hautzinger, S. P. Harvey, S. Johnston, L. T. Schelhas, B. W. Larson, E. L. Warren, M. C. Beard, J. J. Berry, Y. Yan and K. Zhu, "Compositional texture engineering for highly stable wide-bandgap perovskite solar cells," Science 378, 1295-1300 (2022). https://doi.org/10.1126/science.adf0194.

Presentations

Z. Song, C. Li, L. Chen, Y. Yan, “(Invited) Monolithic All-Perovskite Tandem Cells for Unassisted Water Splitting,” at Electrochemical Society Meeting (2022). DOI: 10.1149/MA2022-02481800mtgabs.

Z. Song, C. Li, L. Chen, Y. Yan, “Inorganic Lead Halide Perovskites Based Tandem Photoelectrodes for Unassisted Water-Splitting”, MRS Spring Meeting, May 9-13, 2022.

Z. Song, C. Li, J. L. Young, T. G. Deutsch, Y. Yan, “High-Photovoltage Pb-based All-Perovskite Tandem Solar Cells for Unassisted Water-Splitting,” AIP Publishing Horizons: Energy Storage and Conversion, Virtual Conference, August 4-6, 2021.

Z. Song, C. Li, L. Chen, Y. Yan, “Air-stable all-perovskite tandem solar cells,” at Solar Power Tech Conference, Virtual Conference, July 5-8, 2021.

Z. Song, C. Li, L. Chen, S. Rijal, J. L. Young, T. G. Deutsch, Y. Yan, “High-Photovoltage All-Perovskite Tandem Solar Cells for Photovoltaic-Electrolysis Water-Splitting Applications”, IEEE PVSC June 20-25, 2021.